Simulating migrated and inverted seismic data
for enhanced reservoir characterization

Proefschrift

ter verkrijging van de graad van doctor
aan de Technische Universiteit Delft,
op gezag van de Rector Magnificus Prof. dr. ir. J.T. Fokkema,
voorzitter van het College voor Promoties,
in het openbaar te verdedigen,
op woensdag 11 oktober 2006 om 10.00 uur

door

Gerrit TOXOPEUS

ingenieur in de Technische Aardwetenschappen

geboren te Assen

Dit proefschrift is goedgekeurd door de promotoren:

Prof. dr. ir. C.P.A. Wapenaar
Prof. dr. S.M. Luthi
Prof. dr. ir. J.T. Fokkema

Samenstelling promotiecommissie:

Rector Magnificus	voorzitter
Prof. dr. ir. C.P.A. Wapenaar,	Technische Universiteit Delft, promotor
Prof. dr. S.M. Luthi,	Technische Universiteit Delft, promotor
Prof. dr. ir. J.T. Fokkema,	Technische Universiteit Delft, promotor
Prof. dr. G.T. Schuster,	The University of Utah, USA
Prof. dr. H. Doust,	Vrije Universiteit Amsterdam
Prof. dr. ir. A. Gisolf,	Technische Universiteit Delft
Dr. S.A. Petersen,	Norsk Hydro, Noorwegen
Dr. M.E. Donselaar,	Technische Universiteit Delft

Jan Thorbecke heeft als begeleider in belangrijke mate aan de totstandkoming van het proefschrift bijgedragen.

Aan mijn ouders

Contents

1

General introduction

1.1   A brief introduction to a shared-earth modeling concept

The human brain uses different sensors to collect different measurements. These measurements are processed and correlated to, for example, interpret an object. Locating natural resources, in particular reservoir structures containing hydrocarbons, is done using a similar concept that is know as 'shared-earth modeling'. A shared-earth model operates in a collaborative environment in which measurements and members provide information for its construction and others utilize the shared-earth model for prediction (measurements, production, cost and benefit, etc.). Typically exploration/production personnel are the main contributors for the model construction whereas well planners and production engineers use the model for prediction of drilling performance and production. In general all relevant professions are contributors to, as well as users of, a shared-earth model.

Common used measurements in a shared-earth model are: seismic, wireline and core data. Physical experiments on land or sea and in a borehole are

performed to record seismic data and wire-line data, respectively. The popularity of using seismic data is due to the large spatial coverage (typical in the order of many km^2) at relatively low economical costs, compared to drilling boreholes. Boreholes are only available at sparse locations, on average every 2 to 3 km.

The seismic experiment uses sensors that record the response of the subsurface in space and time due to seismic waves generated by an artificial source. The signal of the artificial source has a particular signature and frequency content. Computer algorithms are used to process the recorded data, where the principal processing step is known as seismic migration. For an extensive overview of the different seismic processing steps we refer to Yilmaz [2001]. The migrated seismic data show a structural image of the subsurface. The vertical resolution of a migrated image is typically 25 m or less depending on the target depth range and the used source signature. That means that individual entities larger than 25 m can be recognized as successive reflections [Sheriff, 2001]. The current industry practice is to further enhance the vertical resolution of migrated data by a processing step that is known as (constrained sparse-spike) seismic inversion. Recent examples are presented by Veeken and Da Silva [2004].

A wire-line log shows the recording of a physical property of the subsurface as a function of depth. A log has a typical vertical resolution of 15 cm. Many physical phenomena are nowadays measured in a borehole. For example, a gamma-ray log that is obtained from a nuclear logging instrument, is used to identify lithological properties. The rock-density log times the wave velocity (sonic) log gives the acoustic impedance log that is an important calibration of the seismic signal. This is known as a well-to-seismic tie. Log measurements are calibrated with analysis results of formation samples. These rock-samples are obtained by coring. For an extensive overview of how different wire-line logs are recorded, processed and geologically interpreted, we refer to Luthi [2001].

From the core description, the sedimentary facies characteristics are obtained. From this analysis the deposition environment can then be interpreted. This information is used to select a present-day geological setting that has a high degree of analogy, i.e., the shape, size, hydrodynamic regime and sedimentary environment are comparable. By studying modern-analogue data, both large scale and detailed spatial and property data are

obtained.

In a shared-earth modeling concept, the wire-line, core and modern-analogue data are correlated to construct a detailed geological scenario. It is important to note that wire-line and core data will fit different three-dimensional (3D) geological models, because these are essentially one-dimensional (1D) measurements. Therefore, more information is needed to reduce the non-uniqueness of the geological scenario construction. However, the vertical resolution of migrated seismic data is insufficient to directly support selecting the best geological scenario. In other words, the difference in spatial coverage and vertical resolution hampers constructing a shared-earth model. This discrepancy is reduced by simulating migrated and inverted seismic data (Figure 1.1).

In the appraisal stage of a reservoir when the available data are limited to the wire-line logs, core and migrated data from the discovery well, however the shared-earth model is crucial for making the reservoir development plan [Badescu, 2002].

In a later stage, when more data come available, for example production data, these can be used to further reduce the non-uniqueness of the shared-earth model [Gosselin et al., 2004].

1.2 Statement of the problem: common practice of simulating seismic data in the depth domain

The current industry practice is to simulate seismic data in the depth domain by a convolution in the vertical direction between a source wavelet and a reflectivity trace. The source wavelet has a source signature that matches the one that is used in the real seismic experiment. The reflectivity trace is derived from the wave velocity and rock-density logs using the Zoeppritz equations [Aki and Richards, 2002]. By displaying side-by-side successive 1D traces, a two-dimensional or three-dimensional (2D/3D) seismic image is obtained. This method is named the 1D convolution model [Sheriff, 2001]. By comparison of the simulated seismic image with the migrated real seismic image, it aids in identifying seismic events by a well-to-seismic tie [White and Simm, 2003; Gratwick and Finn, 2005], predicting how variations in an Earth model might appear on a seismic image [Pratson and Gouveia, 2002]
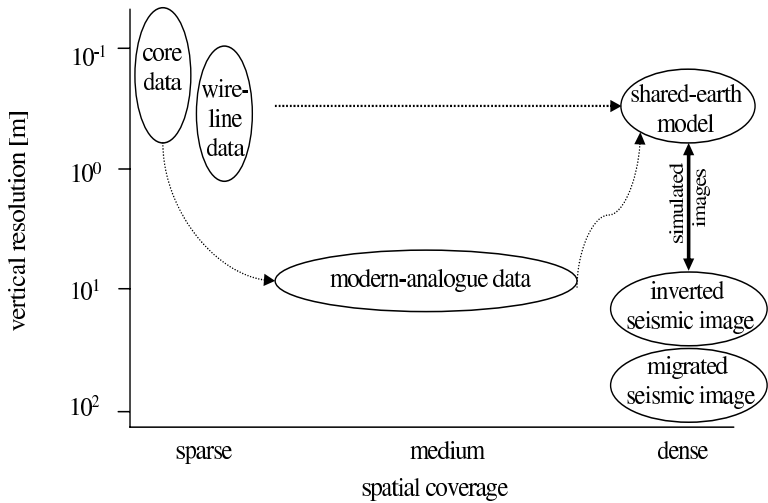
Figure 1.1: Constructing a shared-earth modeling model is hampered by the fact that different measurements have a different spatial coverage and vertical resolution. An earth model characterizes an ideal measurement technique. The dashed lines indicate measured data that are input to the earth model. The solid line indicates the focus of this thesis, simulating migrated and inverted data that can be directly compared to the migrated and inverted real data. Figure is modified from Bos and Van Kruijsdijk [1997].

or interpreting a seismic attribute [Hart and Chen, 2004], etc. However, the 1D convolution model is based on the assumption that the Earth is locally horizontally layered, therefore it only expresses for horizontal layers the vertical resolution of a migrated real seismic image and it does not account for the lateral resolution aspects of the migration process. For this reason, a correct comparison between the simulated and migrated real seismic image is hampered.

The current industry practice is to increase the vertical resolution of migrated real data by a seismic inversion process that is known as (constrained) sparse-spike inversion. Basically, a simulated seismic trace is matched to one

trace of the migrated real data, by varying the number of spikes in an earth model [Oldenburg et al., 1983; van Riel and Berkhout, 1985]. The final result of a seismic inversion process is a constrained sparse-spike real impedance (product of wave velocity and rock-density) image. Unfortunately, this image cannot directly be compared to an impedance image that is built from multiplying P-wave velocity and rock-density data, because of the 1D convolution model in the inversion process.

Alternatively, forward modeling in 2D/3D, subsequently followed by a migration algorithm, results in a simulated migrated image that can be directly compared to the migrated real image. Next, the simulated migrated data can be used as input to a constrained sparse-spike inversion algorithm to simulate an impedance image that can be compared directly to a constrained sparse-spike real impedance image. Unfortunately, two aspects hamper frequent use in shared-earth modeling. Firstly, the high computational costs of one complete simulation. Secondly, when an earth model is changed, the whole simulation has to be run again. Because the 1D convolution model is computationally efficient, these two arguments explain why it is the current industry practice for simulating seismic data.

The horizontal and vertical resolution aspects of migrated seismic data are commonly investigated by studying the combined result of the forward and migration operator. The filtering result of, e.g., one unit strength scattering point would in case of an optimum migration operator be unit at the position of the point scatterer and zero elsewhere. In practice this will not be the case, because of limitations of the source and detector geometry (limited recording aperture and insufficient sampling) [Chen and Schuster, 1999; Vermeer, 2001; Berkhout et al., 2001]. In the literature, this filter is known under different names, a Point-Spread Function (PSF) [Devaney, 1984; Gjøystdal et al., 2002], the Green's function for migration [Schuster and Hu, 2000] or resolution function [Gelius et al., 2002]. To study, in a computationally efficient way, only the vertical resolution aspect of migrated data, the imaging step is omitted from the migration operator. This resulting filter is also known as a resolution function [Berkhout et al., 2001; Volker et al., 2001]. In this thesis, the result of the combined operator is represented by a filter that is named the spatial resolution filter. Since recent, the spatial resolution filter is used in two new seismic applications. Firstly, as an enhanced inversion operator for inverting migrated real data. A recent overview of
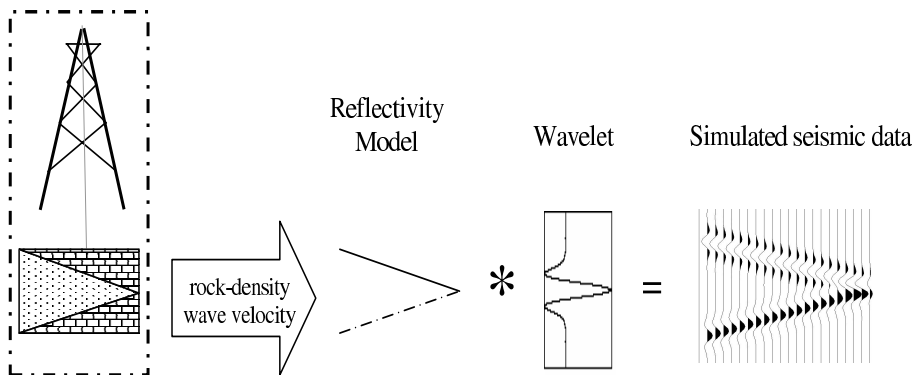
Figure 1.2: The 1D convolution model is summarized by a 1D (in the vertical direction) convolution (denoted by *) between the reflectivity model and a signal of the source. The reflectivity model is computed from the rock-density and wave velocity logs. The source matches the artificial source which is used in the seismic experiment. The solid line illustrates a negative reflection coefficient and the dashed line represent the opposite. The simulated 1D seismic image shows only the vertical resolution of prestack depth-migrated real seismic data. Figure is modified from Sheriff [2001].

examples is published by Yu et al. [2006]. Secondly, to simulate prestack depth-migrated data [Schuster and Hu, 2000; Gjøystdal et al., 2002; Lecomte and Pochon Guerin, 2005]. The simulated migrated image is computed by filtering an earth model by the spatial resolution filter. It is as if we look at the world through glasses that blur it.

This new approach overcomes the main disadvantage of forward modeling in 2D/3D followed by a migration operator, especially when used in a shared-earth modeling concept. Now, an earth model describing a reservoir can be decoupled from an earth model that is used to compute the spatial resolution filter. This enables a target-driven approach and an earth model describing a reservoir can be geologically more detailed and adjusted without having to recalculate the spatial resolution filter, thus providing computational savings. These observations provide the starting point for this thesis.

1.3   Objectives of this research

In summary, to enhance a shared-earth modeling concept the migrated and inverted real seismic data should be (better) incorporated in a shared-earth model by simulating migrated and inverted seismic data. A prerequisite for testing different geological scenarios is that there should be a clear relation between the earth model and the migrated and inverted real data. Finally, the method could be computationally efficient. Therefore, this research has three objectives:

Firstly, extend the combined operator concept such that **simulated migrated and inverted seismic data** can be compared directly to the migrated and inverted real seismic data.

Secondly, demonstrate the ability of the combined operator concept, such that geological ideas of a seismic interpreter can be tested in an **iterative approach**.

Thirdly, include **seismic and geological uncertainties**.

A topic that is not covered in this thesis, is a solid way of comparing simulated migrated and inverted seismic data with the migrated and inverted real data and consequently automatically updating the shared-earth model in order to obtain the best fitting model.

1.4   Outline of the thesis

Chapter 1 is introductory and summarizes the concept of shared-earth modeling. This chapter also states the problem and objectives of this thesis.

The next two chapters deal with the theoretical framework.

Chapter 2 discusses on a conceptional level how a set of operators related to the physical experiment, the migration and inversion step, interact with the Earth. This leads a framework to simulate migrated and inverted data. Key in this framework are the spatial resolution and approximated angle filters. These filters are used to filter a shared-earth model. This is related to the *first objective*. **Chapter 3** decomposes the spatial resolution filter into an angle filter and a band-limitation filter, which is a computationally efficient way of computing a spatial resolution filter. The effect of seismic uncertainties on the spatial resolution filter is studied (*second and third objectives*). This chapter is supported by Appendix A, where the numerical implementation

of the Gazdag phase-shift operator is discussed.

Chapter 4 evaluates the ability of the framework to accurately simulate migrated and inverted data, by simulating data of three earth models. The third earth model represents the complex geological setting found on the Sigsbee escarpment in the deepwater Gulf of Mexico and illustrates how seismic interpretation is enhanced in the target-zone that is located under the massive salt body. **Chapter 5** presents a case study of the Cook Formation (Oseberg Field, offshore Norway). The core, wire-line data and size and shape data of two modern-analogues are used to build different earth models that are used to simulate migrated and inverted data. These simulations are directly compared to the migrated and inverted real seismic data. In this way more confidence is gained in one of the geological scenarios.

Chapter 6 gives an application of a new seismic attribute based on the multi-scale analysis. Simulated inverted data are used to investigate whether constrained sparse-spike inverted real data are proper input to the multi-scale analysis. Next, the multi-scale analysis is used to track inclined internal reflectors of the Cook Formation in the inverted real data. The results are interpreted geologically by the results of the multi-scale analysis that is also performed on the wire-line data and an independent detailed seismic interpretation study.

Finally, in **Chapter 7** the advantages and limitations of simulated migrated and inverted data, an iterative shared-earth modeling approach and the new seismic attribute are discussed. Furthermore, recommendations for future research are given.

2

Framework for simulating prestack depth-migrated and inverted seismic data

A prerequisite for seismic interpretation is to have a clear relation between the real prestack depth-migrated data and a shared-earth model. The current industry practice is to use the 1D convolution model to simulate a seismic image, which expresses the vertical resolution of migrated real seismic data but does not account for the lateral resolution aspects of the migration process. After briefly reviewing the seismic processing steps applied to real data, a new framework using a spatial resolution filter is introduced to simulate prestack depth-migrated data, which can be compared directly with the migrated real data.

Seismic inversion aims at increasing the resolution by removing the signal of the source that blurs the migrated real data. However, the current industry practice of seismic inversion is based on the assumption that the migrated real data are described by the 1D convolution model. This results in impedance data that cannot directly be compared to an impedance model.

By introducing an (approximated) angle filter, the framework simultaneously simulates inverted and migrated seismic data in a specific target-zone, which can be compared directly with the inverted and migrated real data.

The spatial resolution filter and (approximated) angle filters are discussed in more detail in Chapter 3 and Appendix A.

2.1   Representation of seismic data

In a land or marine seismic survey, a specific source and detector layout is deployed to probe the Earth's subsurface structure. A simplified 2D illustration of a marine acquisition is shown in Figure 2.1, where a ship drags a source and a finite number of detectors through the water. With regular intervals, an artificial source generates a seismic wave field. This wave field travels into the Earth and will partly reflect at different layers. At the surface, using different detector positions, this reflected wave field is recorded in time. The collection of these recordings is referred to as one shot record. The distance between the source and one detector position is denoted as offset. Along the course of the ship, the seismic experiment is repeated for many shot positions.

On a conceptional level, the acquired seismic data are described as

$$\text{Real data}(\mathbf{x}_D, \mathbf{x}_S, t) = \text{Physical measurement}\{\text{earth}\},$$

where $\mathbf{x}_D$ and $\mathbf{x}_S$ denote the spatial coordinate vectors of the detector and source positions, respectively, and t denotes time. Similarly, the simulated seismic data are obtained by a forward operator that acts on an earth model. The earth model is a possible representation of the Earth in terms of the parameters dominating the measurements used, while the forward operator resembles our description of the physical measurement (Figure 2.2), according to

$$\text{Simulated data}(\mathbf{x}_D, \mathbf{x}_S, t) = \text{Forward operator}\{\text{earth model}(\mathbf{x})\},$$

where $\mathbf{x}$ denotes the spatial coordinate vector of position in the earth model.
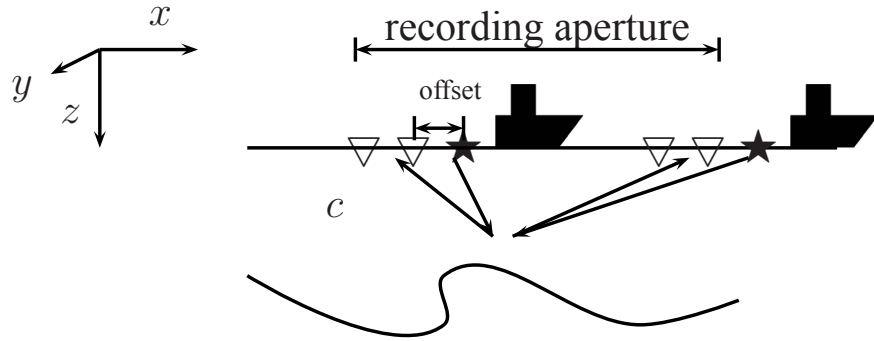
Figure 2.1: Schematic illustration of recording seismic data on sea. c denotes the wave velocity, ★ is a source at different lateral position and ▽ is a detector. The arrows illustrate the paths that a primary wave field travels between a source, a geological boundary (curved solid line) and different detectors.

2.2 Migrated seismic data

From the seismic measurements, a structural image of the Earth is obtained by using a prestack depth-migration operator. This extends the relations to

Real prestack depth-migrated image$(\mathbf{x}) =$
Prestack depth-migration operator$\{$Real data$(\mathbf{x}_D, \mathbf{x}_S, t)\}$,

Simulated prestack depth-migrated image$(\mathbf{x}) =$
Prestack depth-migration operator$\{$Simulated data$(\mathbf{x}_D, \mathbf{x}_S, t)\}$.

The interpreter of the prestack depth-migrated data is concerned with the question how and to what extent geological details are visible in the prestack depth-migrated image. Ideally he or she should investigate the following relations,

Real observations   **Simulating the real observations**
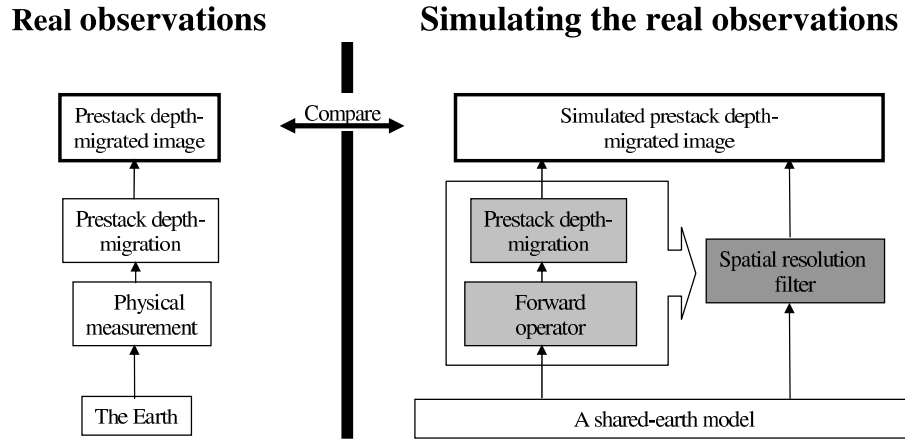
Figure 2.2: Framework of "Simulating in a complete sense", modified from Petersen [1992]. The figure summarizes how prestack depth-migrated data are simulated by filtering an earth model with a combined operator. The combined operator is represented by the spatial resolution filter.

Real prestack depth-migrated image($\mathbf{x}$) =
Prestack depth-migration operator{Physical measurement{Earth}},

Simulated prestack depth-migrated image($\mathbf{x}$) =
Prestack depth-migration operator{Forward operator{earth model($\mathbf{x}$)}}.

These are the combined operations of the aforementioned processes. Therefore, to simulate prestack-depth migrated data a combined operator is introduced to represent the two operators,

Simulated prestack depth-migrated image($\mathbf{x}$) =
Combined operator{earth model($\mathbf{x}$)}.

2.3 Application I: simulating prestack depth-migrated seismic data

The combined operator is represented by a spatial resolution filter, which is obtained from computing the image of a single unit strength scattering point in a background medium (the impulse response of the filter). Using the spatial resolution filter, the simulated migrated data are described as

$$\text{Simulated prestack depth-migrated image}(\mathbf{x}) =$$
$$\text{Spatial resolution filter}\{\text{earth model}(\mathbf{x})\}.$$

Thus, instead of forward modeling shot records and subsequently using a prestack depth-migration algorithm, an earth model is filtered by a spatial resolution filter to simulate prestack depth-migrated data (illustrated by the third column in Figure 2.2). The spatial resolution filter resembles the processes of the physical measurement and the prestack depth-migration algorithm. The simulated migrated data can be compared directly to the migrated real data.

This approach overcomes the main disadvantage of forward modeling in 2D/3D and consequently followed by a migration operator, especially when used in shared-earth modeling. Firstly, there is a clear relation between a shared-earth model and the migrated real and inverted real data, unlike the common used 1D convolution model. Second there is no disk-storage needed of the intermediate result (shot records). Finally, a shared-earth model describing the target-zone (e.g., an aquifer or hydrocarbon reservoir or its analogue) can be decoupled from the earth model that is used to compute the spatial resolution filter. Because of this, a shared-earth model describing the reservoir can be geologically more detailed and adjusted without having to recalculate the spatial resolution filter that saves computational time. These observations are very attractive for iterative testing of different geological scenarios in a shared-earth modeling approach. In Chapter 5 this is illustrated using a case-study of the Cook Formation (Oseberg Field, offshore Norway).

2.4   Application II: simulating (constrained sparse-spike) inverted data

Except prestack depth-migrated seismic data, inverted seismic data are also valuable to support subsurface (geological) interpretation. Some recent applications are found in Veeken and Da Silva [2004]. The current industry practice is to use the migrated prestack depth-migrated seismic data as a starting point. On a conceptional level, the real impedance image is obtained by using a seismic inversion algorithm as

$$\text{Real impedance image}(\mathbf{x}) =$$
$$\text{Seismic inversion}\{\text{Real prestack depth-migrated image}(\mathbf{x})\}.$$

The integration and scaling steps that are part of a seismic inversion process are omitted for notational convenience. More details on these two steps can be found in Ferguson and Margrave [1996].

Similarly, a simulated impedance image is obtained by using the seismic inversion algorithm on the simulated prestack depth-migrated data as

$$\text{Simulated impedance image}(\mathbf{x}) =$$
$$\text{Seismic inversion}\{\text{Simulated prestack depth-migrated image}(\mathbf{x})\}.$$

In the next chapter, it is shown that the spatial resolution filter can be decomposed into two new filters. These filters are named an angle and a band-limitation filter. Using these two new filters, simulating a prestack depth-migrated seismic image is also done by using the following relation,

$$\text{Simulated prestack depth-migrated image}(\mathbf{x}) =$$
$$\underbrace{\text{Band-limitation filter}\{\text{Angle filter}}_{\text{Spatial resolution filter}}\{\text{earth model}(\mathbf{x})\}\}.$$

This relation is used to rewrite the previous introduced relation to obtain the simulated impedance image as

Simulated impedance image$(\mathbf{x}) =$

Seismic inversion{Band-limitation filter{Angle filter{earth model$(\mathbf{x})$}}}.

Next, the influence of the seismic inversion algorithm on the two filters is discussed. We discuss two classes of seismic inversion algorithms. From the seismic literature, these algorithms can be grouped into two classes.

The **first class** of seismic inversion algorithms correctly handles all aspects of the seismic real data in the inversion process, e.g., least-squares inversion [Nemeth et al., 1999] and migration-deconvolution [Yu et al., 2006].

The effect of all these algorithms on the (migrated) real data is represented schematically to have correctly removed the band-limitation filter. Thus, the previous introduced relation reduces to,

Simulated impedance image$(\mathbf{x}) =$ Angle filter{earth model$(\mathbf{x})$}.

This provides an alternative relation to simulate impedance data that can be compared directly to the impedance real data that is obtained with the first class of seismic inversion algorithms.

The **second class** of seismic inversion algorithms represents the current industry practice that in the remainder of this thesis is denoted as a constrained sparse-spike inversion algorithm. These algorithms have in common that they make use of the 1D convolution model [Oldenburg et al., 1983; van Riel and Berkhout, 1985; Lancaster and Whitcombe, 2000]. Hence, the second class of inversion algorithms does not account for the lateral resolution aspects of the migration process. This is simulated by a partly removed band-limitation filter,

Simulated constrained sparse-spike impedance image$(\mathbf{x}) =$

Partly removed band-limitation filter{Angle filter{earth model$(\mathbf{x})$}}.

Thus, this relation provides an alternative way to simulate impedance data that can be compared directly to constrained sparse-spike impedance real data. The previous relation is rewritten by introducing an approximated angle filter,

Simulated constrained sparse-spike impedance image($\mathbf{x}$) =

Approximated angle filter{earth model($\mathbf{x}$)}.

By realizing that the spatial resolution filter is composed of the angle and band-limitation filter, an approximated angle filter is obtained by constrained sparse-spike inverting the spatial resolution filter that is also used to simulate a prestack depth-migrated image (see also Section 3.1.1 for an example).

2.5   Practical aspects

The discussion of this chapter is summarized in Figure 2.3. It shows how the spatial resolution filter and (approximated) angle filters are used to filter an earth-model to simulate prestack depth-migrated and (constrained sparse-spike) impedance data, respectively. As a consequence of the fact that the filters simulate the operators used to forward model, prestack depth-migrate and (constrained sparse-spike) invert the real data, the simulated data sets can be compared directly to the real data sets.

However, in the comparison of migrated simulated and migrated real data, it is tacitly assumed that all multiple scattering has been properly removed from the real data or imaged to its correct position of origin. Removing multiple energy is of great importance in seismic processing and the current industry practice is to remove only the free surface scattering from the real data; internal multiple scattering is only partly removed [Verschuur et al., 1992; Hill et al., 1999; Matson and Dragoset, 2005].

To reduce the computational costs of simulating migrated and inverted data, the following assumptions are used in this thesis. We assume that a prestack-depth migrated real image approximates zero-offset migrated data. These data are obtained by moving a single source and a single detector along a line with no offset between them. In other words the source and detector positions coincide (Figure 2.4 (a)). However, this recording geometry is not realizable in reality (Figure 2.1).

Next, consider an alternative geometry that approximates zero-offset data, the so-called exploding reflector modeling. In this model, sources are places at the reflectors and the source strength are chosen proportional to the reflection coefficients. The propagation velocity in the model is taken half the

actual velocity. When all sources "explode" simultaneously, an image is obtained that resembles a zero-offset image (Figure 2.4 (b) [Loewenthal et al., 1985; Yilmaz, 2001]). In the new framework, one source is placed in the model and the source strength is taken equal to a wavelet or 1. Subsequently, these forward modeled data are migrated to obtain a zero-offset spatial resolution filter or an angle filter, respectively. Alternatively, a zero-offset spatial resolution or angle filter can be directly constructed in the double-Fourier domain. A discussion is provided in the next chapter and Appendix A.

To remove the zero-offset assumption, a common-offset spatial resolution filter can be computed. This is done in three steps. In step one, one-way data are computed using the exploding reflector modeling approach. In step, from these data two-way common-offset data are created [Deregowski and Rocca, 1981; Wapenaar and Grimbergen, 1996]. These common-offset data do not resemble a physical experiment. Therefore, computationally efficient migrating these data is not straightforward. Many authors use an approximate method i.e., the stationary phase or a diffraction-summation type migration method, to perform common-offset migration [Popovici, 1994; Yilmaz, 2001]. In this thesis, common-offset migrated data are obtained by applying a standard prestack-depth migration algorithm to the common-offset data only, which is a time-consuming step (see also Section 3.3).

A shared-earth-model is built using the wave velocity and rock-density logs. Next, a reflectivity model is derived using the Zoeppritz equations [Aki and Richards, 2002]. As an initial approach, the reflectivity grid is derived under a normal-incidence assumption. Additionally, angle information can be added to remove the normal-incidence assumption. This reflectivity model is then filtered by the spatial resolution filter and the (approximated) angle filter to simulate prestack depth-migrated and (constrained sparse-spike) impedance data, respectively. As a result of the proposed framework, the earth model that is used to compute the spatial resolution filter can be different from the earth model that describes the target-zone.

Finally, though the presented framework is valid in 3D for an arbitrary elastic earth model, all examples are in 2D and show only P-wave data. In the case study presented, the variations in the strike direction of the Cook Formation are likely to be small compared to those in the dip direction (Chapter 5). Therefore, a 2D cross-section of 3D migrated and inverted data is thought to be well approximated with 2D images.
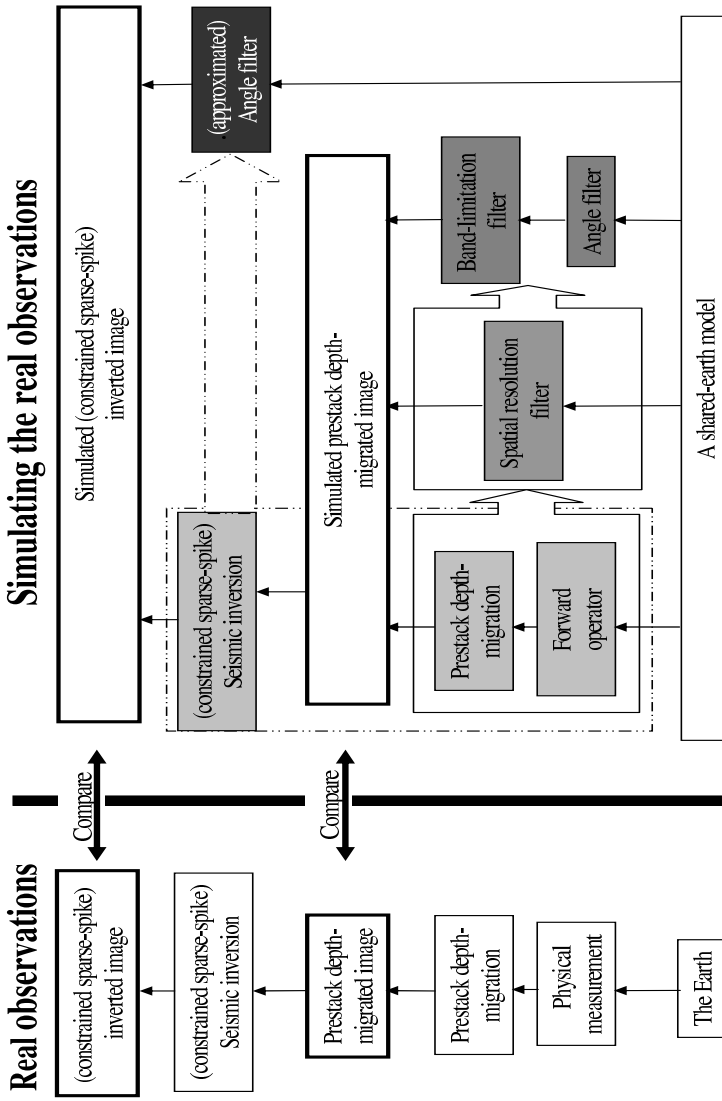
Figure 2.3: The figure summarizes in a conceptual way how different operators are used to obtain migrated and inverted real seismic data, which can be simulated using four different ways (indicated by the gray values). The (approximated) angle and band-limitation filters are used in this thesis to simulate migrated and inverted seismic data.

(a) Zero-offset forward modeling

recording aperture

c

(b) Exploding reflector modeling

recording aperture

$c/2$

unit strength scattering point
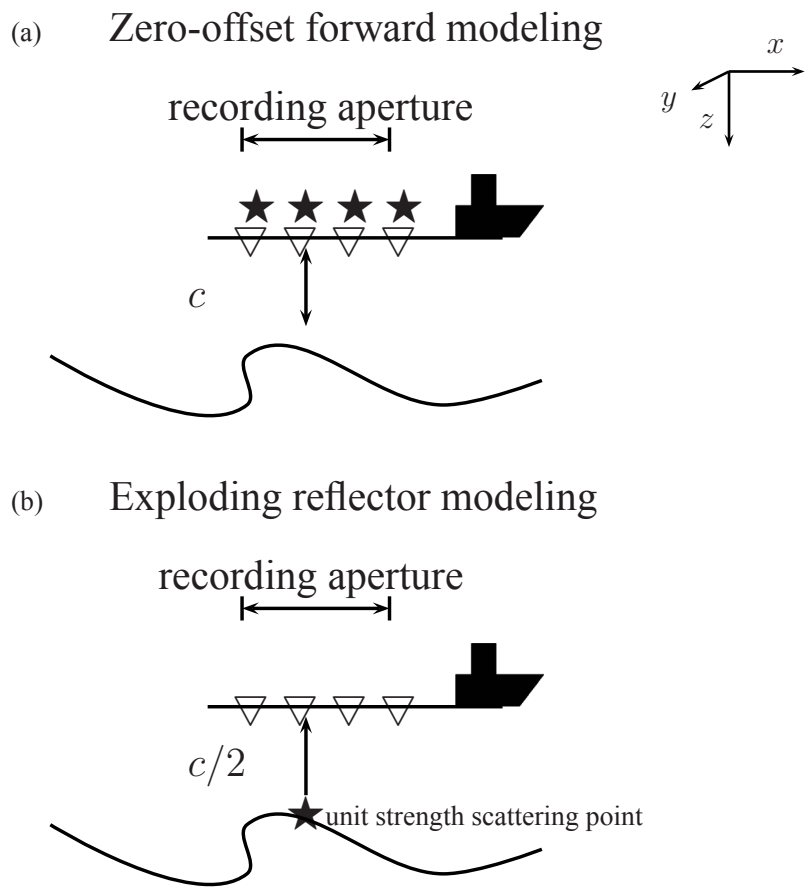
Figure 2.4: (a) Simulating the field experiment (Figure 2.1) by the zero-offset experiment. (b) The exploding reflector model of (a) for one unit strength scattering point. c denotes the wave velocity, ★ is a source at different lateral position and ▽ is a detector. The arrow illustrates the paths that a primary wave field travels between a source, a geological boundary (curved solid line) and different detectors.

3

Approximating the spatial resolution filter in a laterally variant medium

In the previous chapter, it was shown how prestack depth-migrated and (constrained sparse-spike) impedance data are simulated by filtering a reflectivity model (shared-earth model) with filters. The spatial resolution filter depends on the macro velocity properties of the earth model as well as on the acquisition configuration and seismic processing parameters.

In order to facilitate iterative shared-earth modeling, this chapter focuses on efficiently approximating the spatial resolution filter in a laterally variant medium. This is done by decomposing the spatial resolution filter into an angle and a band-limitation filter.

Additionally, the shape of a spatial resolution filter is discussed by reviewing Hagedoorn's isochrone summation and studying the influence of seismic uncertainties; a "wrong" migration velocity model, statics and a laterally varying source wavelet. At the end of this chapter the introduced angle and band-limitation filters are compared to previous research.

This chapter is supported by Appendix A, where the numerical implementation of the Gazdag phase-shift operator is discussed.

3.1 Decomposing the zero-offset spatial resolution filter

In a model with a constant P-wave velocity of 2000 m/s, a single unit strength scattering point is buried at a depth of 2000 m. Symmetrically overlying the unit strength scattering point is a zero-offset acquisition setup, with a total recording aperture of 3000 m (Figure 3.2 (a)). The source signature is a filtered Ricker wavelet with a sampling of 4 ms (Figure 3.1 (a)). The wavelet is characterized by a peak frequency of 25 Hertz (Hz) and minimum and maximum frequency limits of $f = 5$ and 70 Hz, respectively (Figure 3.1 (b)). The two-way time (TWT) recorded zero-offset response is shown in Figure 3.2 (b). After prestack depth-migrated a spatial resolution filter is obtained (Figure 3.2 (c)). Both results are transformed to the double-Fourier domain, where the ω axis of Figure 3.2 (d) is scaled with half the velocity to illustrate the principle of migration: mapping one line of constant ω of Figure 3.2 (d) onto one circle of Figure 3.2 (e) [Stolt, 1978].

In the double-Fourier domain two key features of the spatial resolution filters are observed. *Firstly*, the spectrum is limited from $\omega_{min} = 10\,\pi$ to $\omega_{max} = 140\,\pi$ [radians/s], where $\omega = 2\pi\,f$. *Secondly*, the spatial resolution filter is constrained by the maximum angles of wave propagation (φ_1 and φ_2, see also Figure A.1). For a homogeneous medium these angles are directly related to the total recording aperture [Schuster and Hu, 2000]. Because the acquisition setup is symmetrically overlying the unit strength scattering point, the maximum angles of wave propagation are symmetric. However, using a different acquisition setup or a laterally variant medium, an asymmetric spatial resolution filter can be obtained as well.

Now that the two key features are identified, an alternative way of obtaining a spatial resolution filter can be developed, namely by directly constructing two new filters in the double-Fourier domain. The first filter is named an **angle filter** and uses the maximum angles of wave propagation to form a stop/pass filter (Figure 3.3 (a)). This filter is also obtained from the combined operator, if a delta function is used as source wavelet. The second filter

(a)

(b)
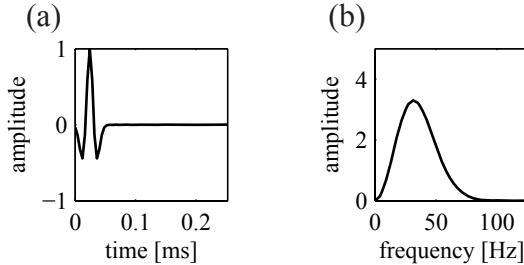
Figure 3.1: (a) Minus the second derivative of a Gaussian function, a so-called Ricker wavelet. (b) The Fourier spectrum of figure (a). The peak frequency is located at the maximum peak in the Fourier spectrum.

is named a **band-limitation filter**, it is circularly shaped and contains the spectrum of the modeling wavelet along its radius (Figure 3.3 (b)). Inverse Fourier transforming give the two filters in the space domain (Figures 3.3 (d) and (e)). Multiplication of the two filters and subsequently inverse Fourier transforming gives a spatial resolution filter, which is also directly obtained from the combined operator (Figures 3.2 (c) and 3.3 (f)). This shows that the spatial resolution filter can be interpreted as acting as two separate filters, summarized in the double-Fourier domain as: A×B=C, where A is the angle filter, B is the band-limitation filter and C denotes the combined operator which is represented by the spatial resolution filter.

■ 3.1.1 An approximated angle filter

In the preceding chapter, an approximated angle filter was introduced to simulate constrained sparse-spike inverted data. This approximated angle filter is obtained by constrained sparse-spike inverting a spatial resolution filter, which is outlined in Figure 3.4. It is summarized by obtaining a 1D inversion wavelet that is used to invert the spatial resolution filter in the double-Fourier domain. The 1D inversion wavelet can be obtained by selecting the $k_x = 0$ component in the double-Fourier domain of the spatial resolution filter. In the double-Fourier domain of the approximated angle filter it is observed that only around $k_x = 0$ the spectrum equals 1 and then it decays (Figure 3.4 (f)). This means that only partly the band-limitation filter is correctly re-
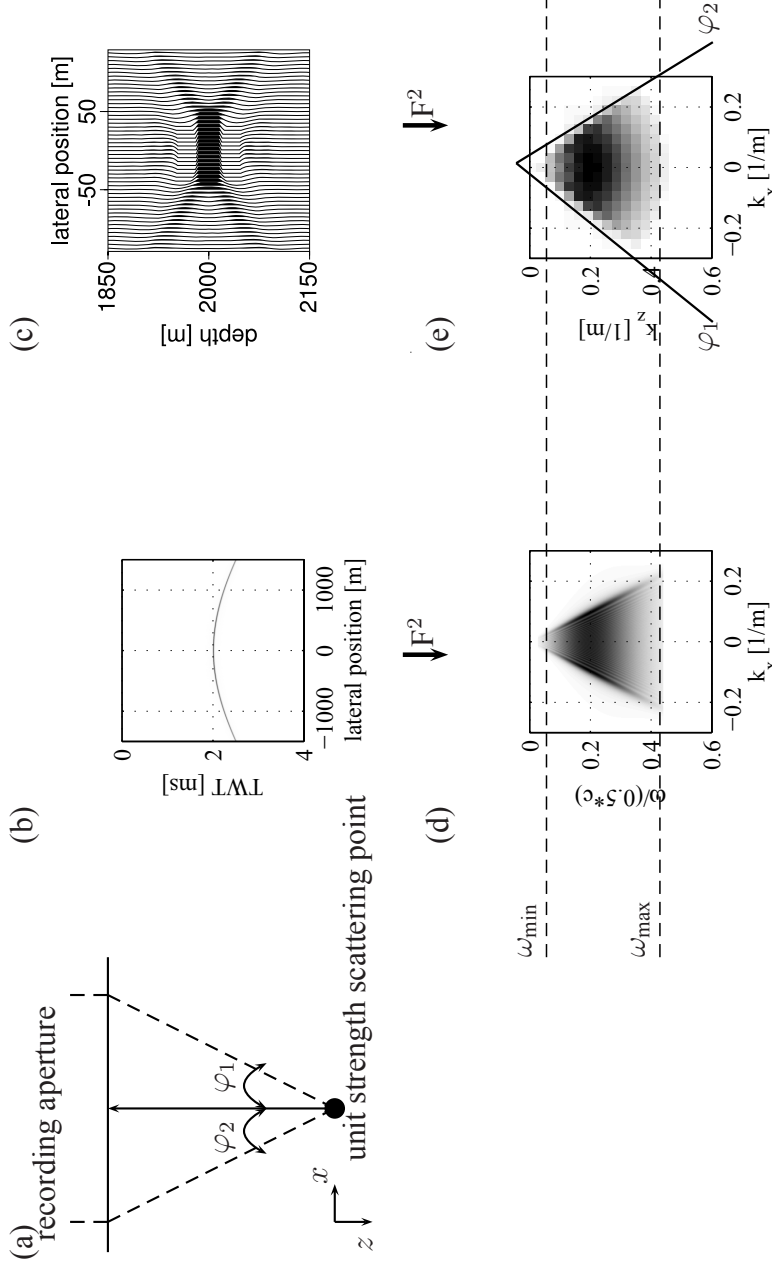
Figure 3.2: (a) Acquisition setup with a recording aperture of 3000 m over the single unit strength scattering point at a depth of 2000 m. (b) Forward modeling response from the single unit strength scattering point. (c) A spatial resolution filter: (d) and (e) Double-Fourier transformed results of figures (b) and (c). F^2 denotes the forward 2D Fourier transform. The maximum angles of wave propagation are denoted by φ_1 and φ_2 and the spectrum is limited by ω_{min} to ω_{max}.
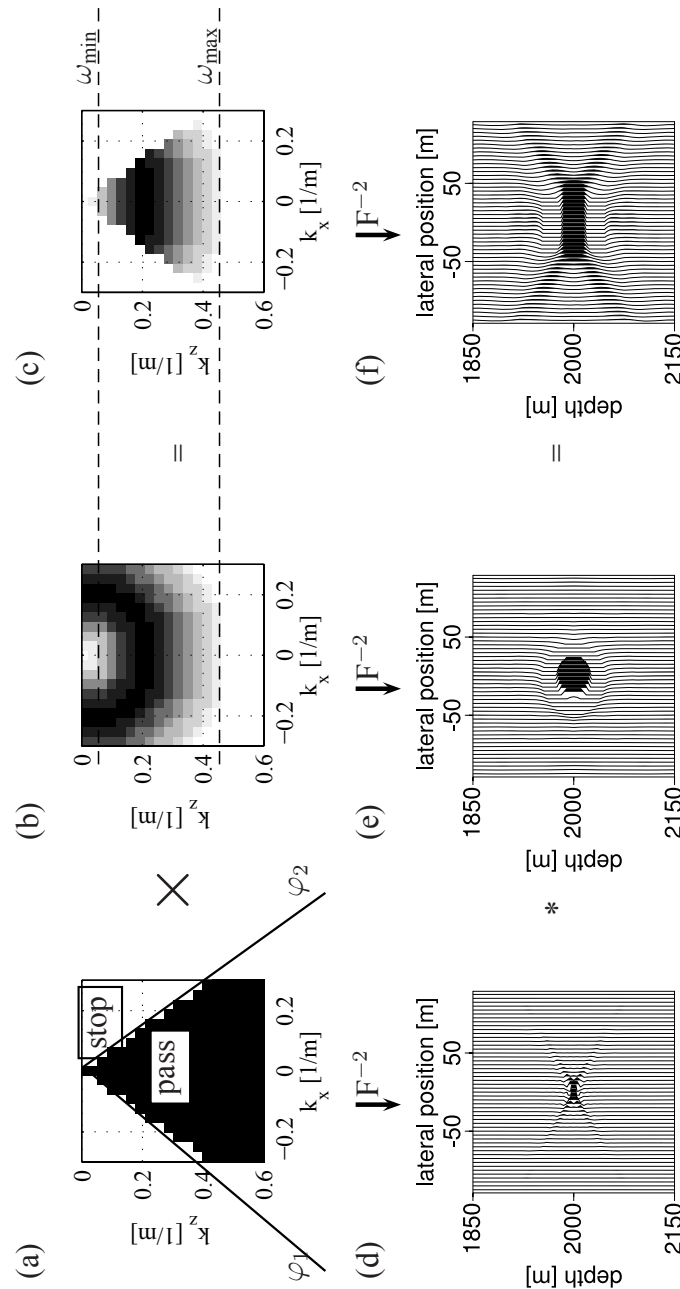
Figure 3.3: *(a) An angle filter in the double-Fourier domain. (b) A band-limitation filter in the double-Fourier domain. (c) A spatial resolution filter in the double-Fourier domain. (d) An angle filter: (e) A band-limitation filter: (f) A spatial resolution filter. F^{-2} denotes the inverse 2D Fourier transform. $\times$ and $*$ denote multiplication and multidimensional spatial convolution, respectively. The maximum angles of wave propagation are denoted by φ_1 and φ_2. The spectrum is limited by ω_{min} to ω_{max} which resembles the signal of the artificial source signature that is used in the physical experiment.*
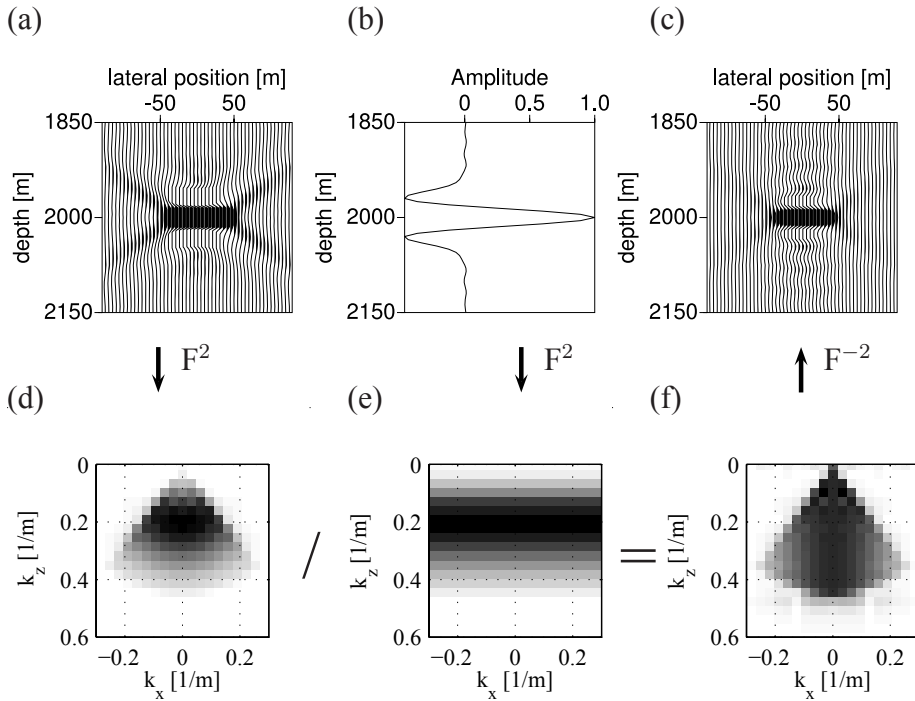
Figure 3.4: *(a) Repeating the spatial resolution filter of Figure 3.2 (c). (b) A 1D wavelet. (c) An approximated angle filter. (d) to (f) show the double-Fourier transform of figures (a) to (c). F^2, F^{-2} denote the forward, inverse 2D Fourier transform, respectively. A trace-by-trace inversion in the double-Fourier domain is denoted by /.*

moved, otherwise the spectrum would either be 1 or 0, like in the angle filter (Figure 3.3 (a)). After a 2D inverse-Fourier transformation an approximated angle filter in the spatial domain is obtained (Figure 3.4 (c)).

Isochrone summation

At this point is has become evident that the total recording aperture is controlling the shape of a spatial resolution filter. This is also expressed by the fact that the angle filter is controlled by the maximum angles of wave prop-

agation. By briefly discussion the pioneering work of Hagedoorn [1954] on seismic migration, it can be graphically illustrated how the shape of the spatial resolution filter changes for different recording apertures.

According to Hagedoorn, the aim of migration is to position the reflected energy from the wavefront measured at the subsurface at its correct position in the subsurface. From one reflection arrival time, belonging to a particular source detector combination, a so-called surface of equal reflection time can be constructed. In Figure 3.5, a set of wavefronts centered at the source position x_S and the detector position x_D, is shown. A reflection time of 2T s observed at x_D can originate from any point on the surface of equal traveltime consisting of lines of intersection between wavefront surfaces (T+t) [s] from x_S with wavefront surfaces (T-t) [s] from x_D. This is indicated by the isochron (thick solid line) in Figure 3.5.

This principle is used to migrate trace-by-trace the zero-offset recording of a single unit strength scattering point (Figure 3.2 (b)). Intermediate results are illustrated by a series of images that starts with the prestack depth-migrated response of the middle trace only (at lateral position = 0 m). The seismogram that contains only one spike is smeared onto the locus of possible reflection points in the migrated image, a semicircle [Stolt, 1978; Yilmaz, 2001]. Next, more and more zero-offset source and detector combinations are added. For the randomly chosen 3, 7, 21, 41 and 201 zero-offset source and detector combinations the result is shown in Figure 3.6. Every time an extra trace is added, a part of another isochron cancels, this stops when the total recording aperture, which resembles 201 source and detector combinations, is reached. This process of adding isochrons is linear. Thus, randomly an isochron can be added. This property can be used as an alternative way to create different spatial resolution filters in a laterally varying medium at a constant depth. After calculating all isochrons individually, a specific spatial resolution filter is computed by adding the proper isochrons. Which isochrons need to be summed would be derived from (a-priori) ray-trace information (Kirchhoff migration) revealing the φ_1 to φ_2 range at a specific location in the subsurface. This process is also applicable to compute a specific common-offset spatial resolution filter.
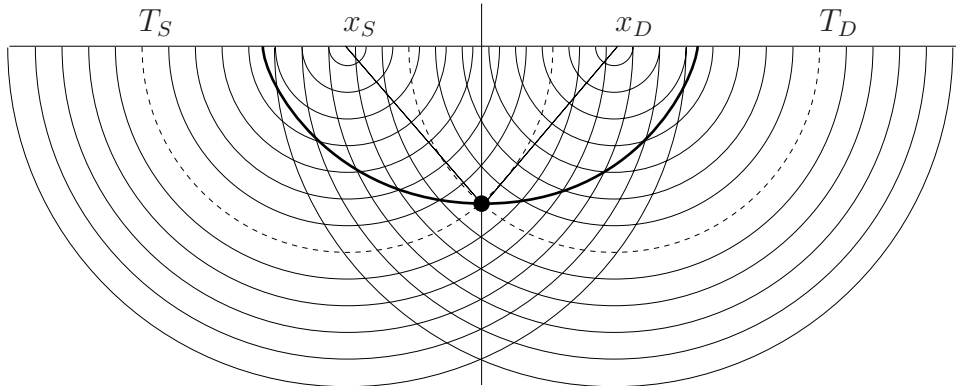
Figure 3.5: A single source detector combination defines for every reflection time a surface of equal travel times. The vertically plotted point at the surface of equal travel times in the middle between source and detector is used to determine a surface of equal reflection times which is an ellipse in two-dimensions.

3.2 A simple salt model

A simple salt model is created by adding to the previous homogeneous model, a water layer and a strong velocity contrast (Figure 3.7 (a)). The modeling wavelet, sampling, zero-offset acquisition setup, recording aperture and position of the single unit strength scattering point (x= 1500 m and z= 2000 m) are all kept the same. The spatial resolution filter is constructed from an angle and a band-limitation filter, the two filters which decompose a spatial resolution filter.

The angle filter uses the maximum angles of wave propagation, found in the laterally variant model by performing ray-tracing through a smoothed velocity model. The obtained maximum angles of wave propagation are φ_1=$\sim 15°$ and φ_2= $\sim -35°$, which is illustrated in Figure 3.7 (c). The band-limitation filter is obtained with the aid of the input wavelet. Using the velocity trace at 1500 m, the wavelet is time-to-depth converted to z= 2000 m. Both filters are constructed in the double-Fourier domain, multiplied and through the inverse Fourier transform the corresponding spatial resolution filter is obtained (Figure 3.8 (a)). It is named a local 1D spatial resolution filter, because the
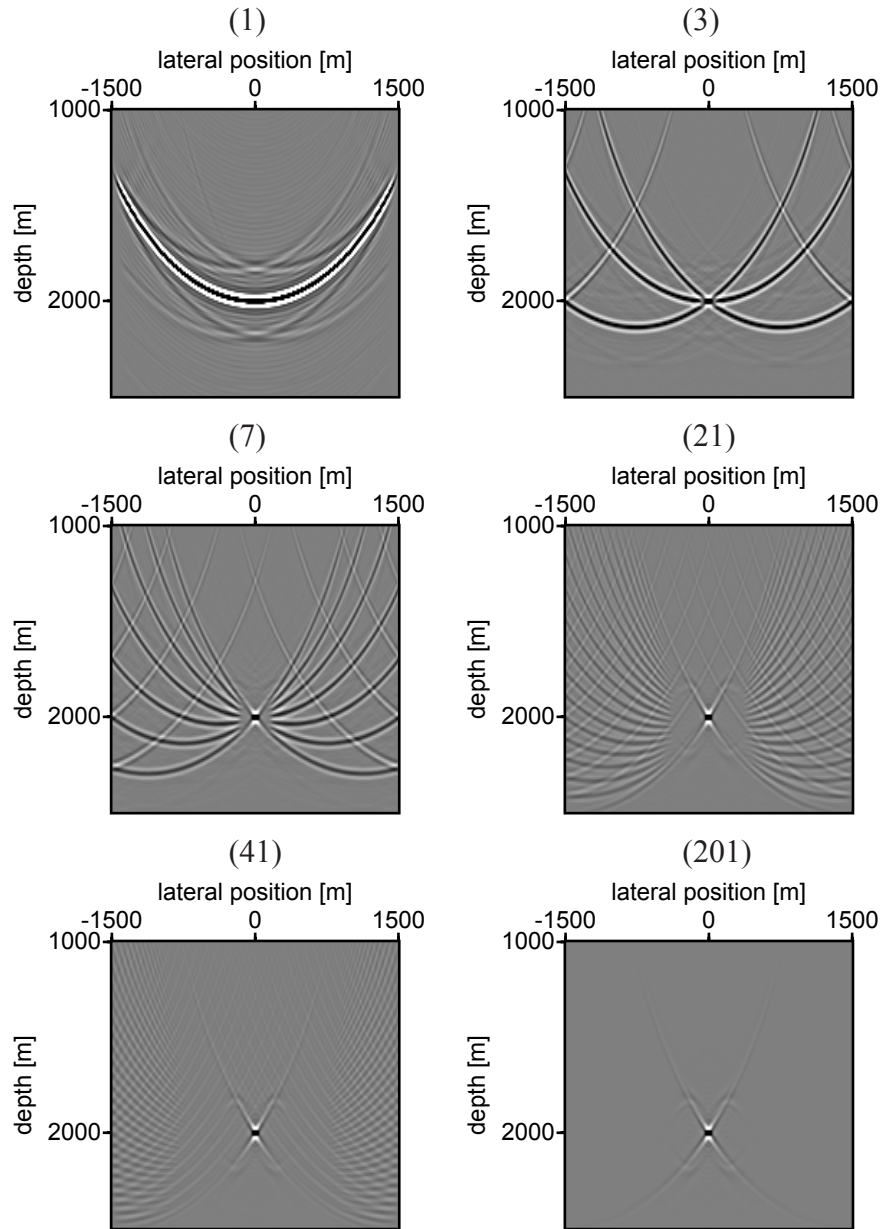
Figure 3.6: Series of images show how the shape of a spatial resolution filter changes is related to the total recording aperture. The number of equally spaced source and detector pairs is increases from 1,3,7,21,41 to finally 201.

spatial resolution filter is obtained under a "local 1D" assumption. That the medium is laterally variant is taken into account by constraining the spatial resolution filter by the maximum angles of wave propagation obtained by ray-tracing in the smoothed model of the laterally variant medium.

The accuracy (in terms of the phase) is verified by a reference spatial resolution filter that is computed using the forward and migration operator in the $x - \omega$ domain [Thorbecke et al., 2004] (Figure 3.8 (b)). The reference result shows that there is a strong resemblance (regarding the phase) with the local 1D spatial resolution filter. The shape of the local 1D spatial resolution filter is slightly different from the reference case (illustrated by the black arrows in Figures 3.8 (a) and (b)). This is also expressed in the double-Fourier domain, where the maximum angles of wave propagation for the $x - \omega$ spatial resolution filters are $\varphi_1 = \sim 10°$ and $\varphi_2 = \sim -35°$. Thus, by ray-tracing the φ-range is obtained about 5° too wide. Perhaps because in the ray-tracing method a smoothed velocity model is used.

Another difference between the two is that in the double-Fourier domain of the reference case a gap is shown in between the maximum angles of wave propagation, indicated by the double arrow in Figure 3.8 (e). For the local 1D spatial resolution filter it is assumed that between φ_1 and φ_2 all angles are present, a gap is not taken into account. Obviously, at increasing computational costs the local 1D spatial resolution filter can also include an irregular range of angles of wave propagation. This would lead to the method presented by Gelius et al. [2002]. Finally, compare the local 1D spatial resolution filter (Figure 3.8 (a)) with the spatial resolution filter computed in the previous introduced homogeneous model (repeated in Figure 3.8 (c)). It shows that although the same acquisition setup is used, the shape of the spatial resolution filter differs greatly. As will be discussed and illustrated in Chapter 4, this has an important influence on how accurately prestack depth-migrated and constrained sparse-spike inverted data are simulated.

■ 3.2.1 Studying seismic uncertainties

In the previous discussion it has been shown that the shape of a spatial resolution filter is mainly controlled by the source wavelet and the maximum angle of wave propagation. However, it was tacitly assumed that all seismic processing steps could be ideally performed. For example, to properly
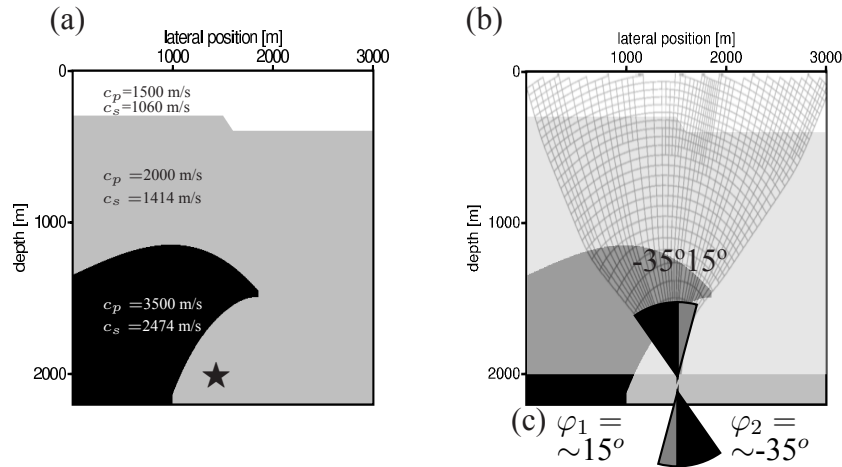
Figure 3.7: (a) Simple salt model. The asterisk denotes the position of the obtained spatial resolution filter. (b) Ray-trace result overlying the simple salt model. (c) Schematically illustrated are the maximum angles of wave propagation that are obtained by ray-tracing, figure (b).

perform prestack depth-migration a macro velocity model of the subsurface is needed, or the effect of statics has to be removed from the recorded data, for more information on seismic processing algorithms we refer to Yilmaz [2001]. In this section the effect on the shape effect of the spatial resolution filter is discussed, then in Chapter 4 the effect on the prestack depth-migrated image is illustrated. Simulating the influence of inversion uncertainties on the shape of the inverted spatial resolution filter is presented in Chapter 6. Both discussions are limited to the zero-offset case, but there is no limitation to apply the following to a common-offset (even with wave conversion).

The forward modeled result of a single unit strength scattering point at $x=$ 1500 m, $z=$ 2000 m in the simple salt model of Figure 3.7 (a) and the prestack depth-migrated response are redisplayed in Figures 3.9 (a) and (b), respectively. The spatial resolution filter is used as a reference case in the following discussion.
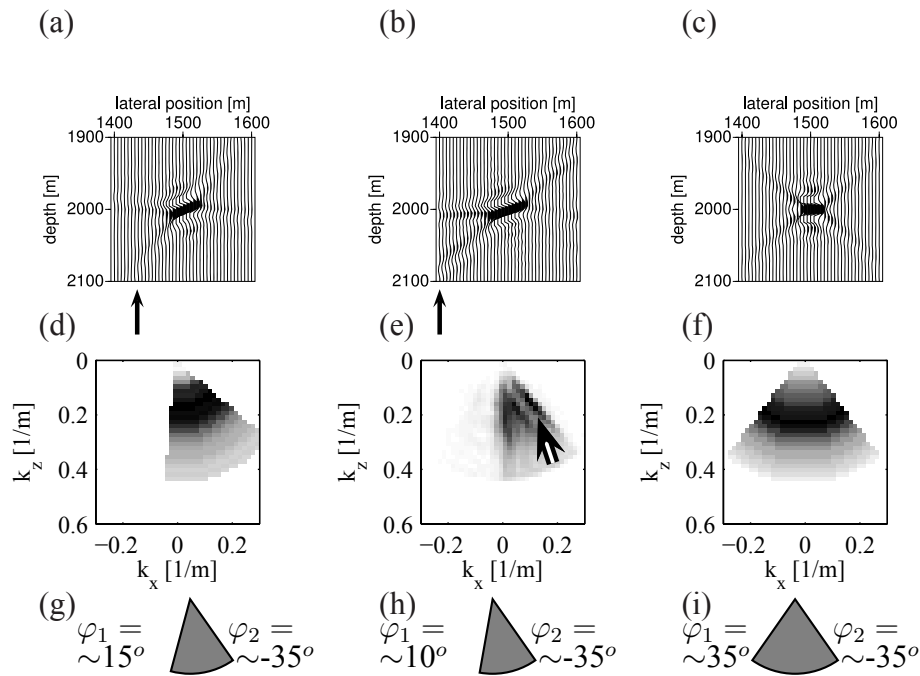
Figure 3.8: Different spatial resolution filters at position x= 1500 m, z= 2000 m in the simple salt model. (a) Local 1D spatial resolution filter. (b) Reference spatial resolution filter. (c) Spatial resolution filter derived in a homogeneous model of 2000 m/s (repeating Figure 3.2 (e)). (d) to (f) show the double-Fourier transformed results of figure (a) to (c). (g) to (i) schematically illustrate the measured maximum angles of wave propagation in the double-Fourier domain.

Influence of a wrong migration velocity model
Finding a macro velocity model to properly prestack depth-migrate the re-corded seismic data is not an easy task. Migrating seismic recordings with a wrong velocity model results in events that are not focused. This does not necessarily mean that these events are not positioned at the proper depth-level. A migration velocity model that is 10% lower than the modeling ve-locity model produces a suboptimal focused spatial resolution filter or frown [Zhu et al., 1998] shown in Figure 3.9 (c).
Next, in the migration velocity model the velocity of the salt body is replaced by 2000 m/s, creating a two layered migration velocity model. The resulting spatial resolution filter is now out of focus in a complicated manner, Fig-ure 3.9 (d). Convolving this result with a shared-earth model illustrates the effect of a wrong migration velocity model, which will help a seismic in-terpreter to understand uncertainties in the seismic data, this is illustrated in Section 4.3.5.

Influence of statics

A static correction is applied to the seismic recordings to correct for the effects of, e.g., variations of elevation [Sheriff, 2001]. In order to simulate the effect of not removing statics on prestack depth-migrated data, the shot record shown in Figure 3.9 (a) is trace-by-trace randomly shifted by 0 or +/- 4 ms, which represent statics. The resulting spatial resolution filter is shown in Figure 3.9 (e), an amplitude effect is shown when compared to the ref-erence case. A normalized difference plot between Figures 3.9 (b) and (e) reveals its cause, a number of isochrons, which are the constituents of a spa-tial resolution filter, are shown in Figure 3.9 (f). Obviously, in the migration process they did not properly cancel due to the introduced static shifts.

Influence of a laterally varying source wavelet

When a shot is fired in a seismic survey, it may be slightly different from the previous one because of a variety of physical conditions that have changed. A spatial resolution filter that has a laterally varying source wavelet is com-puted using the following two steps. Firstly, a shot record with a broad source frequency range (0 to 100 Hz) is computed. Secondly, on a trace-by-

trace basis it is convolved with a Ricker wavelet which the lower and upper frequency ranges are randomly varying between 0 and 10 Hz and 60 and 80 Hz, respectively. The obtained spatial resolution filter is subtracted from the reference case (Figure 3.9 (g)). This results in a filter that has the shape of a spatial resolution filter (Figure 3.9 (h)).

3.3   Discussion of previous research

A new framework has been presented to simultaneously simulate (constrained sparse-spike) inverted and prestack depth-migrated data based on the (inverted) spatial resolution filter (Figure 2.3). In this chapter, the angle and band-limitation filters have been introduced to efficiently obtain a focused zero-offset spatial resolution filter in a laterally variant medium. In the literature four other ways to calculate a focused spatial resolution filter can be found. No publications studied the effect of seismic uncertainties on the spatial resolution filter.

Assuming a homogeneous background model, Chen and Schuster [1999] presented an analytical expression for the zero-offset case. Gelius et al. [2002] use ray-tracing through a laterally variant medium. Special care is taken to correctly simulate the amplitude, a method known as Simulating Migrated Amplitude (SMA) [Laurain et al., 2004]. This thesis introduces the angle and band-limitation filters. The angle filter is obtained after ray-tracing for the maximum angles of wave propagation and the band-limitation filter is constructed by locally stretching the source wavelet. The resulting spatial resolution filter is named a local 1D spatial resolution filter, because only for a layered medium it is exact and locally the medium is assumed to be laterally invariant. Furthermore, this thesis also uses the one-way $x - \omega$ operator of Thorbecke et al. [2004] to compute reference data for the zero-offset and offset case. The list is completed by a finite difference or finite element method that also can be used to compute a spatial resolution filter.

Focusing on the previous results of the homogeneous and simple salt model, for three different categories the listed methods are ranked for their suitability for accurate iterative shared-earth modeling (performed in the next two chapters and the main objective of this thesis). Table 3.1 lists the phase, amplitude and computational costs. The ratings used are $\Box$, $+$,$++$ and $+++$ meaning *not applicable*, *good*, *better* and *very good*.
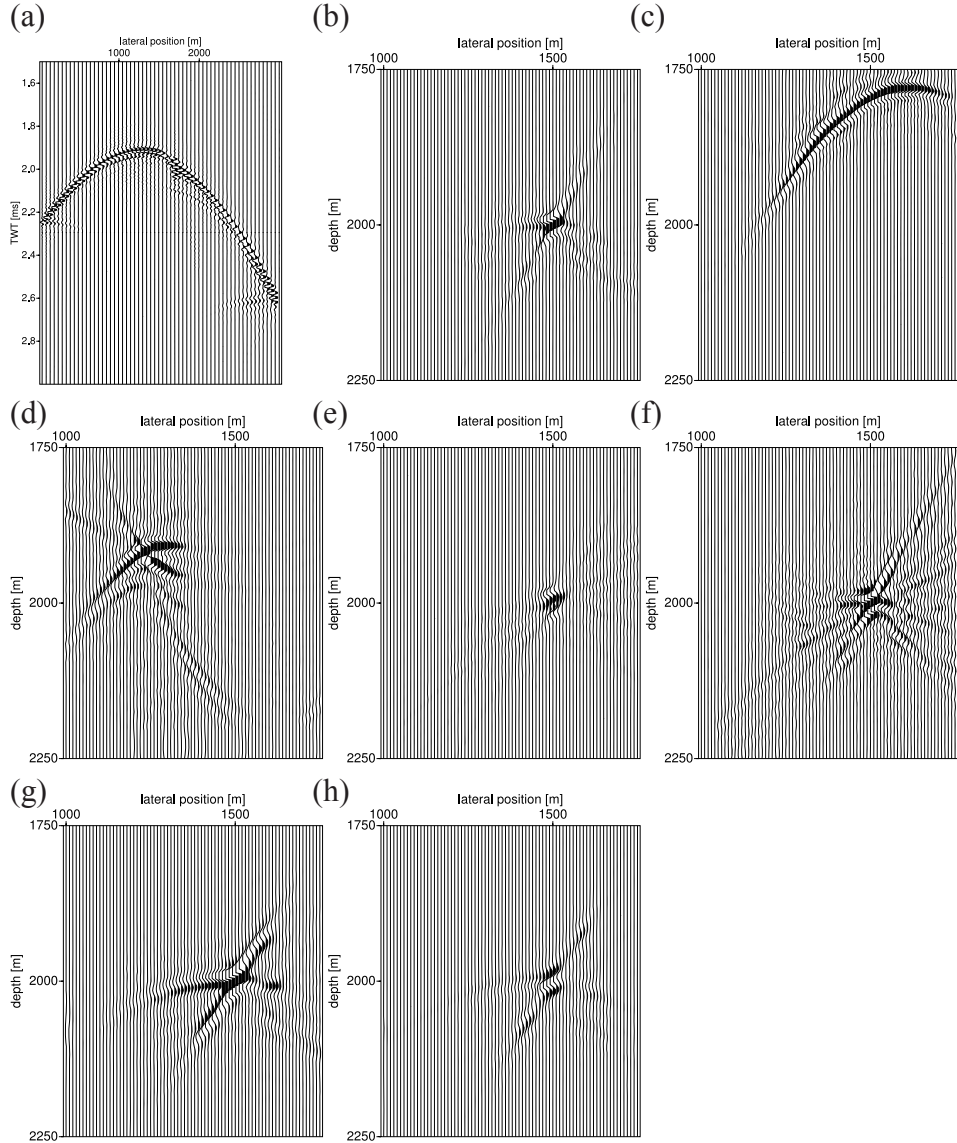
Figure 3.9: (a) Zero-offset shot record of the single unit strength scattering point at the selected position in the simple salt model. (b) Redisplaying Figure 3.8 (b). (c) A suboptimal focused spatial resolution filter. (d) A suboptimal focused spatial resolution filter. (e) Spatial resolution filter after statics is introduced. (f) Normalized difference plot between figures (b) and (e). (g) Spatial resolution filter resulting from a laterally varying source wavelet. (h) Normalized difference plot between figures (b) and (g). The arrows highlight differences between the spatial resolution filters.

As shown in Section 3.2, computing a spatial resolution filter in a laterally variant model, by assuming a homogeneous model results in a too inaccurate filter. The effect of the overburden on especially the phase of the spatial resolution filter is clearly visible. Therefore, in Table 3.1, not applicable ($\square$) is assigned to the methods which assume a homogeneous model. On the other hand, attractive for iterative model is the compute efficient implementation (+++) due to the use of analytical expressions. Unfortunately no analytical expressions are presented for the common-offset case.

The influence of a laterally variant model is incorporated in two ways. Firstly, the maximum angles of wave are used and secondly, assuming locally a 1D medium. In the case of the simple salt model it is concluded that (at least) for the phase of the spatial resolution filter this approximates the one-way $x - \omega$ case reasonably well. The method can obviously be extended in the following two ways. Firstly, the assumption that between maximum angles of wave propagation all angles are present could be removed. This would approach the method of Gelius et al. [2002]. Secondly, the method can also be extended to take care of the amplitude behavior as presented by Laurain et al. [2004]. Therefore, the here presented method is rated ($\square$/+) for the phase part and not applicable for amplitude part. This means that for a relative simple, laterally variant medium (more or less horizontally overburden), the method will simulate accurate data within a limited computational time (++).

A general disadvantage of ray-based methods is that, for complex wave fields, they break down and therefore a complex velocity model is often smoothed to avoid these problems. One-way $x - \omega$ wave field operators do not have this problem. These operators are more accurate for both the phase and amplitude. Only the flexibility of the one-way theory to handle, e.g., also turning rays, is for shared-earth modeling a disadvantage. For the common-offset case, prestack depth-migration is also computationally expensive. Migration based on ray-tracing can in a smoothed laterally variant medium easily handle wave types and is computationally more efficient. Therefore, the ray-tracing method through the full laterally variant medium will produce accurate phase (+) and amplitude (+) behavior of a spatial resolution filter and are flexible (++) in handling different wave types. A spatial resolution filter obtained by one-way wave field operators are more accurate for the phase (++) and amplitude (++) behavior in a complex laterally

variant medium, but is less flexible handling different wave types and more computationally expensive (+).

Finally, to handle accurately both phase (+++) and amplitude (+++) for any wave type in a complex medium, finite element or difference methods could be deployed. Unfortunately, the high computational costs are the bottleneck (□), see Mulder and Plessix [2004] for a recent estimate of 3D finite difference migration.

Method	Phase	Amplitude	Computational costs
Homogeneous model	□	□	+++
Band-limitation and angle filter (this thesis)	+/□	□	++
Full ray-tracing through laterally variant medium	+	+	++
$x - \omega$ One-way operator	++	++	+
Finite difference or finite element method	+++	+++	□

Table 3.1: Compute efficiently, deriving an accurate spatial resolution filter, using different methods presented in literature. □ is not applicable; + is good; ++ is better and +++ is very good.

4

Validation tests

4.1 Introduction

The goal of this validation chapter is to demonstrate the ability of the in
Chapter 2 presented framework to accurately simulate prestack depth-mi-
grated and inverted data that can be compared directly with reference data.
Therefore, three different geological models are investigated.

The first model consists of dipping homogeneous layers, in order to in-
vestigate the difference in blurring and suppression of geological dips of
prestack depth-migrated seismic data. The data are simulated using the pre-
sented framework that uses different spatial resolution filters and using the
1D convolution model. Next, the results of inverting the prestack depth-
migrated data making use of the 1D convolution model, migration-decon-
volution method and a band-limitation filters are compared to each other.
The band-limitation filter is proposed as an alternative filter in the migration-
deconvolution method. Finally, the different inverted results are simulated
using the angle and approximated angle filter, respectively.

The second model is a representation of one-half of a graben structure, which
is for example found on the margins of the south Atlantic Ocean. A marine

survey, used to probe the geological structure, had a too limited recording aperture such that only a part of the structure is imaged on the prestack depth-migrated and constrained sparse-inverted reference data-sets. Simulating prestack depth-migrated and constrained sparse-spike inverted seismic data making use of spatial resolution filters will help a seismic interpreter to understand the effect of a limited recording aperture on the shared-earth model.

The third model represents the complex geological setting found on the Sigsbee escarpment in the deepwater Gulf of Mexico. The acquisition and processing steps to obtain the reference prestack depth-migrated and constrained sparse-spike inverted data resemble that of a present day real data-set. The complex overburden makes geological interpretation of the target-zone under the massive salt body a real challenge. The interpreter can test different geological ideas by simultaneously simulating offset prestack-migrated and constrained sparse-spike inverted data. The ability to also simulate common-offset data, will help the seismic interpreter to understand seismic uncertainties, e.g., randomly imaged multiple scattering.

4.2   A dipping layer model

A geological model, starting at a depth of 2550 m, consisting of seven velocity layers. The interfaces have dips of $0°$, $30°$, $45°$, $60°$ and $75°$, respectively (Figure 4.1 (a)). Using the normal-incidence assumption, their reflectivity strengths are 0.05, 0.03, -0.04, 0.07 and 0.06 (Figure 4.1 (b)). Additionally, the reflectivity model contains two gaps of 8 and 20 m, respectively in the uppermost layer. Obviously, these gaps do not exist in a real geological model, but are included to illustrate the horizontal smearing of a prestack depth-migrated image.

■ 4.2.1   Simulating prestack depth-migrated seismic data

It is assumed that the dipping structure is buried in a homogeneous background model with a constant P-wave velocity of 2000 m/s. The constant velocity is used to time-depth convert a Ricker wavelet with a peak frequency at 25 Hz to depth (Figure 4.1 (c)). In the 1D convolution method, the source signature is convolved with the normal-incidence reflectivity data to simulate

a 1D seismic image (Figure 4.1 (e)). A spatial resolution filter is obtained using the same input wavelet and the total recording aperture is chosen such that the maximum angles of wave propagation are $\pm 70°$ (Figure 4.1 (d)). A prestack depth-migrated seismic image is simulated by performing a multidimensional spatial convolution between the normal-incidence reflectivity model and the spatial resolution filter (Figure 4.1 (f)).

In the following discussion, the two simulated seismic images are compared on three aspects; firstly, suppression and blurring of geological reflectors, secondly, migration wavelet stretch and thirdly, horizontal smearing.

Firstly, when counting the number of seismic events in Figures 4.1 (e) and (f) it is observed that the $75°$ dip is not imaged in Figure 4.1 (f). This is directly related to the chosen maximum angles of wave propagation of $\pm 70°$. A spatial resolution filter suppresses geological dips that are outside its range of angles of wave propagation, similar as in migration (we refer to Beylkin and Burridge [1984], Chapter 4 of Bleistein et al. [2000] and Lecomte et al. [2003]).

The previous discussion can also be illustrated in the double-Fourier domain (Figure 4.2). Again, six reflectivity layers are counted in Figure 4.2 (a), it is noted that the $30°$ and $45°$ dips are very close to each other. By multiplying (equivalent of a spatial convolution in the space domain) of the reflectivity model with the 1D wavelet filter (Figure 4.2 (b)), all reflectors are imaged (Figure 4.2 (d)). The spatial resolution filter (Figure 4.2 (c)) suppresses the $75°$ reflector due to the $70°$ maximum angles of wave propagation restriction (Figure 4.2 (e)).

If the acquisition setup or the geological overburden over the target is changed such that it is illuminated with a spatial resolution filter with φ_1 and φ_2 of $\pm 25°$, respectively (Figure 4.3 (a)). Now only the horizontal event is imaged in the prestack migrated image (Figure 4.3 (c)). Next, the total recoding aperture is modified such that, φ_1 and φ_2 are $\pm 80°$, respectively (Figure 4.3 (b)). The simulated prestack depth-migrated result is shown in Figure 4.3 (d). It shows that all interfaces are imaged.

Secondly, the shapes of the wavelet in the different seismic results are compared. A trace at a lateral position of 190 m is selected from the images created with the 1D convolution model and the $70°$ spatial resolution filter and compared in Figure 4.4. Both simulated results have the same peak and trough values, which correspond to the reflectivity values. However, with

increasing geological dip angle the wavelet of the migrated image obtained with the spatial resolution filters is stretched. This feature also occurs in real data migration and is known as migration wavelet stretch [Wapenaar et al., 1999]. This stretch amounts to 1/cos(angle of geological dip) in two dimensions. Thus, at a $60°$ geological dip the wavelet resulting from using the spatial resolution filter is twice as long wavelet, as illustrated by two arrows in Figure 4.4 (a).

Thirdly, the influence of the two gaps of 8 and 20 m in the reflectivity model are investigated by considering a horizontal slice at 2575 m through the images of Figures 4.1 (e) and (f). Both methods show the same amplitude values (away from the gaps and edge), but their responses differ around the gaps (Figure 4.5). The 1D convolution method represents both gaps correctly, and it represents the values of the normal-incidence model. The $70°$ spatial resolution filter has almost smeared the gap of 8 m, similar as would happen in migration. This illustrates that besides the vertical resolution, it is also expresses the horizontal resolution of a prestack depth-migrated image. The horizontal resolution is quantified by $\lambda/(4 sin(\varphi))$ [Claerbout, 1976; Chen and Schuster, 1999]. Here, $\lambda = \frac{c}{f}$, with $c = 2000$ m/s and $f = 70$ Hz, which results in a horizontal resolution of approximately 8 m. As the formula shows, the horizontal resolution depends on the maximum angles of wave propagation. As a result, depending on the maximum angles of wave propagation, the gaps are completely smeared or imaged, respectively illustrated by the two circles in Figures 4.3 (c) and (d). The vertical resolution is quantified by $\lambda/4$ [Kallweit and Wood, 1982; Vermeer, 2001]. This shows that the horizontal resolution is less than the vertical resolution (for $\varphi < 90°$).

■ 4.2.2 Inverting prestack depth-migrated seismic data

In order to test simulating (constrained sparse-spike) inverted data, the simulated prestack depth-migrated image of Figure 4.1 (f) is inverted using the following three steps.

In step one, the seismic wavelet is removed in the double-Fourier domain using three different inversion filters. *(a)* A 1D inversion wavelet (Figure 4.1 (c)) creates a constrained sparse-spike reference set. *(b)* A $70°$ spatial resolution filter (Figure 4.1 (d)) is used to perform migration-deconvolution [Yu
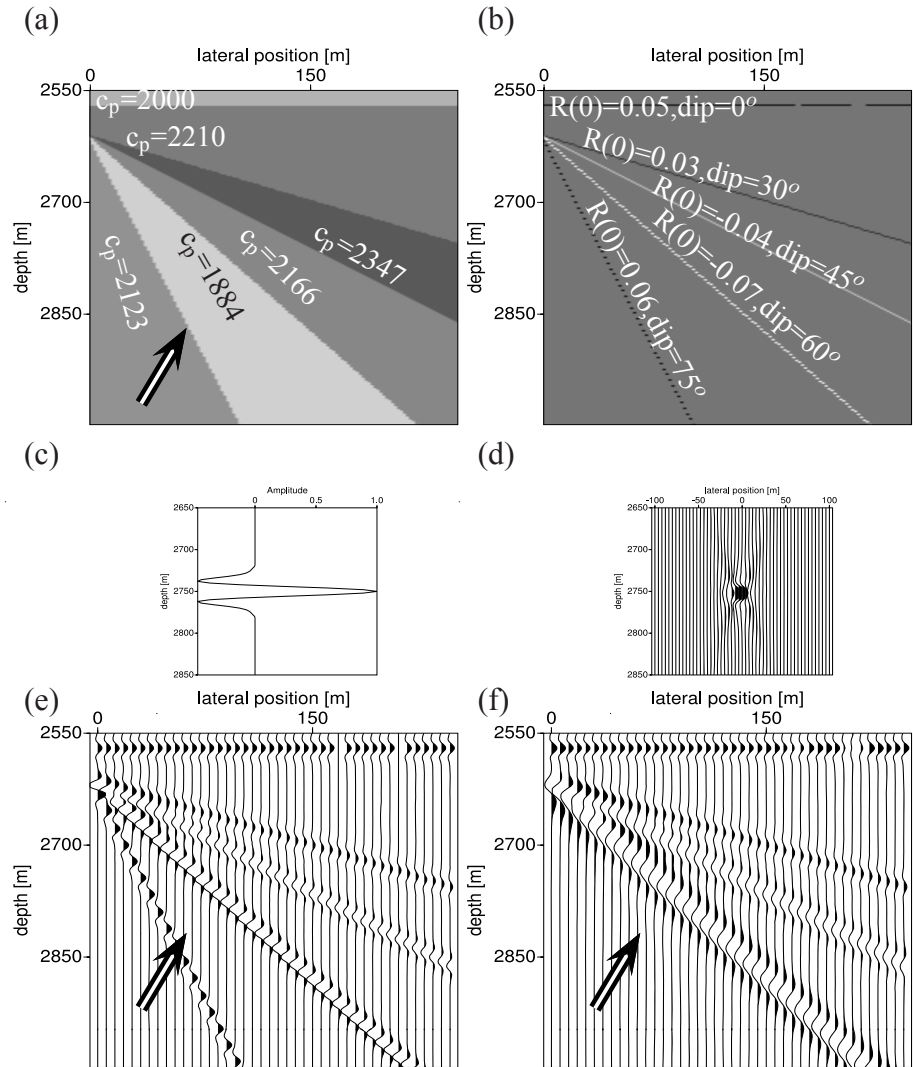
Figure 4.1: (a) A dipping layer model, with velocities in m/s. (b) Normal-incidence reflectivity model. (c) A 1D wavelet. (d) A 70° *spatial resolution filter. (e) The 1D convolution model result using the 1D wavelet of figure (c). (f) The prestack depth-migrated data using the spatial resolution filter of figure (d). The arrows highlight the* 75° *dip.*
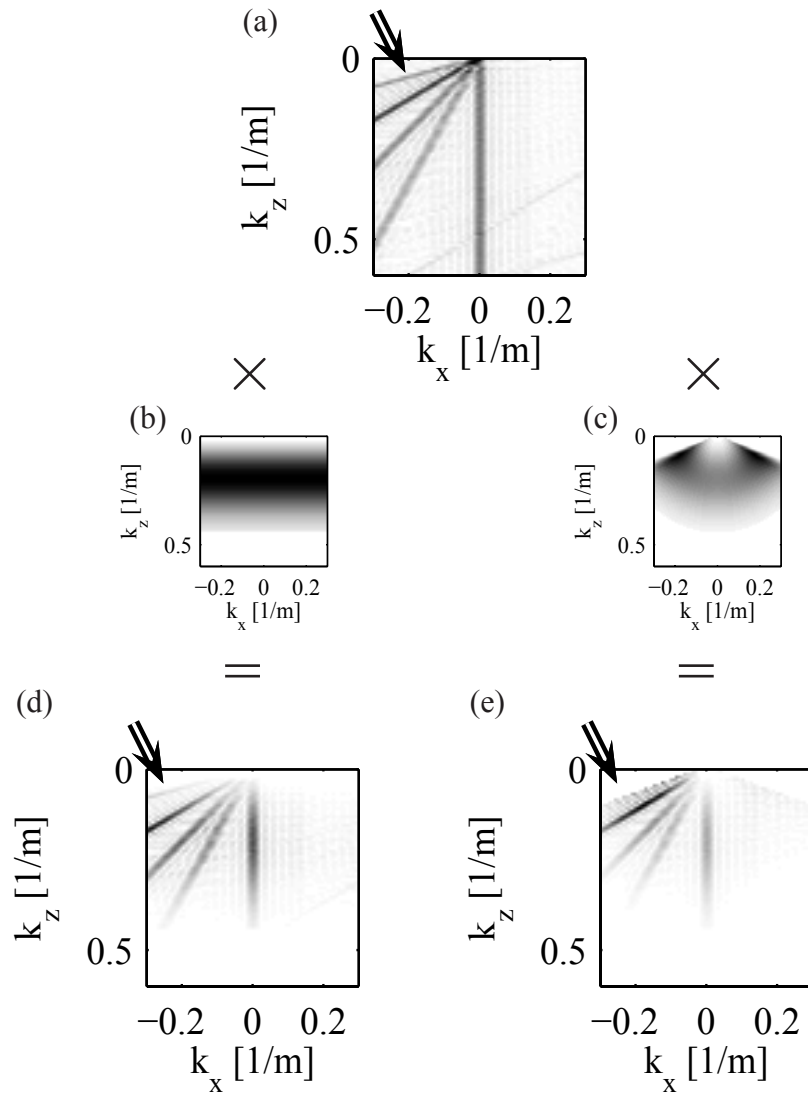
Figure 4.2: (a) to (e) Double-Fourier transformed images of Figures 4.1 (b) to (f). Dot denotes multiplication. Arrows highlight the 75° dip. The 75° dip is imaged by filtering the shared-earth model with the 1D wavelet (1D convolution model). The 75° dip is not images by filtering the shared-earth model by the 70° spatial resolution filter. × denotes multiplication.
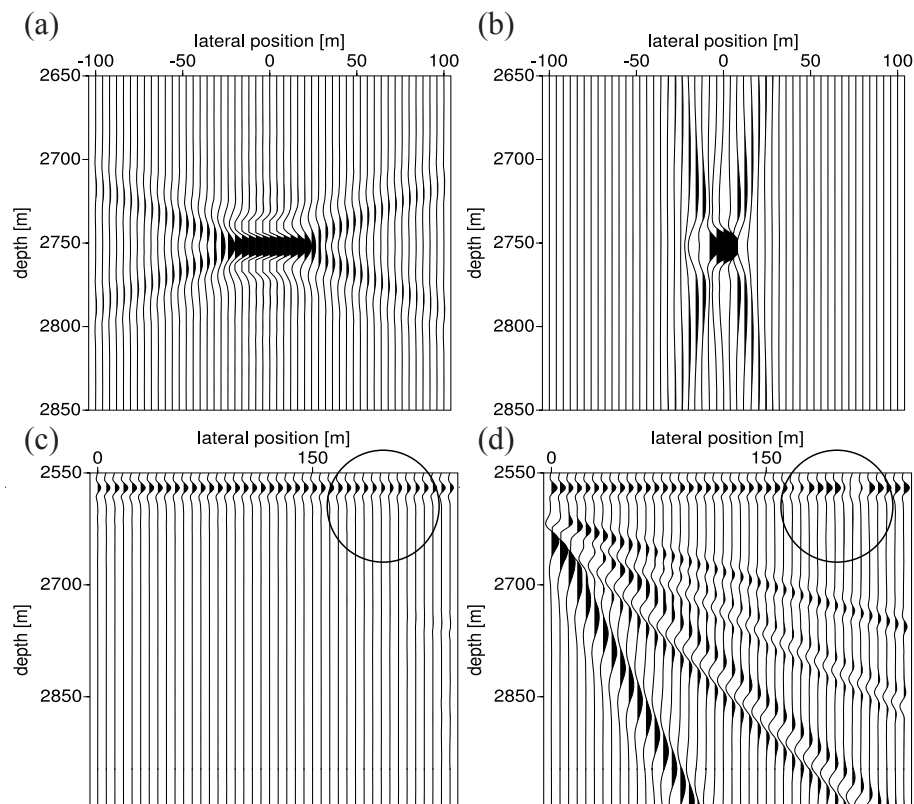
Figure 4.3: (a) A $25°$ spatial resolution filter. (b) A $80°$ spatial resolution filter. (c) The prestack depth-migrated data using the spatial resolution filter of figure (a). (d) The prestack depth-migrated data using the spatial resolution filter of figure (b). The circles highlight the difference in horizontal resolution.
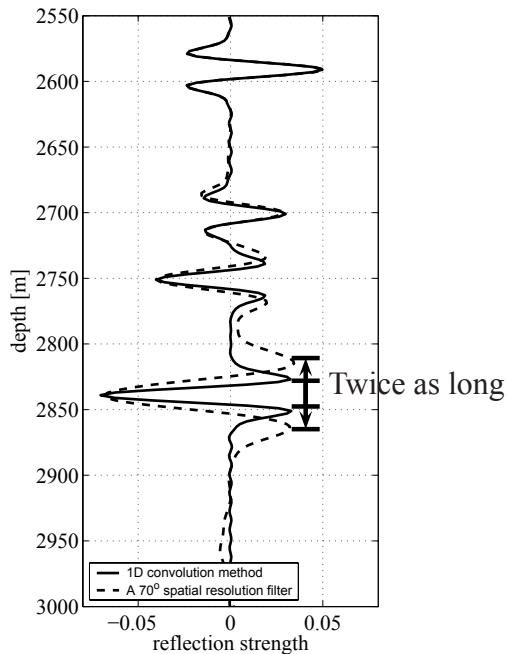
Figure 4.4: A trace comparison at lateral position 190 m of Figures 4.1 (e) and (f). The two arrows highlight that the 1D convolution model does not simulate migration wavelet stretch.

et al., 2006]. *(c)* A band-limitation filter (Figure 4.6 (d)) is used as an alternative inversion filter in the migration-deconvolution approach.

In step two, low-frequency information is added trace-by-trace from one well log at lateral position of 80 m, to compensate for the low-frequency filtering of the source wavelet. It constitutes an approximation, since only at the selected lateral position the reconstruction of the low-frequency content is restoring filtered information completely.

Finally in step three, all traces are integrated in the form of a cumulative sum and shifted with a constant impedance value obtained from the well-log position [Ferguson and Margrave, 1996]. It is observed that the resolution of the constrained sparse-spike result is more blurred than the migration-deconvolution and band-limitation images, in particular focus at the $75°$
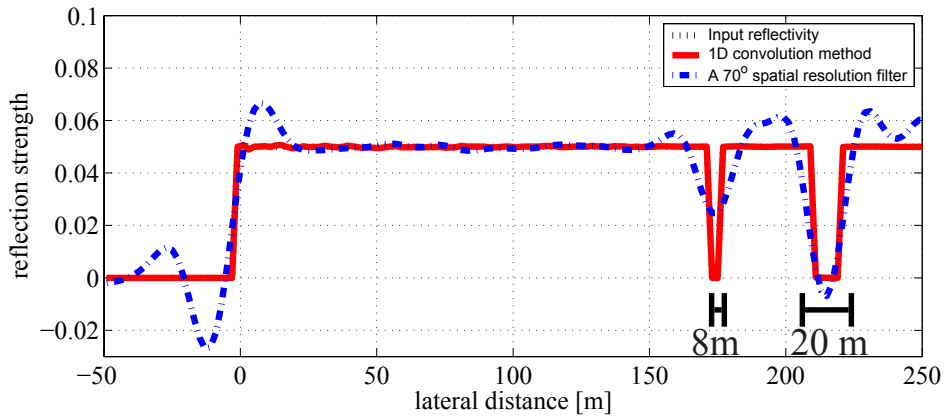
Figure 4.5: A depth slice through the horizontal reflector of Figures 4.1 (e) and (f). The gaps illustrate, the horizontal smearing of a 70° spatial resolution filter. The 1D convolution model images both gaps; only the 20 m gap is imaged by the spatial resolution filter. The 1D convolution model result is overlying the input reflectivity data.

(Figures 4.6 (b), (a) and (c), respectively). In order to investigate this in more detail, at lateral positions 20, 80 and 120 m, traces from the impedance model (Figure 4.1 (a)) and the different computed inverted impedance images are selected and shown in Figure 4.7 (a).

The comparison among the three traces shows that the impedance results from the migration-deconvolution and band-limitation filter match each other closely. When comparing the constrained sparse-spike inversion to the migration-deconvolution results, it is observed that up to a geological dip of $\sim$ 25° all inverted results are comparable. However, with increasing geological dip the constrained sparse-spike inversion algorithm does not properly account for the wavelet stretch and horizontal smearing, this results in amplitude and phases errors and subsequently a decrease in resolution.

Finally, the influence of adding low-frequency information from only one well log is that at the depth of the 75° dip in the selected well log (2900 m), the impedance values of the neighboring traces deviate from the impedance value of the selected well log. Thus, for the neighboring traces, the depth of the 75° dip appears at the wrong depth location, illustrated by the arrow and the horizontal line in Figure 4.7 (a).
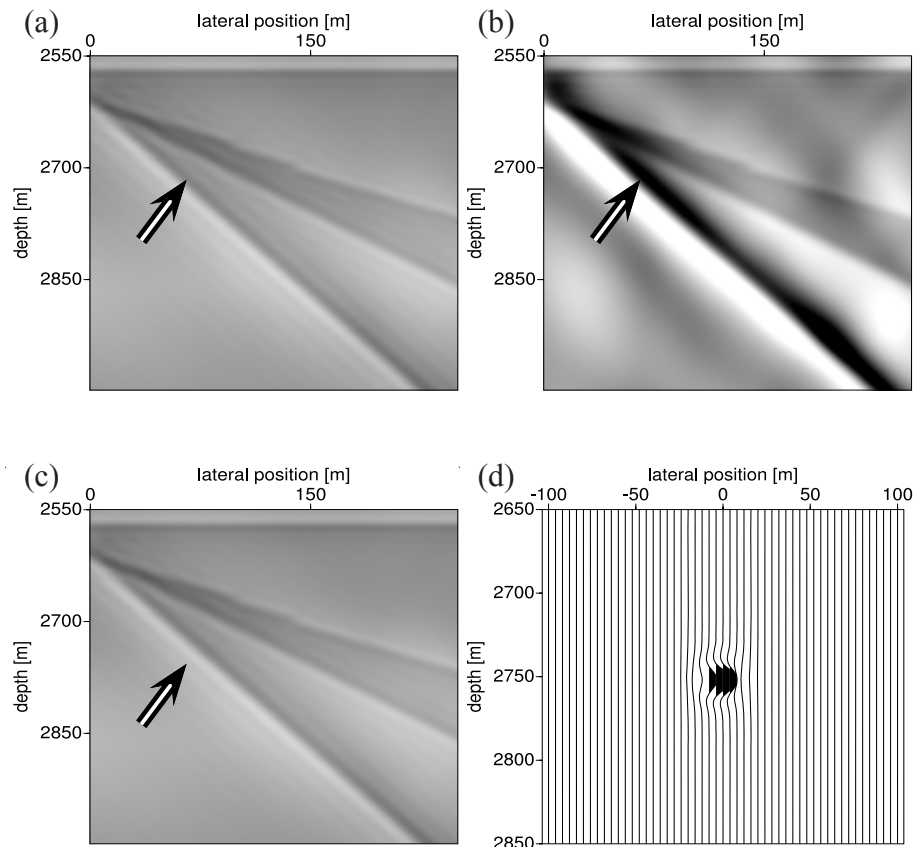
Figure 4.6: *An impedance result of inverting the prestack depth-migrated image of Figure 4.1 (f) using three different inversion methods. (a) The migration-deconvolution method. (b) A constrained sparse-spike inversion approach. (c) A band-limitation filter as an alternative filter in the migration-deconvolution process. (d) A band-limitation filter. The arrows highlight the $75°$ reflector dip.*
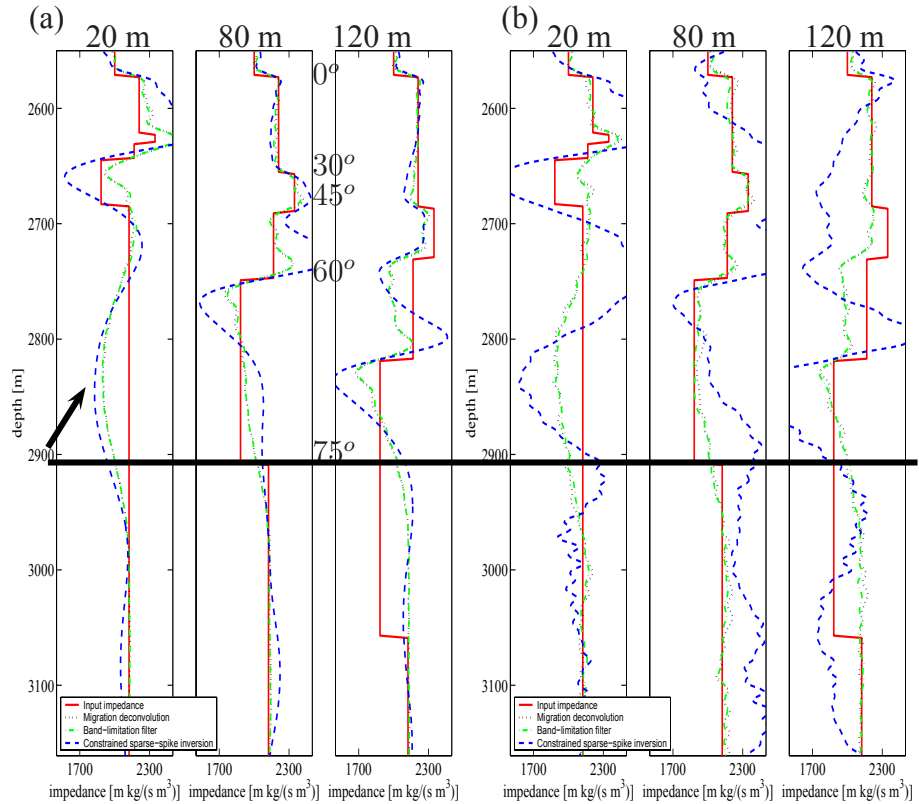
Figure 4.7: *(a) Trace comparison at lateral positions of 20, 80 and 120 m of Figures 4.1 (a) and 4.6 (a) to (c). (b) Trace comparison at lateral positions of 20, 80 and 120 m of Figures 4.1 (a) and 4.8 (b) to (d). The black line and arrow illustrate the effect of the low-frequency model.*

Band-limitation filter, a new inversion filter?

The inverted results using the band-limitation filter and spatial resolution filter method (migration-deconvolution), were shown to match each other very closely. The band-limitation filter is used as an inversion filter, by realizing that ideally the migrated real data do not have any information outside the maximum angles of wave propagation. The advantage of using the band-limitation filter is that it does not require a detailed overburden velocity model of the target to derive exact information on the maximum angles of wave propagation (φ_1 and φ_2).

However, by inverting beyond the maximum angle content of the seismic data, noise can easily be boosted. In order to investigate this issue, randomly distributed noise is added to the prestack depth-migrated result (Figure 4.1 (f)). The result is shown in Figure 4.8 (a). The previous described inversion steps are then used to obtain Figures 4.8 (b) to (d). At lateral positions 20, 80 and 120 m, traces from the impedance images are selected, which shows that the band-limitation filter still matches the migration-deconvolution result (Figure 4.7 (b)). This demonstrates that the band-limitation filter impedance result is not affected severely by the added noise. On the other hand however, the constrained sparse-spike result shows serious amplitude and phase problems. Further tests with the band-limitation filter, e.g., on real data, are beyond the scope of this thesis.

■ 4.2.3 Simulating inverted data

The constrained sparse-spike and migration-deconvolution inversion results shown in Figures 4.6 (a) and (b) are used as reference data to test simulated inverted data.

The migration-deconvolution image is simulated by in two steps. Firstly, by filtering the reflectivity model with an angle filter (Figure 4.9 (a)). Secondly, the low-frequency model is added to the filtered result and an integration and a scaling step are performed to simulate a migration-deconvolution image (Figure 4.9 (c)). The image matches nicely with the reference result. This also shown in more detail by Figure 4.10 (a) that comparison traces at lateral positions, 20, 80 and 120 m of Figures 4.1 (a), 4.6 (a) and 4.9 (c).

The result of the constrained sparse-spike inversion method is simulated by filtering the reflectivity model with an approximated angle filter (Figure 4.9
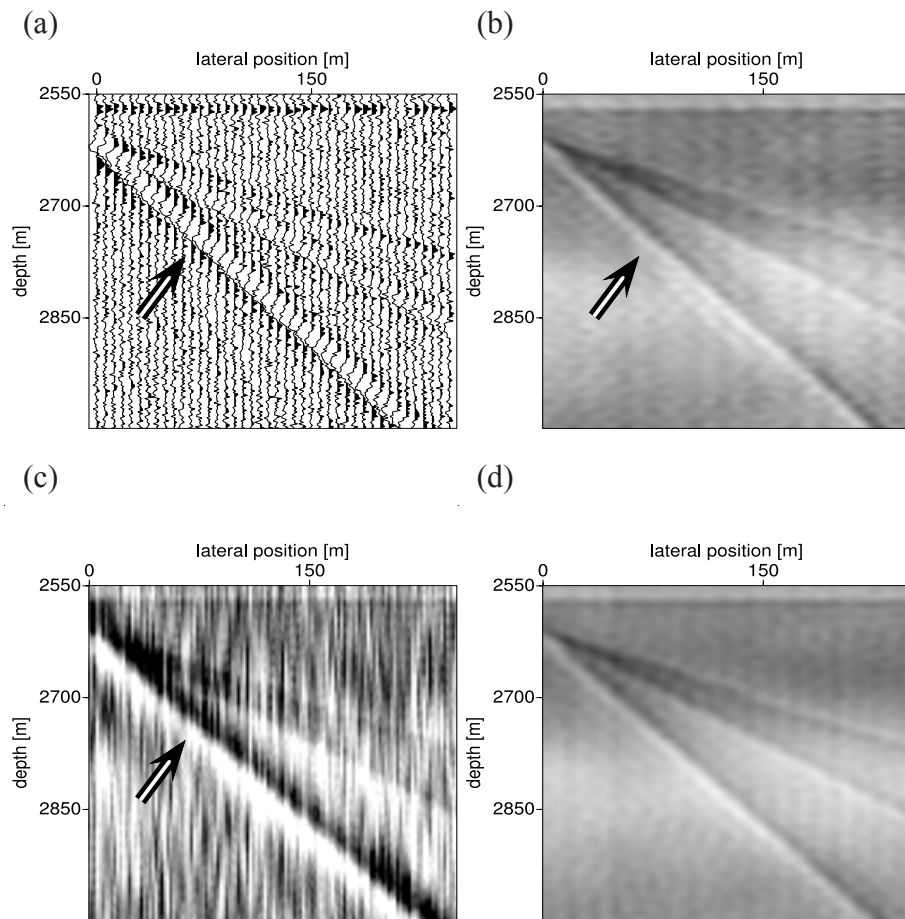
Figure 4.8: *(a) Result after adding random noise to the prestack depth-migrated im-age of Figure 4.1 (f). (b) Inverted result using the migration-deconvolution method. (c) Constrained sparse-spike inversion result. (d) Using a band-limitation filter in the migration-deconvolution method. The arrows highlight the* 75° *reflector dip.*
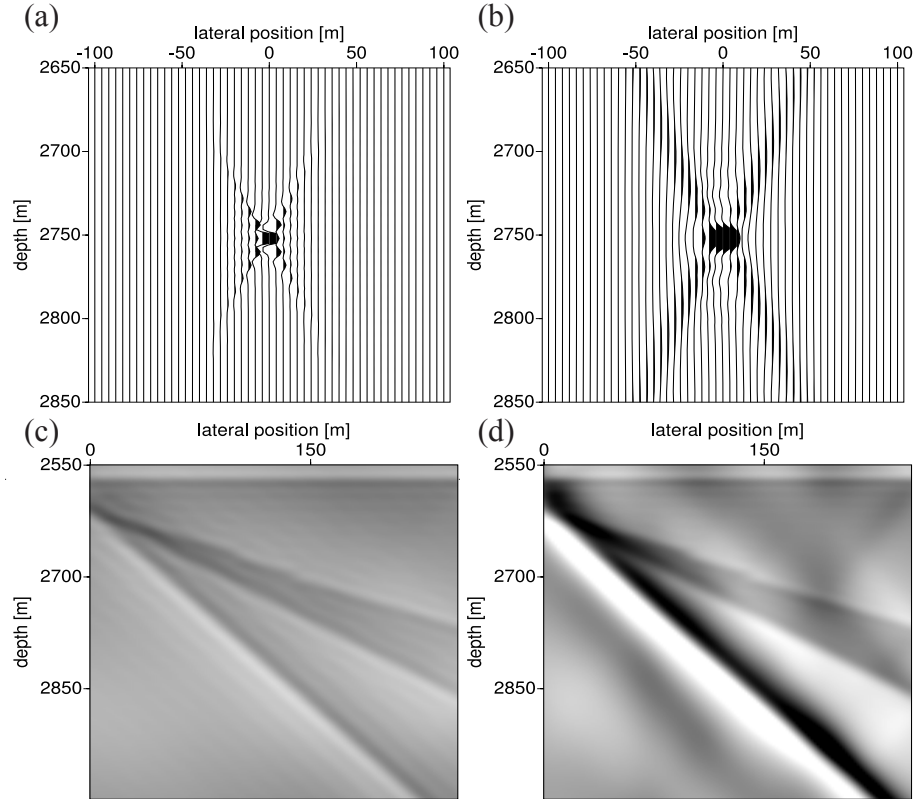
Figure 4.9: (a) An angle filter. (b) An approximated angle filter. (c) A simulated migration-deconvolution impedance image. (d) A simulated constrained sparse-spike impedance image.

(b)) and repeating the second step to compute the simulated image (Figure 4.9 (d). Again, the simulated result nicely matches the trend of the reference result. This is shown in more detail by a trace comparison in Figure 4.10 (b). This figure compares traces at lateral positions, 20, 80 and 120 m from Figures 4.1 (a), 4.6 (b) and 4.9 (d).
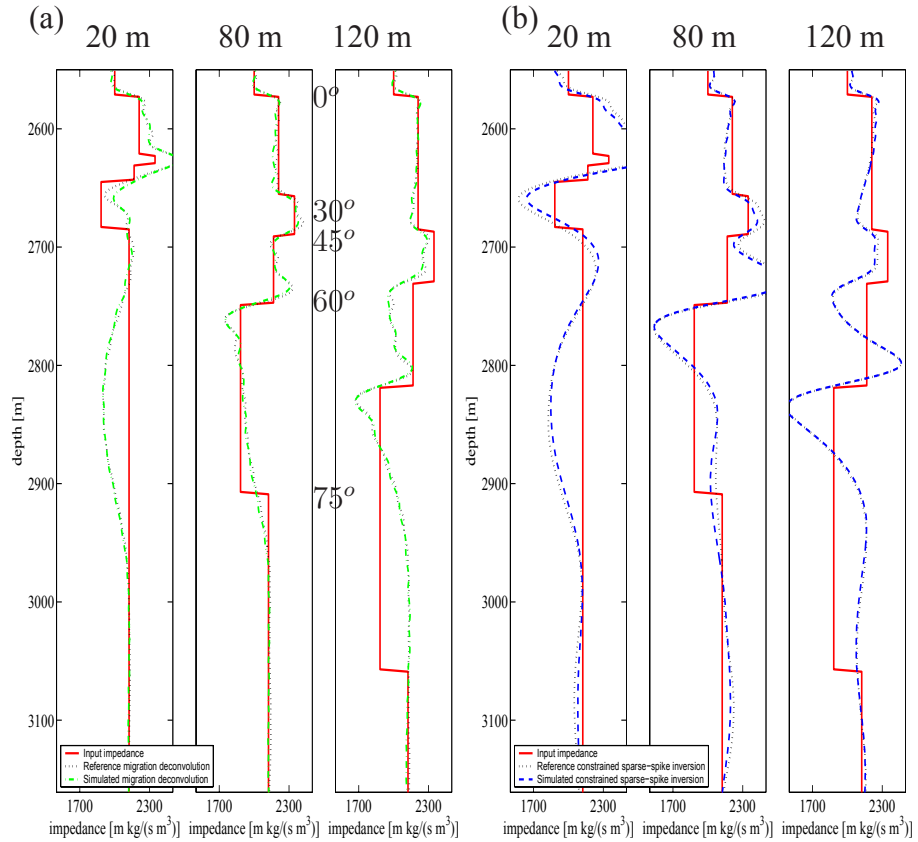
Figure 4.10: (a) A trace comparison at lateral positions, 20, 80 and 120 m of Figures 4.1 (a), 4.6 (a) and 4.9 (c). (b) A trace comparison at lateral positions, 20, 80 and 120 m of Figures 4.1 (a), 4.6 (b) and 4.9 (d).

4.3 Evaluating enhanced reservoir characterization: graben model

The geological structure found on the margins of the South Atlantic Ocean is an one-half of a graben, Figure 4.11 (a), a model inspired by Mittet et al. [1995]. A reference data-set simulating a marine acquisition spread using an acoustic finite difference scheme is designed such that the steeply dipping faults of the graben structure are not illuminated. The survey has a detector length of 800 m, with a spread and detector spacing of 10 m (illustrated by the black arrow in Figure 4.11 (a)). The source signature is a Ricker wavelet with a peak frequency at 25 Hz and a sampling of 4 ms. Subsequently, the shot records are prestack depth-migrated. In order to obtain a focused result, the velocity field of the forward modeling is also used as input to the migration algorithm.

The dashed box of Figure 4.11 (a) indicates the selected target-zone which is of interest for seismic interpretation. The enlarged reference image is shown in Figure 4.11 (b).

The objective is to match the phase of the reference image as well as possible using the 1D convolution model and with the presented framework using a zero-offset spatial resolution filter and the normal-incidence assumption (see also discussion in Section 2.5). The main reason for considering the phase only is the prestack depth-migration algorithm used to create the reference depth image is not preserving the amplitude.

Using the velocity trace at 1200 m, the source wavelet of the reference survey is time-to-depth converted. In the 1D convolution model the normal-incidence reflectivity model of the graben model is convolved with a time-to-depth converted Ricker wavelet to simulate the enlarged 1D seismic image of Figure 4.12 (a).

■ 4.3.1 Simulating zero-offset prestack depth-migrated seismic data

A prestack depth-migrated seismic image is simulated by performing a multidimensional spatial convolution between the normal-incidence reflectivity model and one zero-offset local 1D spatial resolution filter (Figure 4.12 (b)). This is a direct extension of the 1D convolution model, where only in the

vertical direction a convolution is performed between a source wavelet and an earth model.

The zero-offset local 1D spatial resolution filter is obtain by constructing an angle and a band-limitation filter. The maximum angles of wave propagation are needed to compute an angle filter. This angle information is computationally efficient obtained using the following approach: ray-tracing is performed through a smoothed version of the velocity model by only shooting rays from the two outer grid-points of the acquisition setup (Figure 4.13 (a)). At every location in the earth model the maximum angle of wave propagation is found by taking the opposite of the wavefront and measuring the angle with the vertical. Going from left to right in Figure 4.13 (b), it is shown that the angle of φ_2 is increasing due to the overburden and the reverse trend is observed for the value of φ_1 that is caused by the fact that the outer boundary of the acquisition setup is reached.

The band-limitation filter is constructed from the time-to-depth converted Ricker wavelet.

■ 4.3.2 Discussion on the simulated zero-offset seismic data

The comparison between Figures 4.11 (b), 4.12 (a) and (b), starts around the area indicated by the double arrow. The limited recording aperture has caused that the steeply dipping faults are not imaged in the reference image. This is not simulated by the 1D seismic image, but in the local 1D prestack depth-migrated image the steepest dipping fault is suppressed. Or in other words, the reference prestack depth-migrated and simulated local 1D prestack depth-migrated image both include effects of the limited recording aperture, limited source bandwidth and propagation effects in the overburden. That a spatial resolution filter acts as two different filters is also observed: the angle filter has suppressed the steepest dipping fault and the band-limitation filter has blurred all geological boundaries in the reflectivity model.

When moving away for the previous selected area, the match between the reference and simulated prestack depth-migrated image gets poorer. This is because the spatial resolution filter is only locally valid, a spatial resolution filter varies with both the depth and the lateral position. In order to investigate this, nine equally spaced local 1D spatial resolution filters from $x=$

1100 m, z= 1100 m to x= 1500 m,z= 1500 m are computed and convolved with nine equally sized areas of the normal-incidence reflectivity model. After summing the individual results, a local 1D prestack depth-migrated image is simulated (Figure 4.14 (a)). Three of the nine spatial resolution filters are shown below this figure in the space-depth and double-Fourier domain. It is observed that going from left to right the spatial resolution filter becomes increasingly more asymmetric, because as discussed the maximum angles of wave propagation change. In order to verify this result a $x - \omega$ prestack depth migrated image is simulated using nine $x - \omega$ spatial resolution filters through the un-smoothed velocity model (Figure 4.15 (b)).

The phase of the reference image is much better simulated by the prestack depth-migrated images based on more spatial resolution filters (Figures 4.12 (b), 4.14 (a) and 4.15 (a)). Using a higher number of spatial resolution filters results in that also in the area indicated by the single arrow the faults are correctly suppressed. However, the area indicated by the circle shows that in the local 1D prestack depth-migrated image the fault is not suppressed enough. By comparison of the local 1D and the $x - \omega$ spatial resolution filter at x= 1100 m, z= 1300 m in the double-Fourier domain, it is revealed that the angle range obtained from ray-tracing is wider (illustrated by the solid line in Figures 4.14 (b) and 4.15 (b)). This can result from the fact that a smoothed velocity field is used in the ray-tracing, or additionally the fact that only the outer acquisition points are used to calculate the maximum angles of wave propagation, may both play a role. Ideally from each subsurface point rays are propagated to the subsurface, but this is more computationally expensive. The total computation time for this 2D model is approximately *minutes* for the simulated images and *hours* for the reference case.

■ 4.3.3 An averaged horizontal-resolution attribute map

Additionally, the derived angle information is used to compute a horizontal-resolution attribute map according to $\lambda/(4sin(\varphi))$ and $\lambda = \frac{c}{f}$ [Claerbout, 1976; Chen and Schuster, 1999; Vermeer, 2001]. For c the local wave velocity and for f the center frequency of 31 Hz are chosen. Because, the maximum angles of wave propagation are laterally varying, for each φ_1 and φ_2 a horizontal resolution map is computed, averaging produces an averaged horizontal-resolution attribute map. It is observed that around the steeply

(a)

(b)
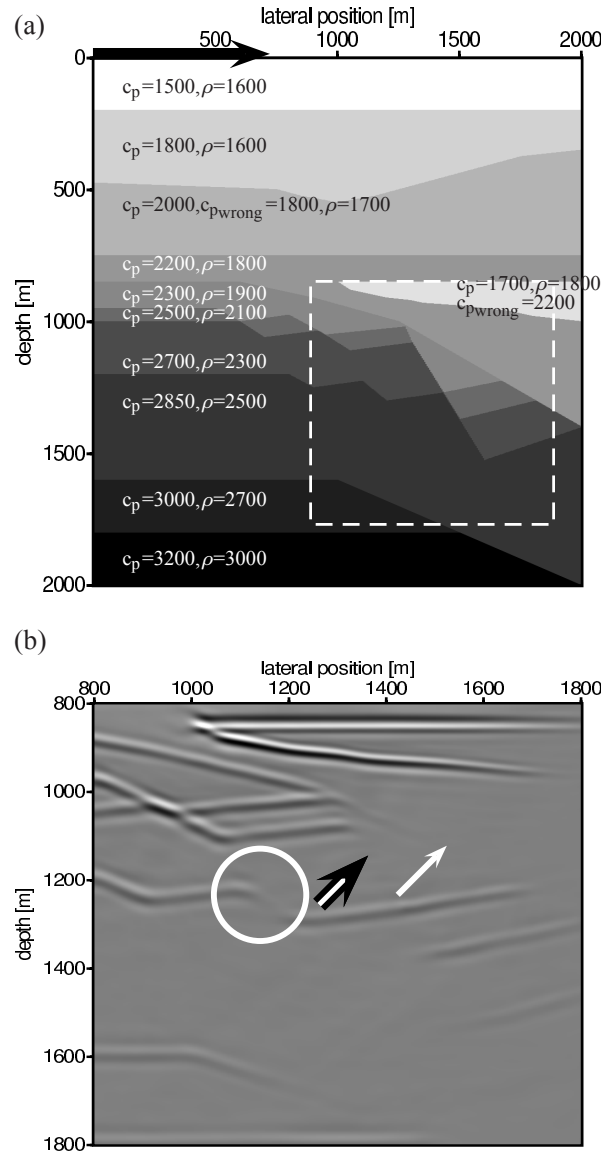
Figure 4.11: (a) One-half of a graben model. Unit of the P-wave velocity values is m/s and the unit of rock-density is kg/m³. The black arrow indicates the direction and length of the detector array. The following images correspond to the area outlined by the dashed box: (b) Reference prestack depth-migrated image using the velocity model (figure (a)) in the prestack depth-migration algorithm. The white arrow, double arrow and circle indicate areas where the match between reference and different simulated images is discussed.

(a)

(b)
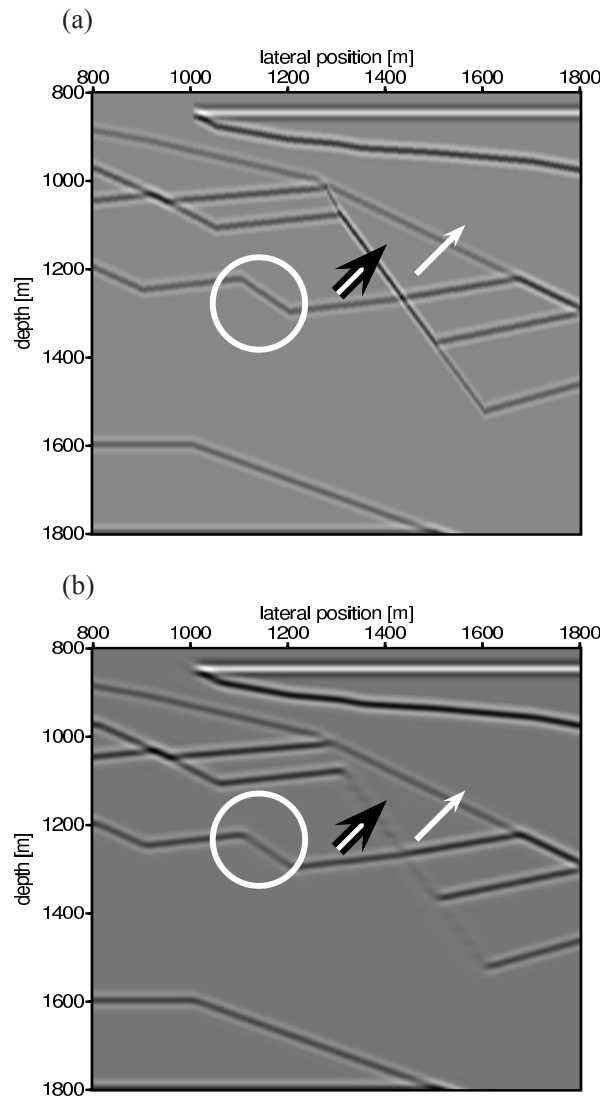
*Figure 4.12: (a) A 1D seismic image, result of the 1D convolution model. (b) A simulated prestack depth-migrated image using one local 1D spatial resolution filter at x= 1200 m and z= 1200 m. The white arrow, double arrow and circle indicate areas where the match between reference and different simulated images is discussed.*
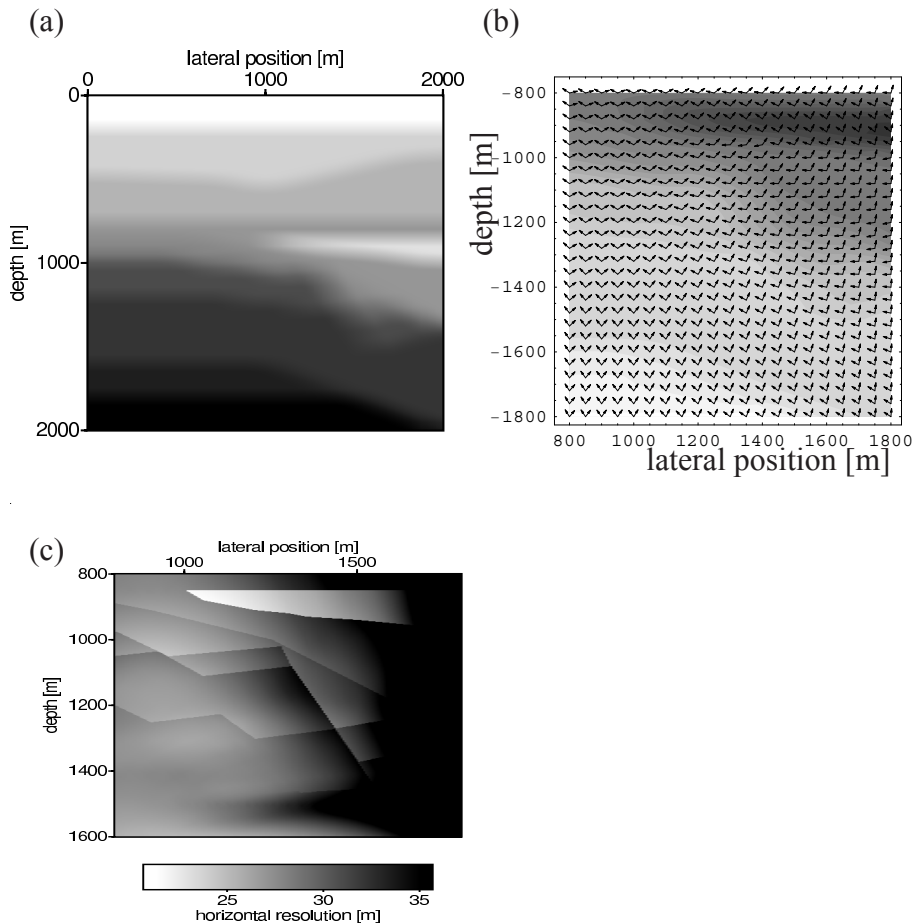
Figure 4.13: (a) Smoothed velocity model of Figure 4.11 (a). The following images correspond to the area outlined by the dashed box in Figure 4.11 (a). (b) Left and right maximum angles of wave propagation superimposed on the smoothed velocity model of figure (a). (c) A map of the averaged horizontal-resolution.

(a)

(b)
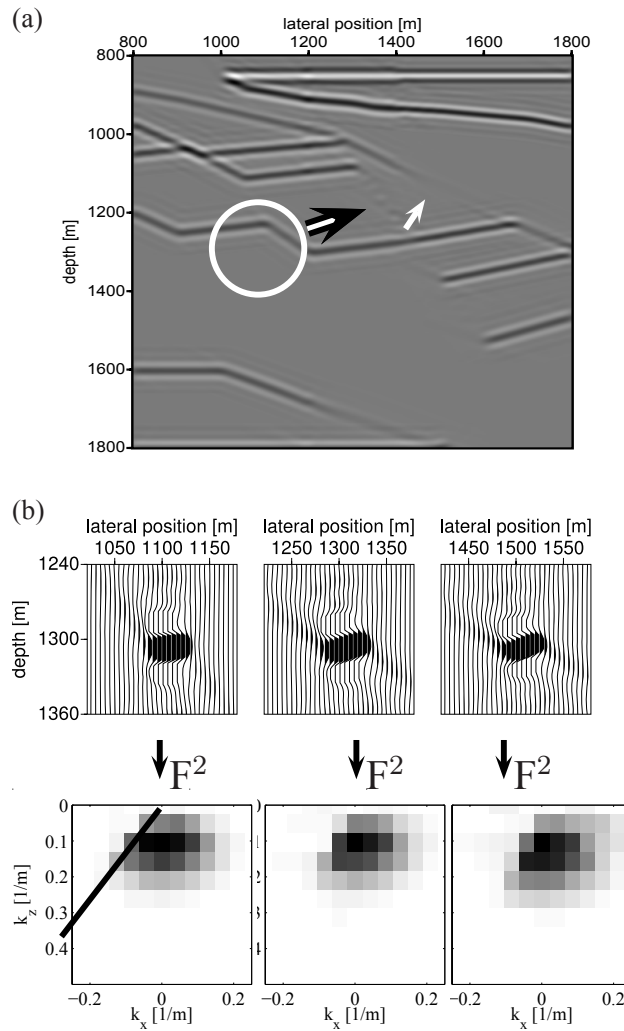
Figure 4.14: The following images correspond to the area indicated by the dashed box in Figure 4.11 (a). (a) Simulated prestack depth-migrated seismic images, using nine local 1D spatial resolution filters. (b) Three of the nine local 1D spatial resolution filters at a constant depth of 1300 m. The spatial resolution filters are shown in the space domain above and double-Fourier domain below. The white arrow, double arrow and circle indicate areas where the match between the reference and different simulated images is discussed. The black line discusses the accuracy (in terms of phase) between the local 1D and $x - \omega$ spatial resolution filters.

(a)

(b)
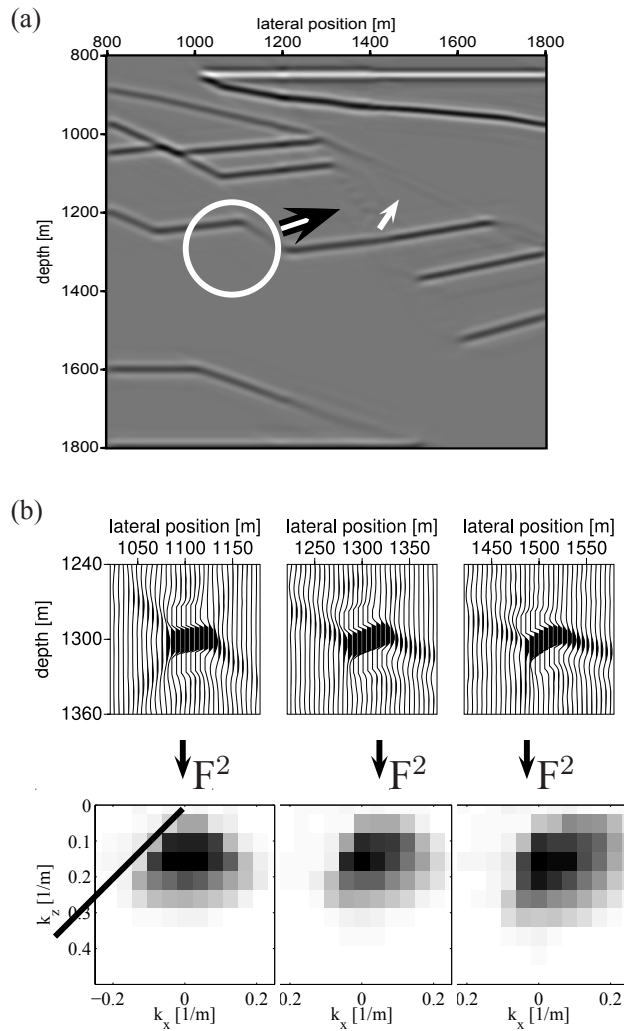
*Figure 4.15: The following images correspond to the area indicated by the dashed box in Figure 4.11 (a). (a) Simulated migrated seismic image of the graben model, using nine $x - \omega$ spatial resolution filters. (b) Three of the nine $x - \omega$ spatial resolution filters at a constant depth of 1300 m. The spatial resolution filters are shown in the space domain above and double-Fourier domain below. The white arrow, double arrow and circle indicate areas where the match between the reference and different simulated images is discussed. The black line discusses the accuracy (in terms of phase) between the local 1D and $x - \omega$ spatial resolution filters.*

dipping faults and boundaries of the seismic survey, the horizontal resolution increases (Figure 4.13 (c)). This means that geological features are horizontally more smeared, making them more difficult to interpret. It is noted that especially in survey design the horizontal resolution is studied through a so-called focal beam analysis [Berkhout et al., 2001; Volker et al., 2001; Vermeer, 2001].

■ **4.3.4   Simulating common-offset prestack depth-migrated seismic data**

An offset range between 250 and 350 m is selected from the acoustic finite difference modeled shot records and subsequently prestack depth-migrated, the resulting focused near-offset image is shown in Figure 4.16 (a).

A near-offset image is simulated by filtering the nine equally distributed areas of the normal-incidence reflectivity model with nine constant 300 m offset $x - \omega$ spatial resolution filters. After a summation of the individual spatial convolution results, this produces a simulated near-offset prestack depth-migrated image (Figure 4.17 (a)). Below this figure, three of the nine $x - \omega$ constant offset spatial resolution filters are shown in the spatial and in the double-Fourier domain. The near-offset spatial resolution filters are more blurred than the $x - \omega$ zero-offset spatial resolution filters, because less angle information is taken into account (Figures 4.15 (b) and 4.17 (b)).

The match between the reference and simulated near-offset images is very good. This is observed, in the three areas highlighted by the two different arrows and the circle, the simulated near-offset image has correctly suppressed the steep dipping faults and show a proper blurring. It is noted that by using a properly stretched wavelet in the 1D convolution model the near-offset blurring could have been simulated. However, not the specific suppressing of the geological boundaries in the near-offset case.

Offset information is quite important in fluid and rock classification [Yilmaz, 2001; Avseth et al., 2003]. In order to simulate amplitude information, the following two improvements are considered. Firstly, a proper reflectivity model is obtained by calculating the incidence angle associated to the offset. A quick approach would be to use Snell's law to find the incidence angle on a trace-by-trace basis, which is a common technique to transform an offset- to an angle-image. Secondly, care could be taken to correctly simulate the
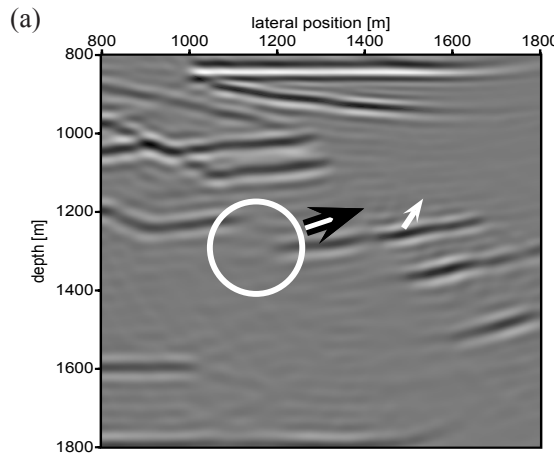
Figure 4.16: (a) A reference near-offset image of Figure 4.11 (a). The white arrow, double arrow and circle indicate areas where the match between the reference and different simulated images is discussed.

amplitude of the spatial resolution filter, e.g., following a method known as Simulating Migrated Amplitude (SMA) [Laurain et al., 2004].

■ 4.3.5 Simulating seismic uncertainties

In the previous discussion, ideally zero- and near-offset prestack depth-migrated images were simulated. The spatial resolution filter can also express the influence of, e.g., a "wrong" migration velocity model or be influenced by statics (see also the discussion in Section 3.2.1).

Simulating suboptimal focused prestack depth-migrated seismic data

In the previous examples one and the same velocity model was used for forward modeling and as input to migration. In order to test the application

(a)

(b)
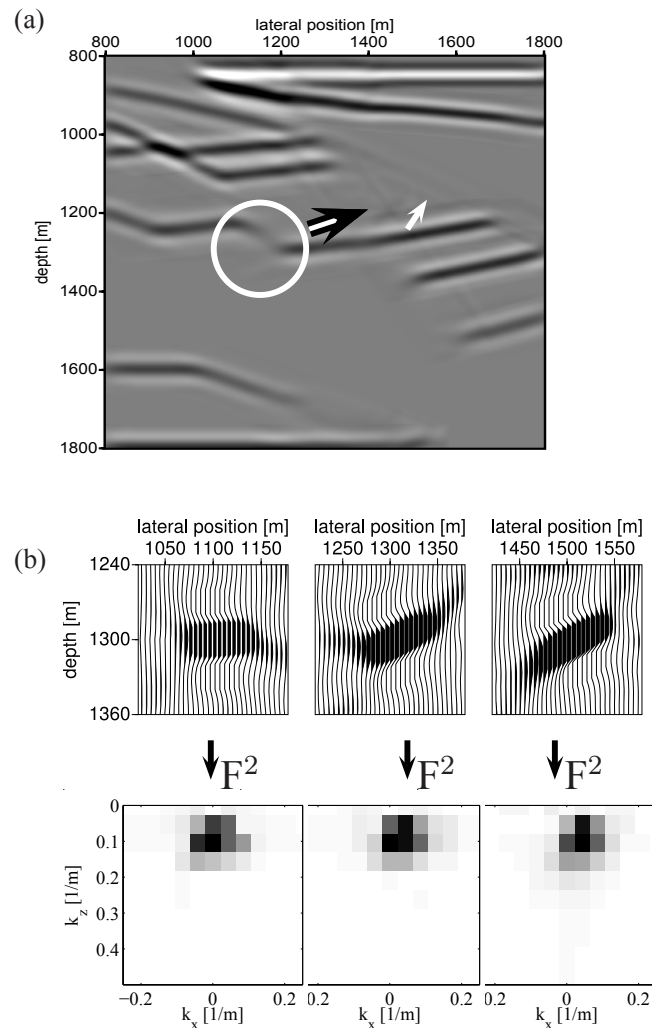
Figure 4.17: (a) Simulated near-offset image using nine offset $x - \omega$ spatial resolution filters. (b) Three of the nine $x - \omega$ offset spatial resolution filters at a constant depth of 1300 m. The spatial resolution filters are shown in the space domain above and double-Fourier domain below. The white arrow, double arrow and circle indicate areas where the match between the reference and simulated image is discussed.

of supporting migration velocity analysis, the velocity of two layers in the migration velocity model is lowered (indicated by $c_{p_{wrong}}$ in Figure 4.11 (a)). The acoustic finite difference measurements are prestack depth-migrated using the modified velocity model. The result is shown in Figure 4.18 (a), together with the previous reference migration result in Figure 4.19 (b). The wedge structure is gradually shifted upward going from $x=$ 1600 m to $x=$ 1000 m (indicated by the dashed horizontal line in Figures 4.18 (a) and (b)). Also the whole structure in the target is laterally shifted, which is highlighted by the white vertical line at lateral position 1000 m (Figures 4.18 (a) and (b)). In order to simulate these effects, nine $x - \omega$ spatial resolution filters at $x=$ 1100 m, $z=$ 1100 m to $x=$ 1500 m, $z=$ 1500 m are computed by performing forward modeling with the actual velocity model and shot-based migration with the modified velocity model. A rectangular grid overlying the spatial resolution filters, show that they are both vertically and horizontally wrongly positioned (Figure 4.19 (b)). Or in order words, they are out of focus. Each of the nine spatial resolution filters is convolved with an equal area of the normal-incidence reflectivity model. After summing the individual result, a suboptimal focused prestack depth-migrated image is simulated (Figure 4.19 (a)).

The result shows that the shifting of the wedge structure is simulated and also the target area is laterally mis-positioned (Figures 4.18 (b) and 4.19 (b)). The abrupt steps illustrate the local behavior of the spatial resolution filter. Making use of more spatial resolution filters will result in a smoother seismic image.

Simulating the influence of statics for interpreting time-lapse data

Interpreting time-lapse data is hampered by uncertainties in the detector positions between two different seismic surveys [Wever and Spetzler, 2004]. In order to show what effect this uncertainty has on a prestack depth-migrated image, the absolute detector uncertainty is translated into a static shift and a difference spatial resolution filter is computed.

At $x=$ 1300 m, $z=$ 1300 m a spatial resolution filter is computed, where the shot record was trace-by-trace randomly shifted by 0 or +/- 4 ms. The time shift simulates a certain detector mis-positioning between the two seismic surveys. Subtracted from the static free spatial resolution filter at the same
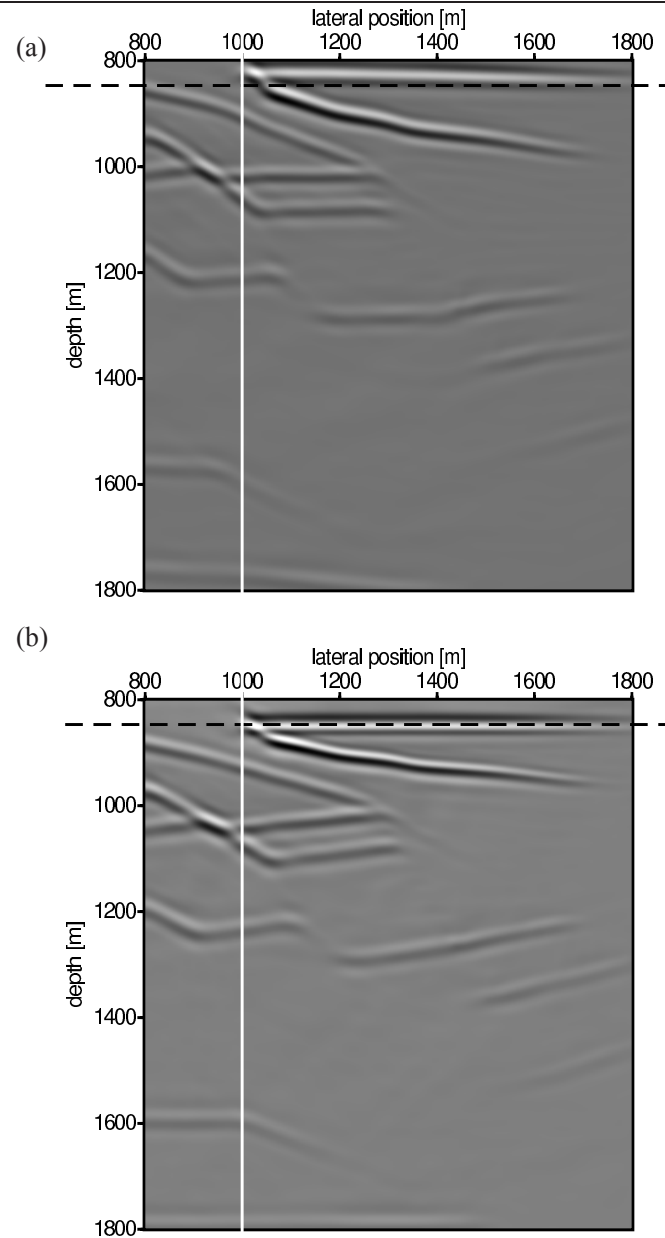
Figure 4.18: The following images correspond to the area indicated by the dashed box in Figure 4.11 (a). (a) A reference prestack depth-migrated image. Redisplaying Figure 4.11 (b). The dashed and white lines highlight the effect of a "wrong" migration velocity model.

(a)

(b)
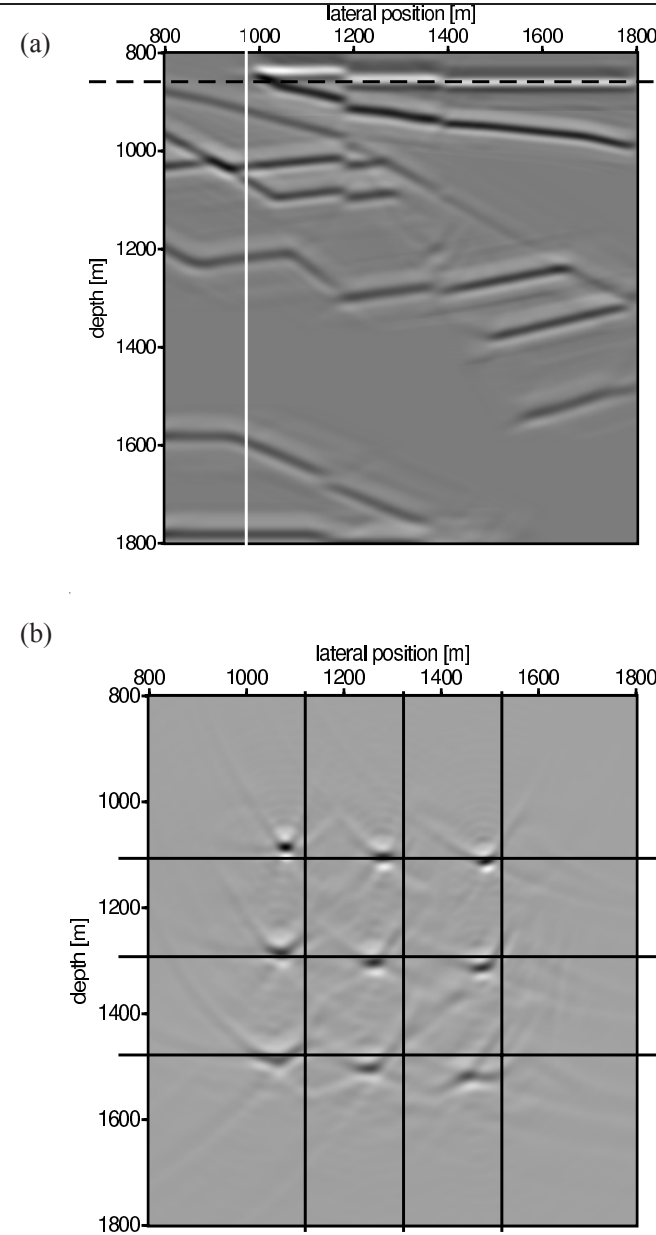
Figure 4.19: *The following images correspond to the area indicated by the dashed box in Figure 4.11 (a). (a) A simulated prestack depth-migrated image obtained by using the nine out of focus spatial resolution filters of figure (b). (b) Nine spatial resolution filters. The grid in overlay illustrates that all nine spatial resolution filters are out of focus. The dashed and white lines highlight the effect of a suboptimal focused image.*

position, a difference spatial resolution filter is obtained (Figure 4.20 (b)), which show Hagedoorn's isochrons (see also discussion in Section 3.1.1). This difference spatial resolution filter is then used in a multidimensional spatial convolution with the normal-incidence reflectivity model to simulate a difference prestack depth-migrated image (Figure 4.20 (a)). Coherent events, e.g. indicated by the arrow, appear in the target-zone. This could hint an interpreter that the coherent reflectors originate from detector mispositioning instead of a fluid replacement.

It is emphasized that this conclusion should be taken with great care, because statics can significantly vary laterally. Therefore, using only one difference spatial resolution filter, which is only locally valid, is an assumption that may easily break down.
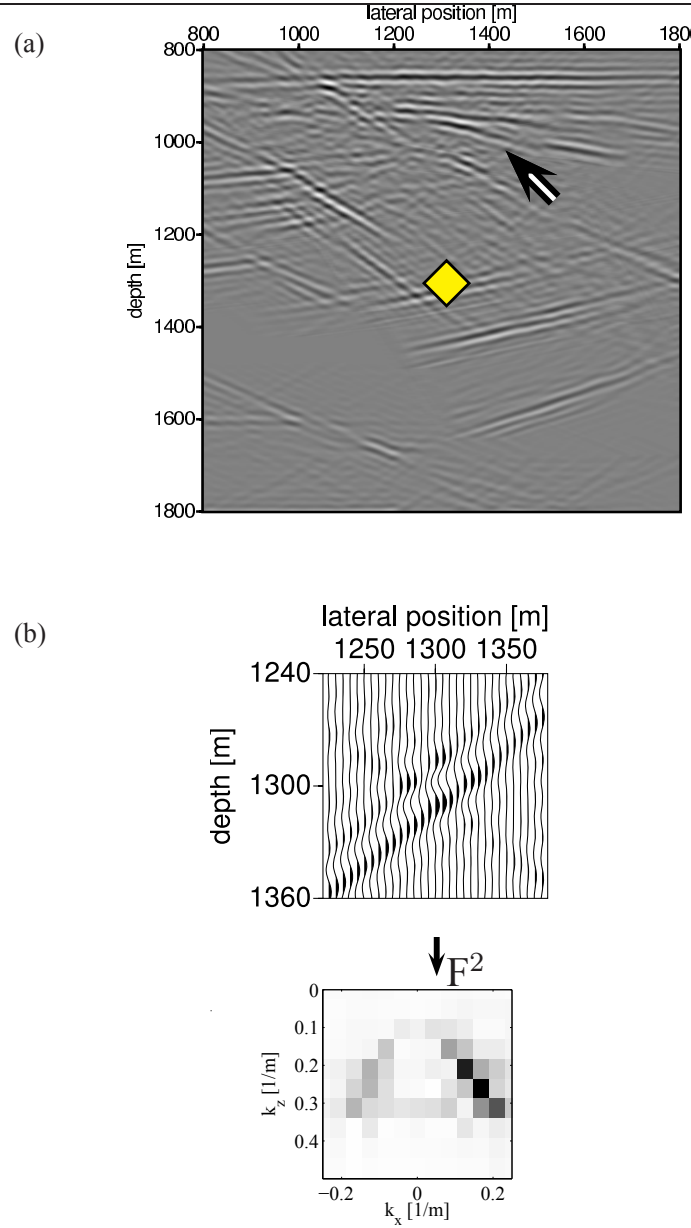
Figure 4.20: *The following image corresponds to the area indicated by the dashed box in Figure 4.11 (a). (a) A difference plot, showing the effects of detector mispositioning by using a difference spatial resolution filters. The location of the filter is highlighted by the diamond. (b) A difference spatial resolution filter. The spatial resolution filter is shown in the space domain above and double-Fourier domain below. The arrow highlights a coherent event.*

■ 4.3.6   Simulating constrained sparse-spike inverted data

The reference constrained sparse-spike impedance image of the prestack-depth migrated data (Figure 4.11 (b)) is obtained with a commercial software package. The impedance result is obtained with the following four steps. In step one, based on a well log at $x=$ 1150 m, an inversion wavelet is estimated. In step two, the constrained sparse-spike inversion algorithm is applied, followed in step three, by adding low-frequency information from only the well log to all traces. In the final fourth step, an impedance image is simulated after an integrating step and scaling each trace with a constant impedance value that is computed from the log data (Figure 4.21 (a)). It is noticed that the industry practice is to build a more detailed low-frequency model instead of using only the well log; this would probably have improved the impedance image.

Impedance data are simulated by performing a multidimensional spatial convolution between the approximated angle filter and the normal-incidence reflectivity model, followed by adding the low-frequency information that is used in the inversion process of the reference data and an integration and a scaling step (Figure 4.21 (b)). The approximated angle filters at $x=$ 1100 m, $z=$ 1100 m to $x=$ 1500 m, $z=$ 1500 m, are computed by performing a constrained sparse-spike inversion of the local 1D spatial resolution filters shown in Figure 4.14 (b). This step adds almost no additional computational costs to simulate inverted data. As an intermediate result the filtered normal-incidence reflectivity data show that the approximated angle filters (Figure 4.23 (b)) have suppressed specific geological reflectors but not blurred the other reflectors (Figure 4.23 (a)). The impedance model of Figure 4.11 (a) is shown in Figure 4.22 (a). Additionally, the low-frequency trend of the input impedance model is removed and replaced by the low-frequency information of only the well log at $x=$ 1150 m (Figure 4.22 (b)).

Two traces at 1150 m and 1500 m are selected from the reference, the simulated, the input impedance and the low-frequency filtered input impedance model. The comparison shows that the reference and simulated data show the same trend. This is not shown by the input impedance data (Figure 4.24). Around the location of the steeply dipping faults ($x=$ 1200 m to $x=$ 1800 m), two depth slices at 1050 m and 1200 m are shown in Figures 4.25 (a) and (b), respectively. The reference and simulated constrained sparse-spike inverted

data match each other nicely. However, they do not recover the trend of the input impedance, because the influences of the low-frequency model and the suppression of specific dipping reflectors need to be restored. Finally, the low-frequency filtered input impedance result shows that only taking into account the low-frequency model is not sufficient, also it should include the effect of the limited recording aperture and propagation effects of the over-burden, because the seismic inversion process does not account for this.

(a)

(b)
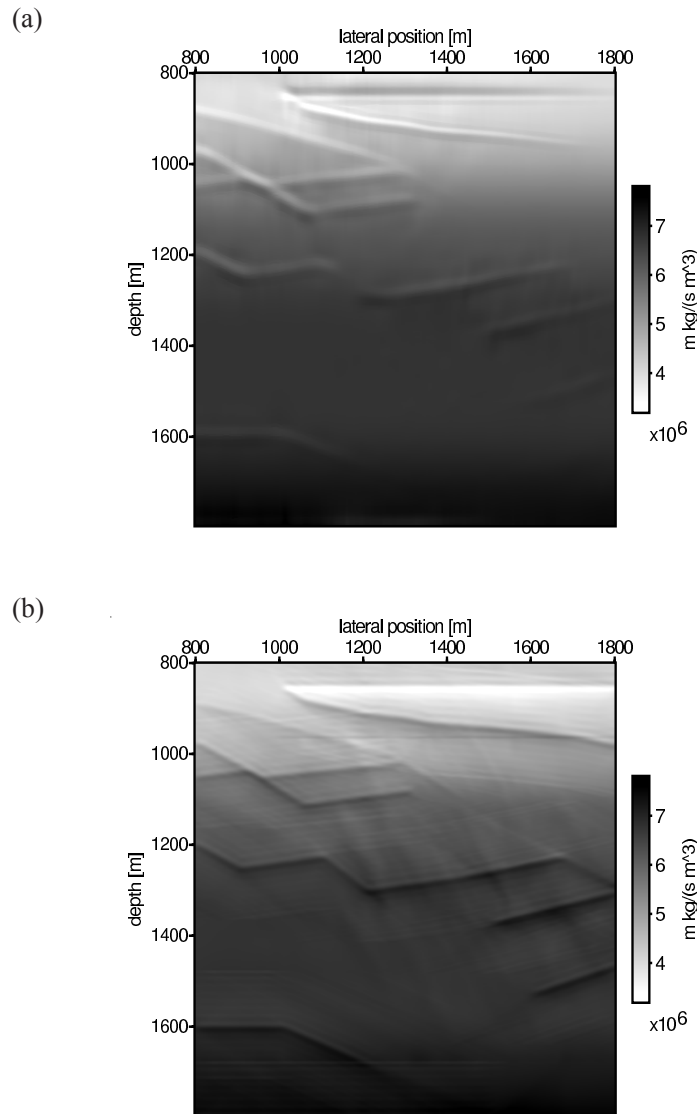
Figure 4.21: *The following images correspond to the area indicated by the dashed box in Figure 4.11 (a). (a) A constrained sparse-spike impedance result of Figure 4.11 (b). (b) A simulated constrained sparse-spike impedance result.*

(a)

(b)
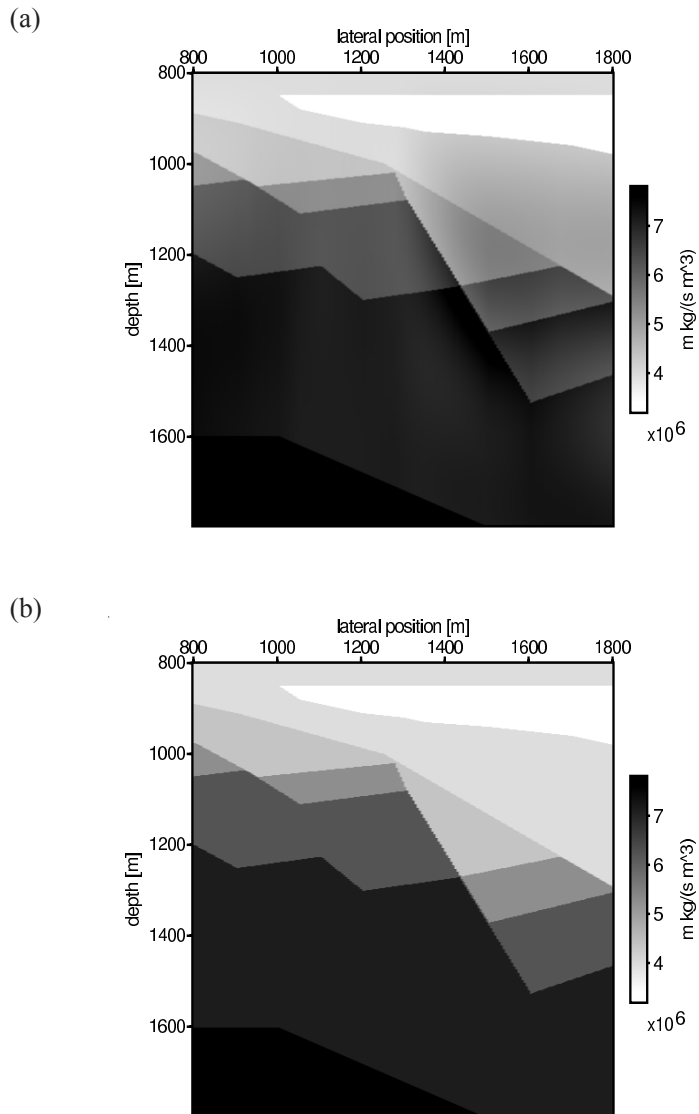
Figure 4.22: *The following images correspond to the area indicated by the dashed box in Figure 4.11 (a). (a) The impedance model of Figure 4.11 (a). (b) Low-frequency filtered version of figure (a).*

(a)

(b)
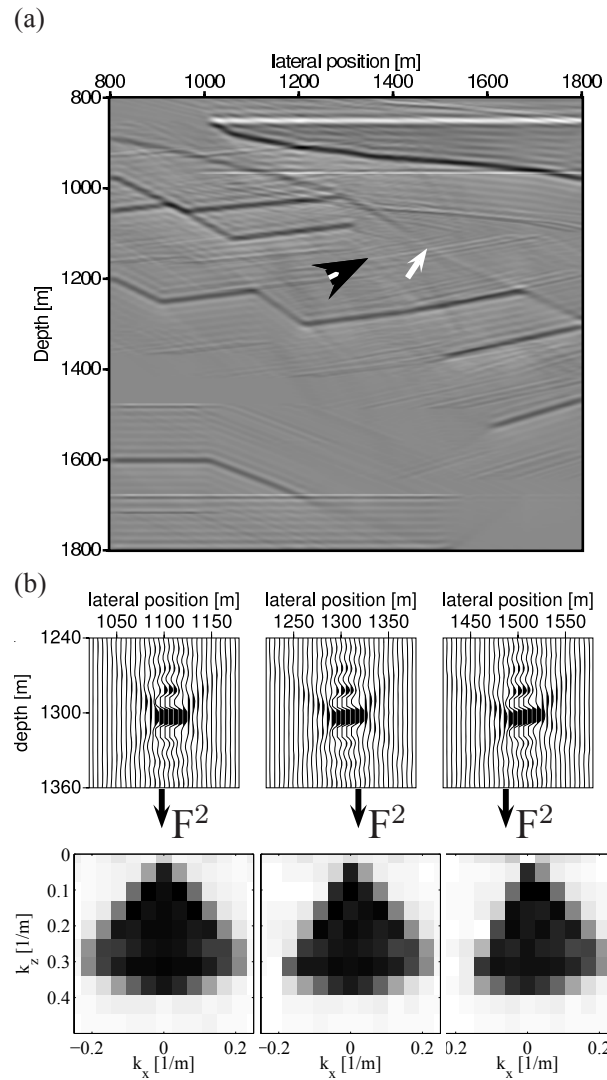
Figure 4.23: The following image corresponds to the area indicated by the dashed box in Figure 4.11 (a). (a) A local 1D angle filtered normal-incidence reflectivity image. (b) Three of the nine approximated angle filters at a constant depth of z= 1300 m. The spatial resolution filters are shown in the space domain above and double-Fourier domain below. The arrows highlight suppressed steeply dipping faults. It is noticed that the reflectors by filtered by a band-limited filter that has a constant spectrum. Therefore, the image is blurred.
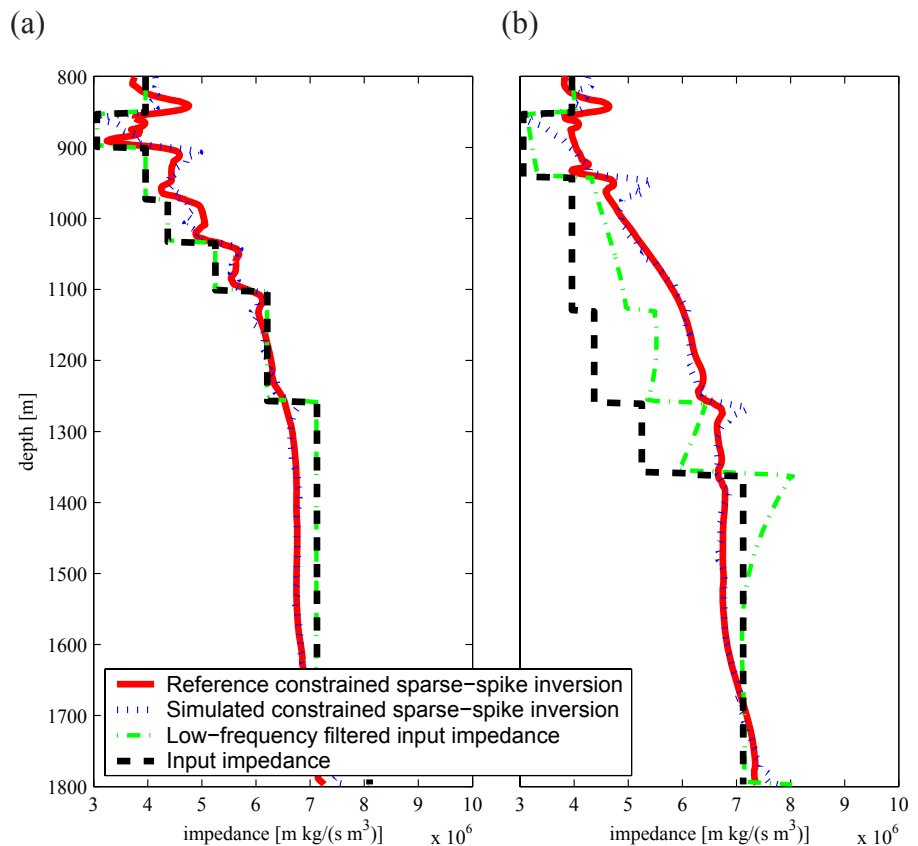
Figure 4.24: *(a) A trace comparison at lateral position 1150 m of Figures 4.21 (a) and (b), 4.22 (a) and (b). A trace comparison at lateral position 1500 m of Figures 4.21 (a) and (b), 4.22 (a) and (b).*

(a)

(b)
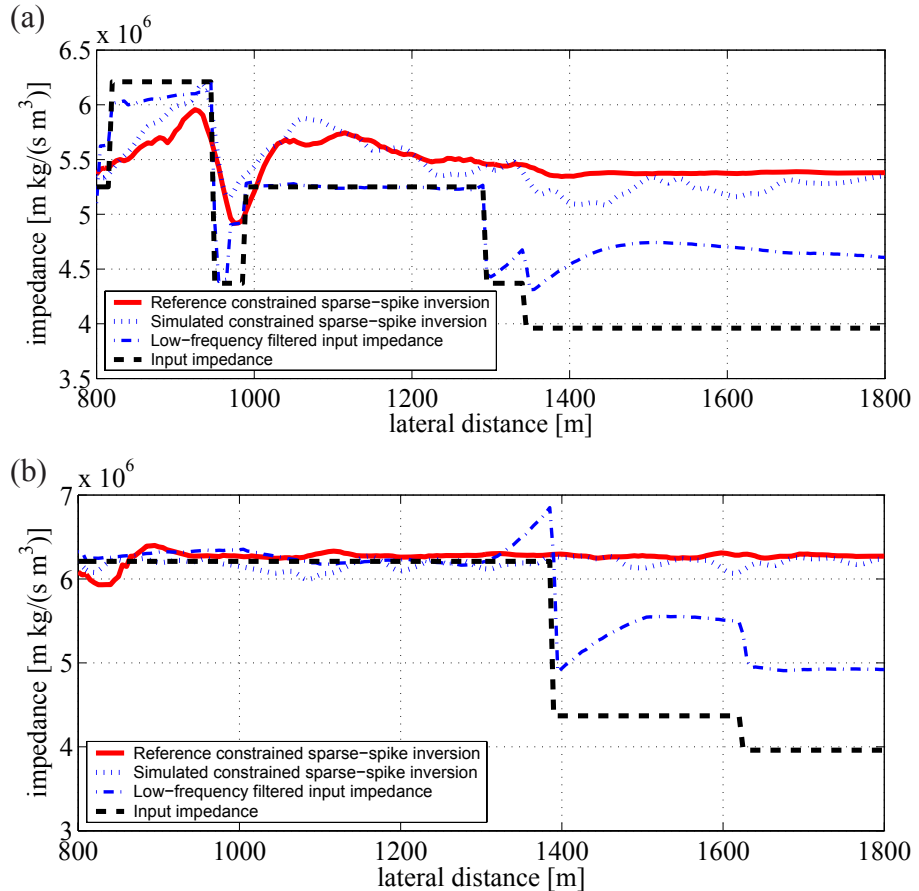
Figure 4.25: (a) A depth slice comparison at a depth of z= 1050 m of Figures 4.21 (a) and (b) and 4.22 (a) and (b). (b) A depth slice comparison at a depth of 1200 m of Figures 4.21 (a) and (b) and 4.22 (a) and (b).

4.4   A complex overburden model: Sigsbee model

The Sigsbee 2A data-set (courtesy SMAART consortium, Paffenholz et al. [2002]) models the geologic setting found on the Sigsbee escarpment in the deepwater Gulf of Mexico. The complex overburden makes imaging and consequently geological interpretation of the target-zone under the massive salt body (highest velocity) a real challenge. The target-zone is illustrated by the dashed box in Figure 4.26 (a).

The survey parameters to probe the Sigsbee model are summarized as follows [SMAART, 2002], shot records are modeled using an acoustic finite difference forward modeling algorithm with as source a Ricker wavelet with a peak frequency at 25 Hz. The survey starts at the far left side of the model and the source pulls a cable of 7800 m. The shot interval is 45 m, detector interval is 22.5 m and sample rate is 8 ms. No seismic pre-processing steps are done before a prestack depth-migration algorithm is applied, more details on the algorithm are found in Thorbecke et al. [2004]. The migration-velocity model is a gradient-velocity model discretized at dz = 7.5 m and dx = 22.5 m, which includes the correct shape and velocity value of the salt body. The migration parameters are the following; the maximum frequency is set to 52 Hz and the maximum illumination angle is set to $75°$. Using Automatic Gain Control (AGC), a zoomed-in prestack depth-migrated image is shown in Figure 4.27 (b), which is used as reference to test how accurately (in terms of the phase) prestack depth-migrated and constrained sparse-spike inverted data are simulated.

■ 4.4.1   Simulated zero-offset prestack depth-migrated seismic data

The reference migrated data-set is obtained from a stack of prestack depth-migrated common-offsets. This approach could also exactly be simulated using the presented framework. However, this is having large computational costs. Therefore, as an initial approach it is assumed that the reference data resemble a zero-offset prestack depth-migrated image.

The spatial resolution filter is a local filter, to further lower the computational costs it is assumed to be locally lateral invariant for a small depth range. However, in a shared-earth model this interval has to be chosen with
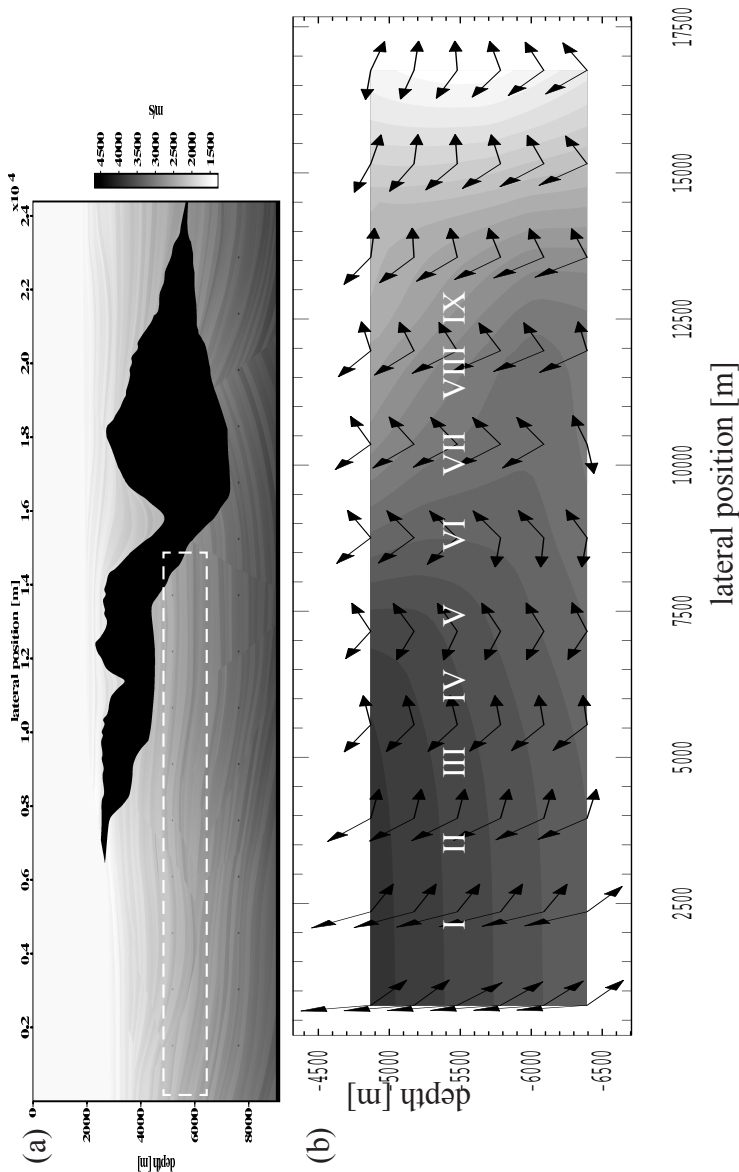
Figure 4.26: (a) earth model of the Sigsbee escarpment. The rectangular box indicates the target area for geological interpretation. (b) Distribution of the maximum angles of wave propagation superimposed on the smoothed velocity model. The lateral position of nine the spatial resolution filters at a depth of 5500 m are indicated by the numbers I to IX.

great care. At a depth of 5500 m (center of the target-zone), nine spatial resolution filters are computed from lateral position 1500 m to 13500 m. The depth and lateral spacing of 1500 m are given by two arguments. Firstly, the ray-trace results show the angle variation changes little in both depth and lateral variation every 1500 m (Figure 4.26 (b)). Angle information that is obtained from, e.g., a Kirchhoff based migration-algorithm can be used as a-priori information to properly choose the positions of the spatial resolution filters. Secondly, the lateral spacing resembles a typical well-spacing and thus the spatial resolution filter would be calibrated with the seismic data at this positions using a well-to-seismic tie (see also a real data example in Section 5.4).

The nine spatial resolution filters are computed in two different ways, the first set uses the angle and band-limitation filter with a local 1D assumption and the second set uses $x - \omega$ forward and prestack depth-migration.

The local 1D spatial resolution filters are obtained by constructing an angle filter with the aid of the ray-trace information. The computed maximum angles of wave propagation that are over 90°, indicate so-called turning waves (Figure 4.26 (b)). However, in the construction of the angle filters the maximum angles of wave propagation values are set to a maximum of 75°. This is done to resemble the processing flow as close as possible. Because, the $x - \omega$ migration algorithm that is used to migrate the reference data does not handle this wave type (see also discussion in Section 3.3) and the maximum angle of illumination is set to 75°. The band-limitation filter is constructed with the aid of a time-to-depth converted Ricker wavelet. This wavelet has a peak frequency at 25 Hz. The simulated zero-offset local 1D prestack depth-migrated image, together with five of the nine local 1D spatial resolution filters are shown in Figure 4.28.

The $x - \omega$ spatial resolution filters are computed performing forward and prestack depth-migration using one-way $x - \omega$ operators [Thorbecke et al., 2004] in the migration velocity model. The simulated zero-offset $x - \omega$ prestack depth-migrated image, together with five of the nine $x - \omega$ spatial resolution filters are shown in Figure 4.29.

The 1D convolution model uses one time-to-depth converted Ricker wavelet at lateral position $x=$ 1500 m, to create the 1D seismic image of Figure 4.30.

Discussion on the simulated zero-offset prestack depth-migrated data

Before the simulated results are discussed, three areas of interest are selected in the reference prestack depth-migrated image by comparing it to the normal-incidence reflectivity model (shown in Figures 4.27 (b) and (a), respectively).

Zone A: adjacent to the salt flank a shadow zone is observed in the reference data, highlighted by the white colored arrow. This portion of the subsurface is unobservable because their ray-paths did not reach the subsurface [Sheriff, 2001]. This is most likely caused by the complex salt structure.

Zone B: left from the shadow zone steeply dipping events are observed in the correctly imaged layers (highlighted by black colored arrows). From the reflectivity model it is concluded that these are artifacts, probably originating from (randomly) imaged internal multiple energy from the steep salt flank.

Zone C: the steep flanks of the sedimentary structure (around lateral position 6000 to 8000 m) are imaged in great detail, although a dimmed zone can be identified (highlighted by the white colored circles).

The three simulated seismic results show the following features in the three zones.

Zone A: the local 1D image (Figure 4.28 (a)) and the 1D seismic image (Figure 4.30 (a)) both do not show the shadow zone. In the $x - \omega$ image it is present, but the lateral position is not correct, which is illustrated by the vertical solid line. This is explained as follows: the 1D convolution model will only vertically blur reflectors, it cannot suppress reflectors. The local 1D spatial resolution filter includes the effects of limited acquisition geometry, limited source bandwidth, discrete sampling [Chen and Schuster, 1999] and propagation effects in the overburden and therefore will suppress certain reflectors. However, it assumes that all angles are equally distributed between the maximum angles of wave propagation. Unfortunately, here this assumption breaks down, as the double arrow in the double-Fourier domain of the IX $x - \omega$ spatial resolution filter (Figure 4.28 (b)) shows, around k_x=0 there is a gap in the spectrum. The IX local 1D spatial resolution filter (Figure 4.29 (b)) has a continuous spectrum, as a result the horizontal reflectors adjacent to the salt flak are not suppressed in the local 1D image. The $x - \omega$ image shows a shadow zone that does not match the shape of the

reference image. This is caused by the assumption that one spatial resolution filter can be assumed constant in a rectangular shaped area of the reflectivity model, this breaks down for the complex geological model. Using more laterally and depth positioned spatial resolution filters in smaller rectangular areas will solve this problem. It is noted that interpolating spatially or in the double-Fourier domain is not a proper way to compute a new spatial resolution filter.

Zone B: the observed artifacts cannot be simulated because in the theoretical framework of Chapter 2 it is assumed that all multiple energy is properly removed.

Zone C:, the cause of the dimmed zones (two white colored circles) is subject for discussion. If it is not created by plotting the migrated data using AGC, angular amplitude variations may explain it. A second assumption of the local 1D spatial resolution filter is that all angles are present at equal strength, the $x - \omega$ spatial resolution filters in the Fourier domain show that in this earth model the wavelet varies in strength, which may simulate the dimmed zone.

The computational times are respectively, one week, minutes, hours and seconds for creating Figures 4.27 (b), 4.28 (a) 4.29 (a) and 4.30 (a), respectively. Finally, Figures 4.31 (a) and (b) show a comparison of the images at depths 5150 m and 5445 m and between lateral position 2500 m to 8000 m, respectively. A horizontal depth slice is chosen, because the 1D convolution model does not simulate horizontal smearing. This is observed in both depth slices by viewing the structures between lateral position 4000 m to 5000 m. The reference data shows that the structure is smoothly represented compared to the very blocky 1D convolution model result, which equals the input reflectivity model. Both the local 1D and $x - \omega$ simulated data show a more smooth representation of the structure, which resembles better the reference data.

■ 4.4.2   Simulating common-offset prestack depth-migrated seismic data

The previous example has illustrated that despite the zero-offset assumption the simulated data will provide a seismic interpreter with a tool to test how different geological scenarios will match the reference offset data.
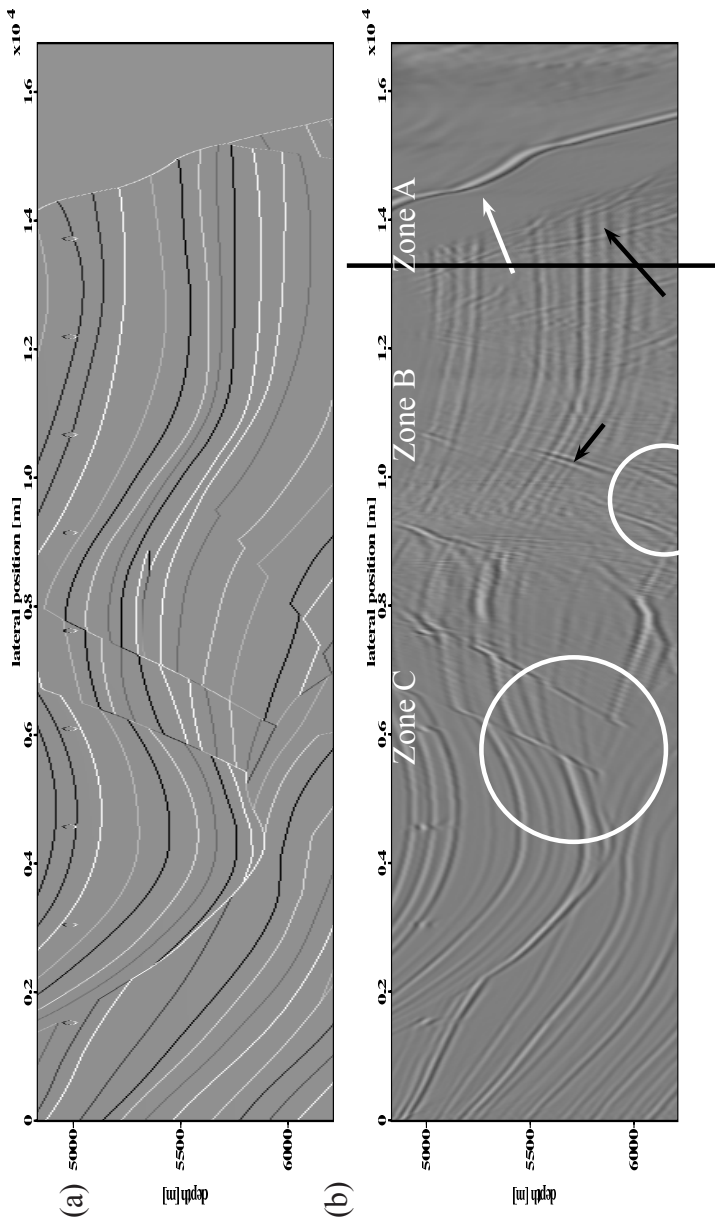
Figure 4.27: (a) The normal-incidence reflectivity model of the target area. (b) The resulting reference prestack depth-migrated image is plotted using AGC. The white arrow, black arrow, circles and line indicate areas where the match between the reference and simulated images is discussed.
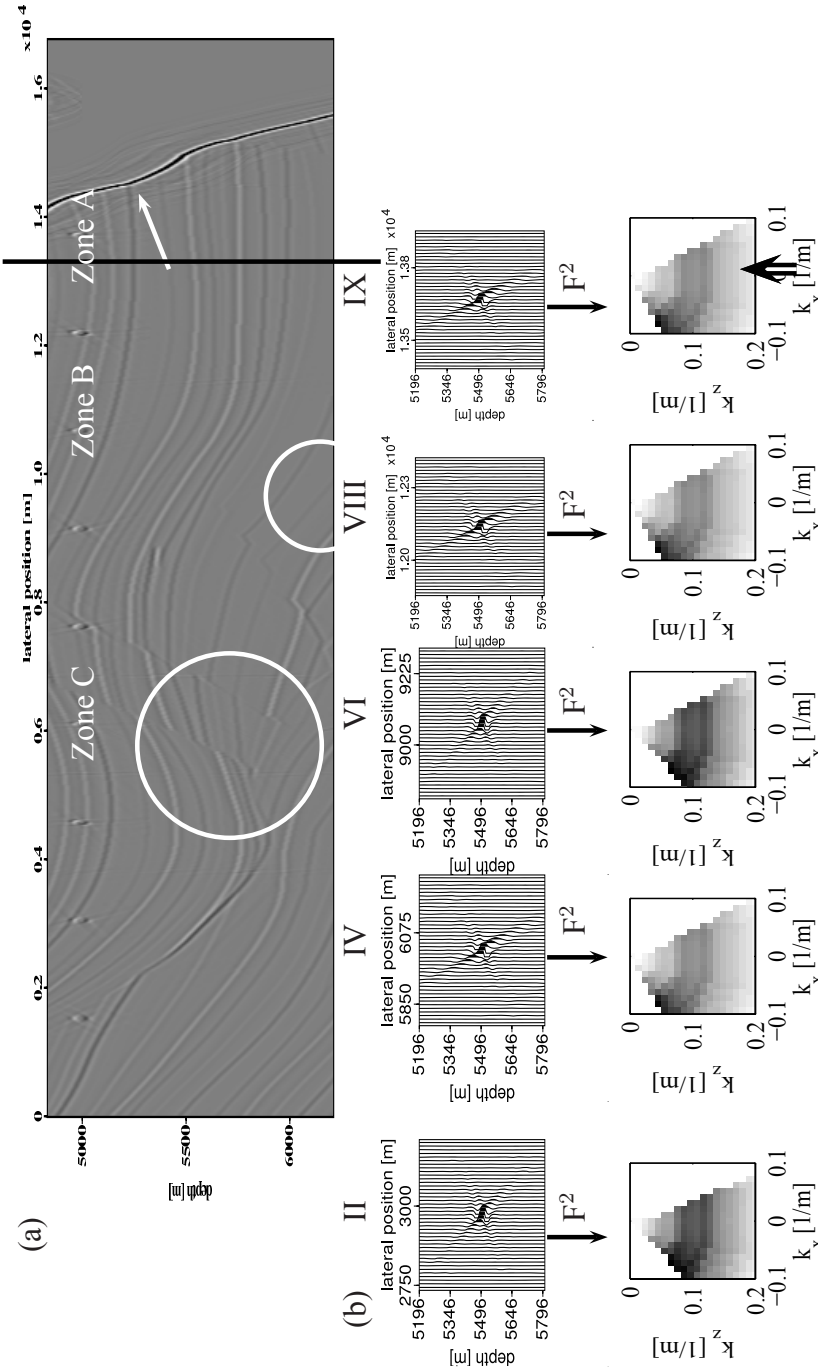
Figure 4.28: *(a) Simulated local 1D prestack depth-migrated seismic image. (b) Five of the nine local 1D spatial resolution filters, which are used to simulate figure (a). The spatial resolution filters are shown in the space domain above and double-Fourier domain below. The white arrow, double arrow, circles and line indicate areas where the match between the reference and simulated images is discussed.*
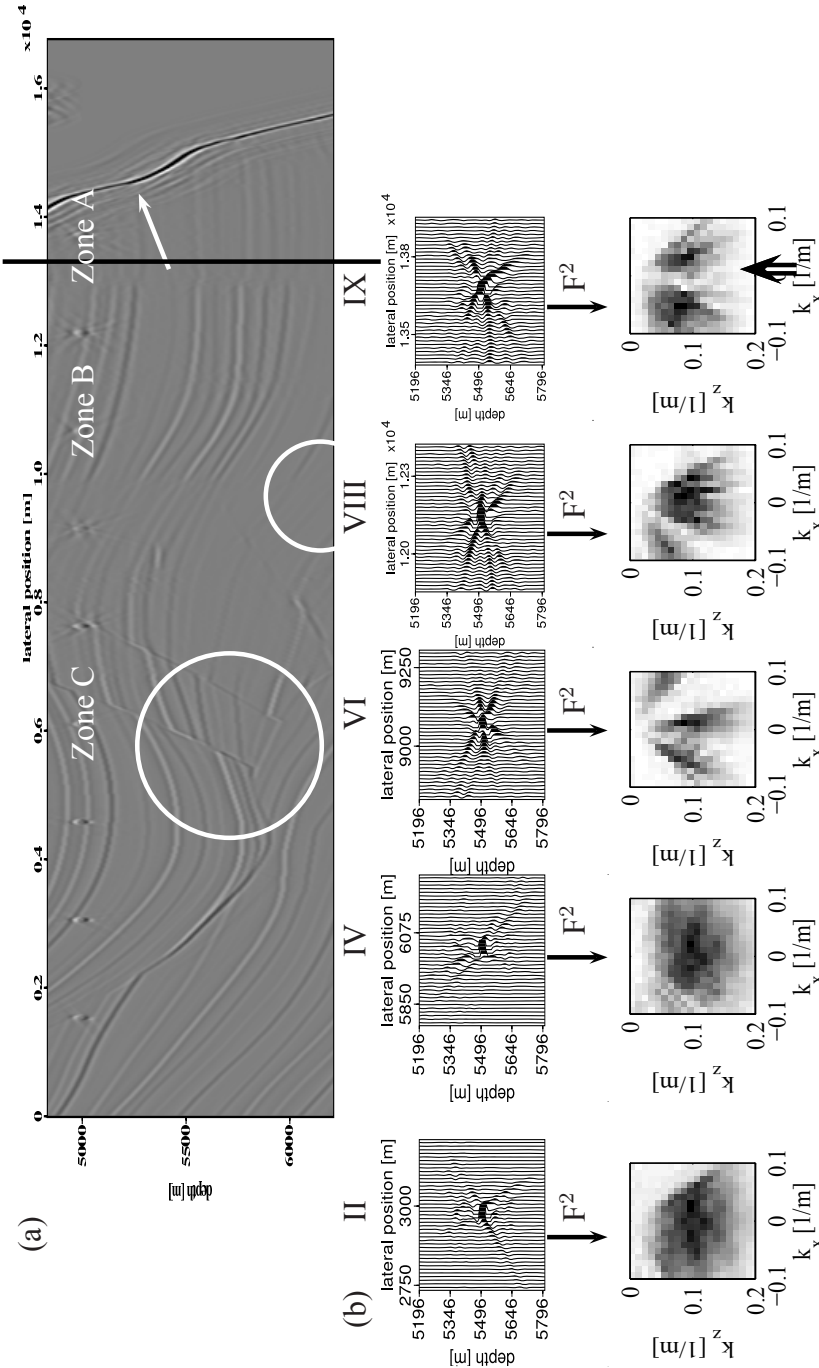
Figure 4.29: (a) Simulated $x - \omega$ prestack depth-migrated seismic image. (b) Five of the nine $x - \omega$ spatial resolution filters used to simulate figure (a). The spatial resolution filters are shown in the space domain above and double-Fourier domain below. The white arrow, double arrow, circles and line indicate areas where the match between the reference and simulated images is discussed.
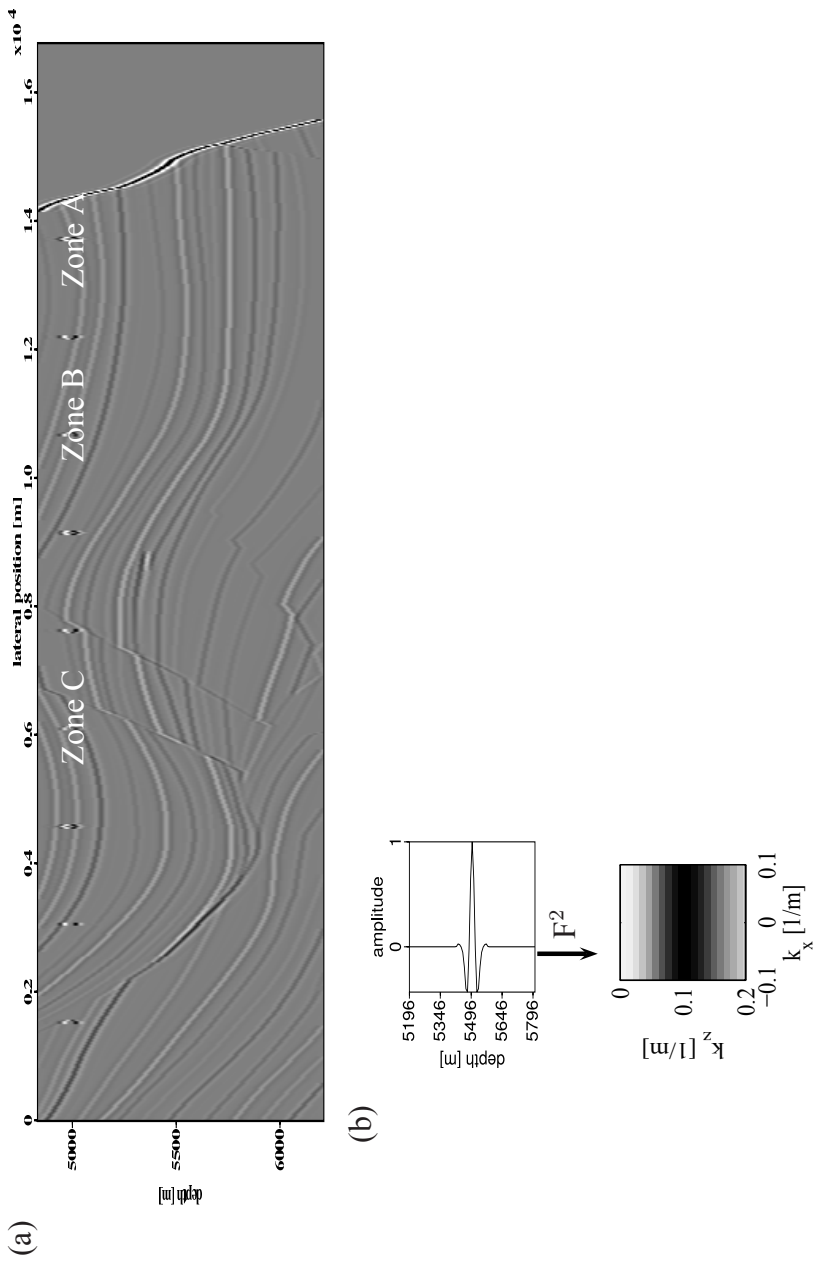
Figure 4.30: (a) Simulated 1D convolution model result. (b) Ricker wavelet used to simulate figure (a). The wavelet is shown in the space domain above and double-Fourier domain below.
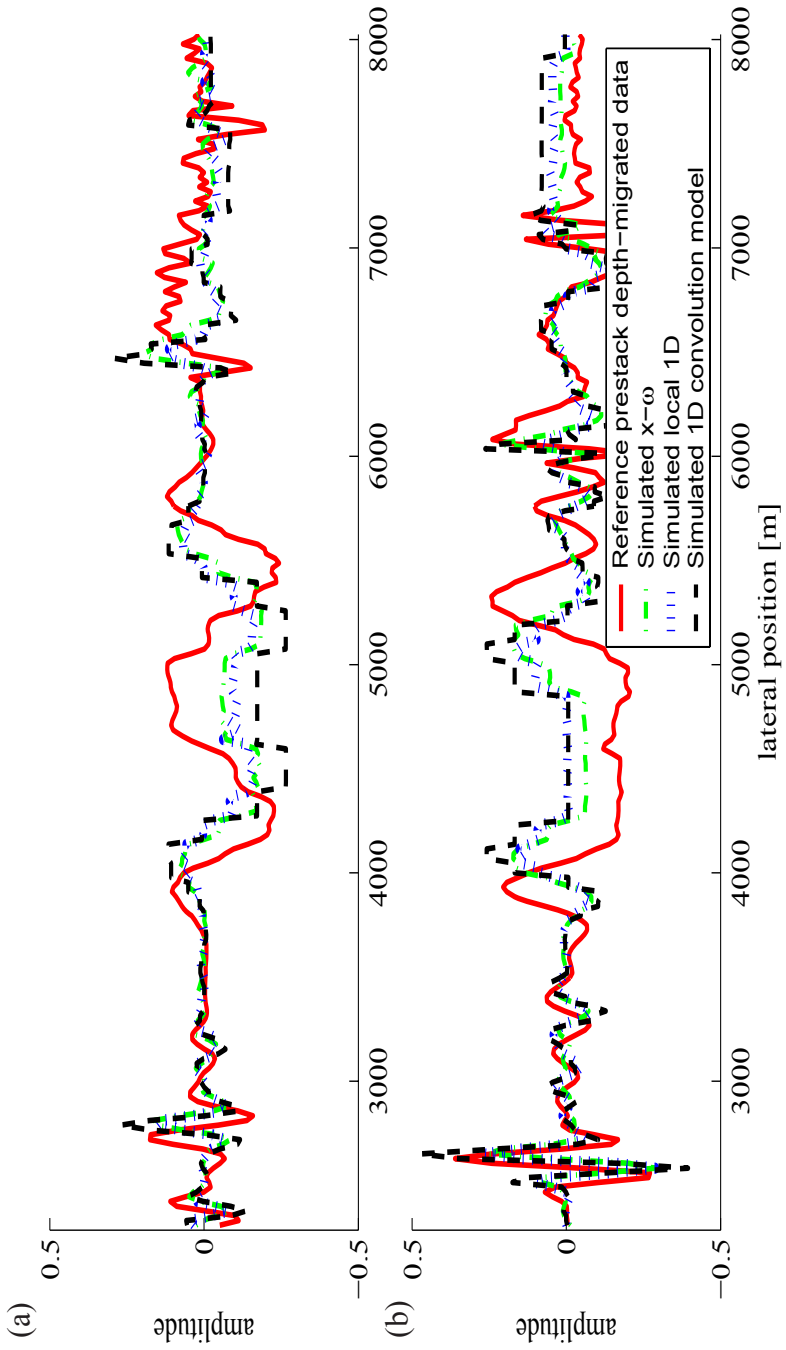
Figure 4.31: (a) Depth slice at position 5150 m, (b) depth slice at position 5445 m of Figures 4.27 (b), and 4.28 4.29 (a) and 4.30 (a). It is noticed that the 1D convolution model result resembles the amplitudes of the normal-incidence reflectivity model.

A reference far-offset prestack depth-migrated image is obtained from pre-stack depth-migrating an offset range between 3000 and 4000 m (Figure 4.32 (a)). If the seismic interpreter again would use the simulated zero-offset image to verify different geological scenarios, the simulated image does not properly simulate the reference far-offset image, which is more blurred and has imaged less structural information.

As a first step to better simulate the reference far-offset image, the zero-offset spatial resolution filters are replaced by nine far-offset $x - \omega$ spatial resolution filters derived from 3500 m offset data (Figure 4.32 (c)). After a summation of the individual spatial convolution results, a far-offset prestack depth-migrated image is simulated (Figure 4.32 (b)).

Discussion on the simulated common-offset depth-prestack migrated results

By comparison of the far-offset reference and simulated image, the following four areas of interest are selected.

Zone A: the reference and simulated far-offset images both show a shadow zone at almost the same lateral position.

Zone B: the black colored arrows probably indicate multiple energy, which is randomly imaged in the reference far-offset image. It is tacitly assumed that all multiple scattering has been properly removed from the real data or imaged to its correct position of origin. Because, multiple scattering is imaged differently on stacked offset images (e.g., compare the black colored arrows of Figures 4.27 (b) and 4.32 (a) and for more information we refer to [Yilmaz, 2001]), simulating different offset images may provide the seismic interpreter with a tool to understand the effect of multiple scattering.

Zone C: here a dimmed zone is found in the reference image as well in the simulated far-offset image.

Additionally to the zero-offset case, the following two observations are made. Firstly, in general the reference far-offset image is more blurred than the simulated zero-offset image, which is caused by the fact that less angle information is taken into account. This effect is also simulated in the far-offset image.

Zone D: shows that the structures on the left-hand side are not imaged, this is caused by the specific acquisition setup of the reference far-offset data.

The acquisition of the simulated far-offset image resembles the reference acquisition setup, thus also simulating that the structures are not imaged.

■ 4.4.3 Simulating constrained sparse-spike inverted data

The reference migrated data are constrained sparse-spike inverted using a commercial software package. Information to estimate an inversion wavelet is provided by a well log at lateral position 3429 m. The low-frequency model is a horizontally layered model based on the well log, which is added to the reflectivity data before the integration and scaling steps. The reference constrained sparse-spike inverted impedance image is shown in Figure 4.33 (a). The lack of structural information in the low-frequency model has created a low-impedance zone over the complete impedance result, adding more information to the low-frequency model will remove this zone. However, this model should than also be used in the simulation of the impedance data. In order to simulate the reference image, the spatial resolution filters which were previously used to simulate prestack depth-migrated data, are constrained sparse-spike inverted to obtained a set of nine local 1D and a set of nine $x - \omega$ approximated angle filters, respectively. These approximated angle filters are used in a multidimensional spatial convolution with the normal-incidence reflectivity data, next the low-frequency model of the reference data are added to the filtered data and after an integration and a scaling step, Figures 4.34 (a) and 4.35 (a) show the local 1D and $x - \omega$ impedance image, respectively.

Discussion on the simulated constrained sparse-spike inverted results

The reference impedance image is compared with the impedance model of the target-zone (Figures 4.33 (a) and (b)). This reveals that most of the geological structures are well resolved in the reference data, although at the far-right side which is under the salt, it is difficult to interpret the result. The previous discussed randomly imaged multiple scattering has also created artifacts in the reference impedance image (indicated by the black colored arrow). This cannot be simulated by the new framework.

The two simulated images show that the low-impedance zone, resulting from the low-detailed low-frequency model, is simulated. In order to investigate
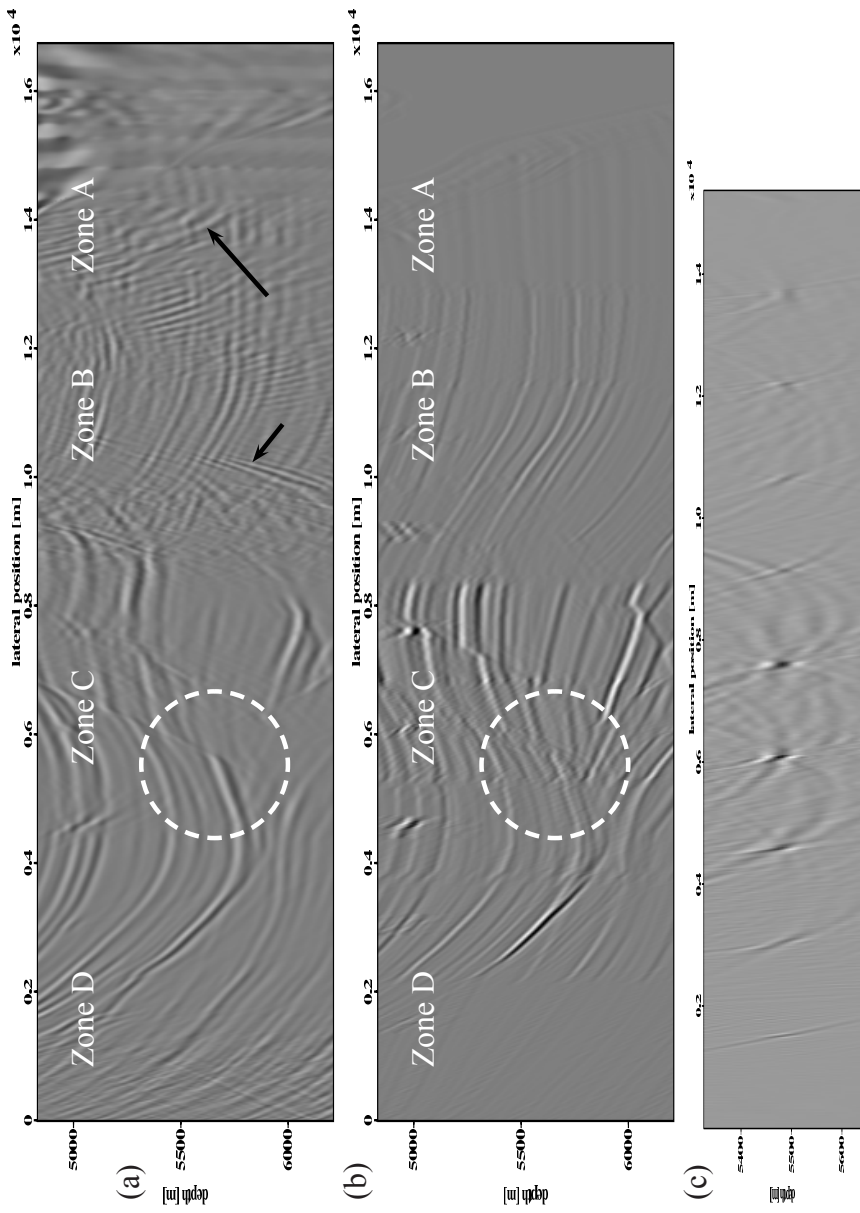
Figure 4.32: (a) A reference far-offset prestack depth-migrated image that is plotted using AGC. (b) A simulated far-offset prestack depth-migrated image. (c) A panel of far-offset spatial resolution filters that are used to simulate figure (b). The black arrows, dashed circle indicate areas where the match between the reference and simulated images is discussed.

the match between the images in more detail, different traces at lateral positions 3429, 6858, 10287 and 13716 m are compared. At the well log position (3429 m), all simulated impedance results match nicely the reference data (Figure 4.36). However, more below the salt the reference data deviate from the impedance model, this trend is also shown by the simulated data.

In order to investigate the effect of horizontal smearing, which is not properly removed by a constrained sparse-spike inversion algorithm, two depth slices at 5150 m and 5445 m between lateral position 2500 to 8000 m are selected from the different data (Figures 4.37 (a) and (b), respectively). The comparison shows that the reference image shows a much smoother representation of the input impedance model.
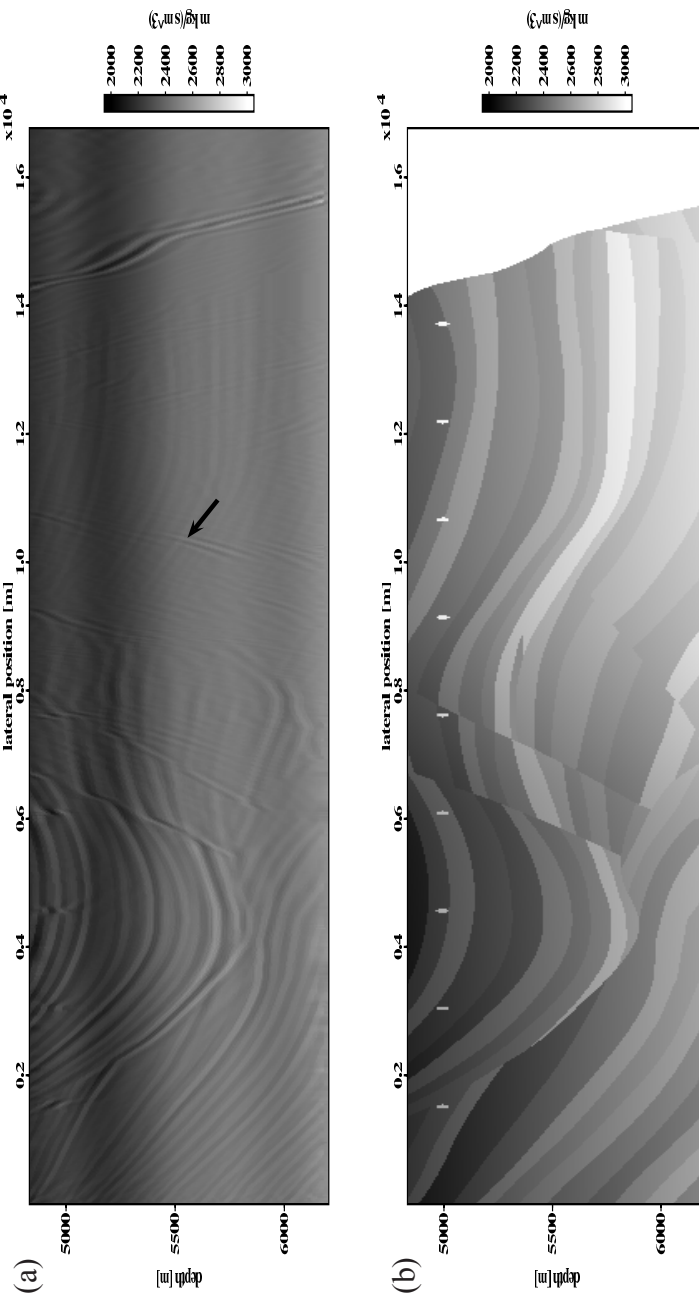
Figure 4.33: (a) Constrained sparse-spike inverted result of Figure 4.27 (b). (b) The impedance image of the target-zone. The black arrow highlight a random images multiple.
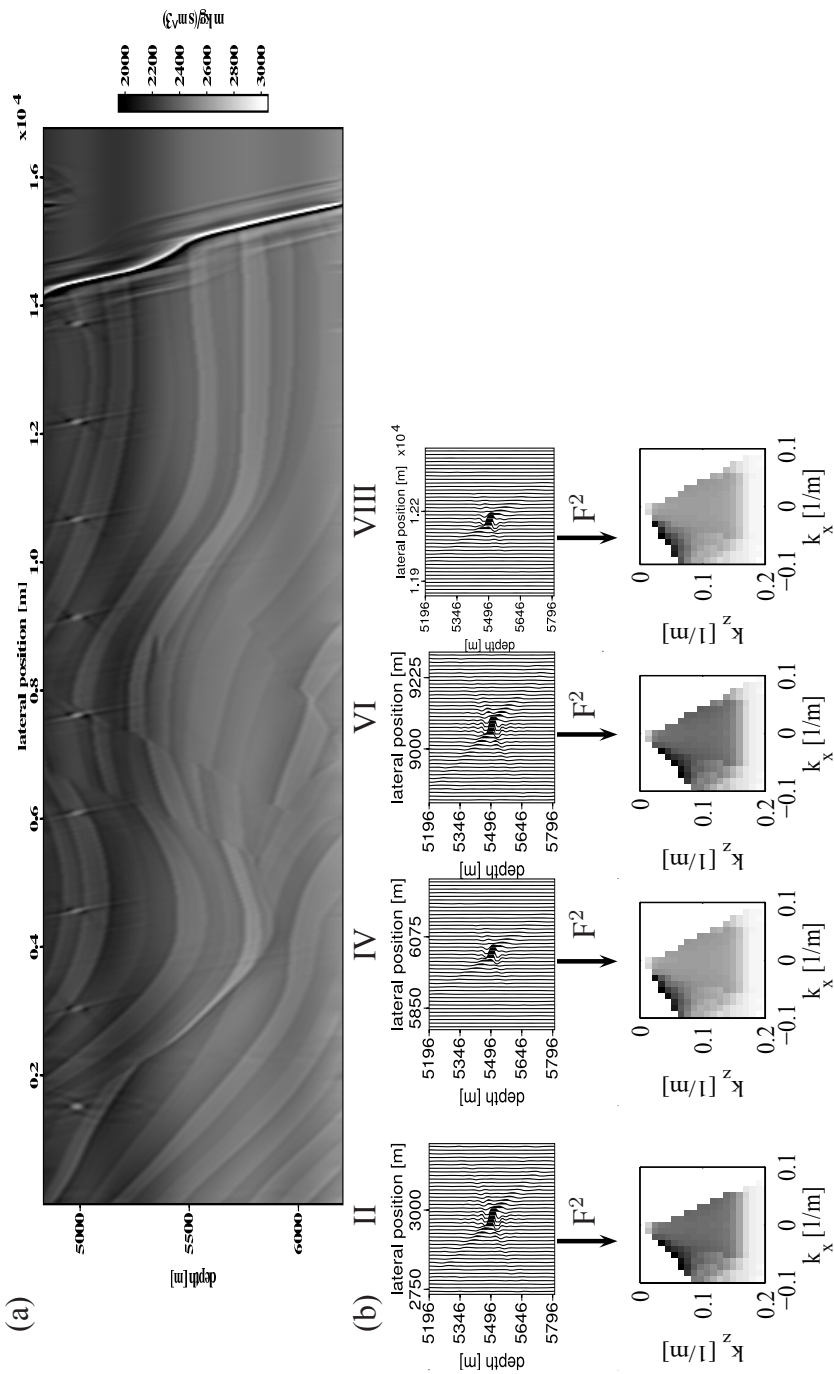
Figure 4.34: (a) Simulated constrained sparse-spike inverted data using nine approximated local 1D angle filter. (b) Four of the nine approximated local 1D angle filter that are used to simulate figure (a). The approximated local 1D angle filters are shown in the space domain above and double-Fourier domain below.
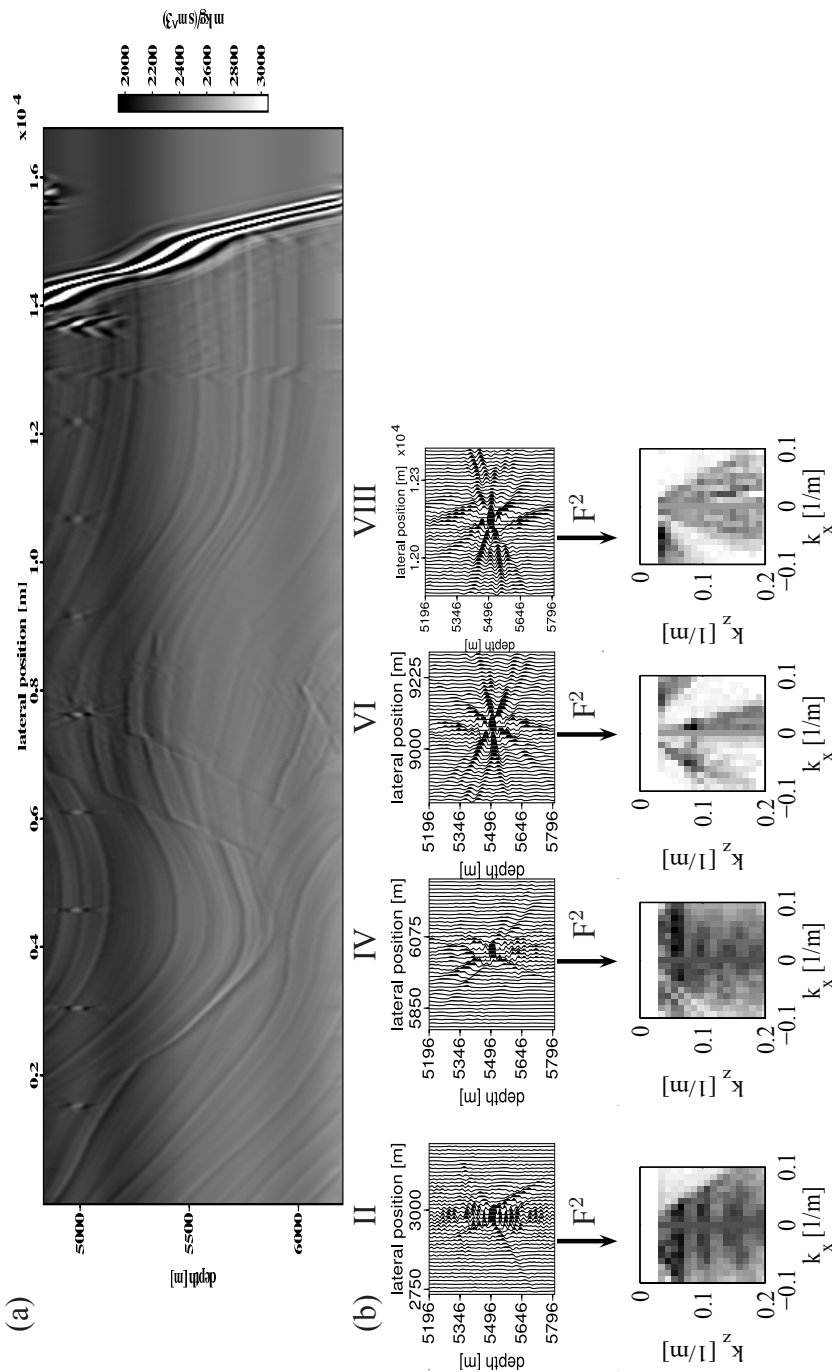
Figure 4.35: (a) Simulated constrained sparse-spike inverted data using nine $x - \omega$ approximated angle filters. (b) Four of the nine $x - \omega$ approximated angle filters that were used to simulate figure (a). The $x - \omega$ approximated angle filters are shown in the space domain above and double-Fourier domain below.
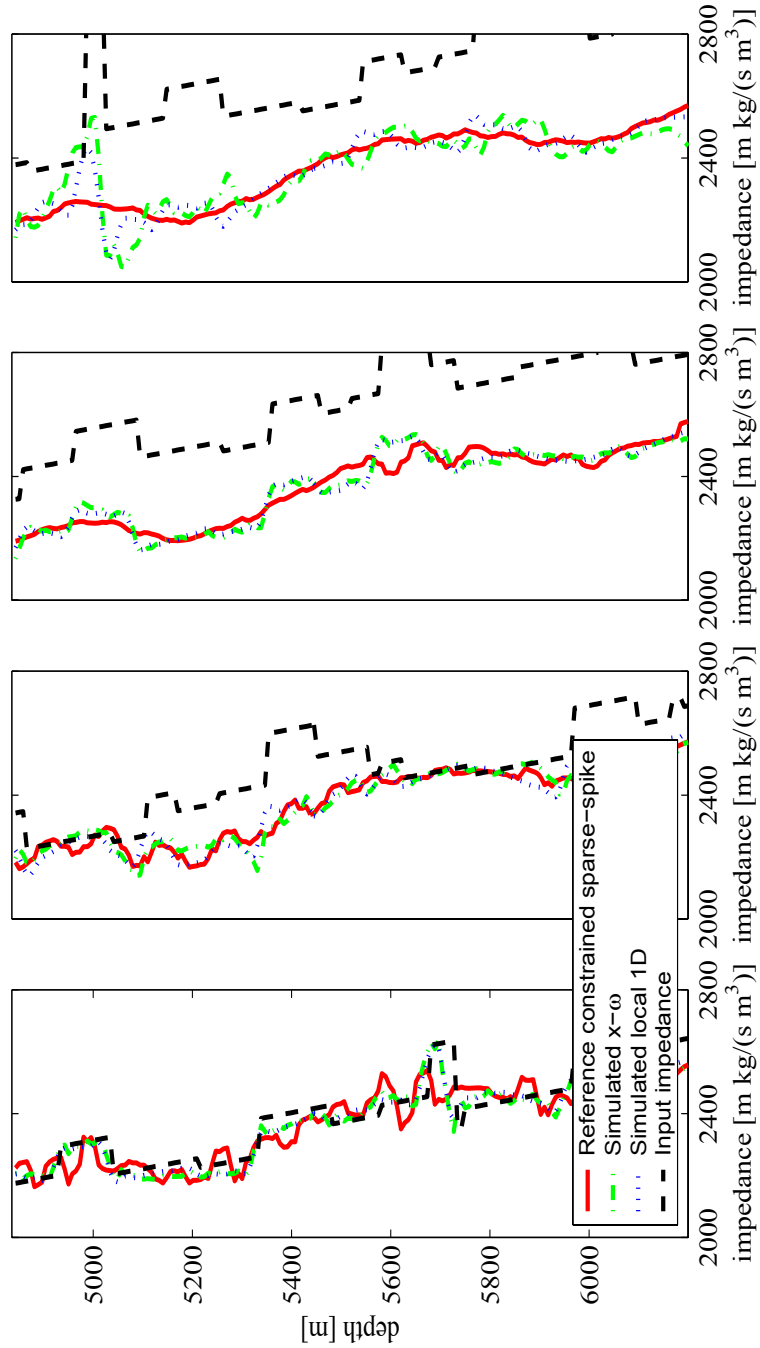
Figure 4.36: Comparing horizontal traces at lateral positions 3429, 6858, 10287 and 13716 m, respectively. Traces are taken from Figures 4.33 (a), (b), 4.34 (a) and 4.35 (a).
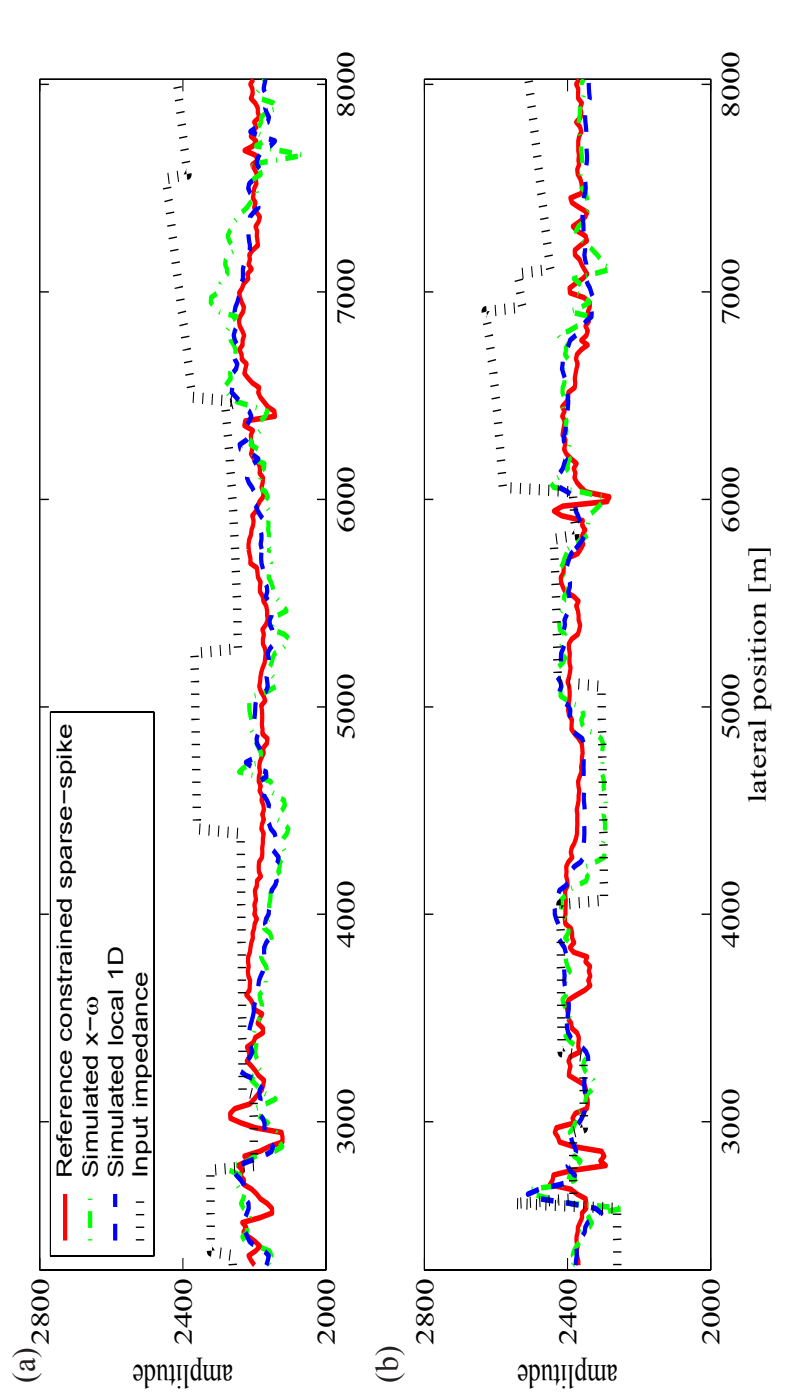
Figure 4.37: (a) Depth slice at positions 5150 and (b) depth slice at positions 5150 m of Figures 4.33 (a), (b), 4.34 (a) and 4.35 (a).

(a) A Norwegian stamp shows the archaeological excavation of the ship Oseberg. (b) A Marshall Island stamp shows the ship of Captain Cook, Resolution, in action.

In the next chapter, the potentials of the developed methodology are explored using a real seismic data-set of the Oseberg area (Figure 5.1), which is named after a Viking ship.

The focus in this area is on a geological formation named Cook, it fits in an alphabetically composed lists of the following formations (Figure 5.3). From base to top these are;

Amundsen, Roald, was a Norwegian polar explorer.

Burton, Sir Richard Francis, was a famous explorer, linguist and studied the Asian cultures.

Cook, James is a British explorer and navigator. On his second journey he commanded the *Resolution* to explore the unknown "south island", Antarctica.

Drake, Sir Francis, was an English privateer, navigator, naval pioneer and raider, politician and civil engineer of the Elizabethan era. He was the first captain to circumnavigate the Earth.

(This information is obtained from *Encarta Reference Library* (2003 edition) and http://www.Wikipedia.org.)

5

Evaluation of the methodology with a real-data example

After an initial large-scale seismic interpretation study of the Cook Formation in the Oseberg Field (offshore Norway) inclined internal reflectors are interpreted in the Cook Formation (Figures 5.1 and 5.2). The seismic interpretation raises the question about what geological setting has created them. Unfortunately, from a reservoir analysis based on the correlation of core description and wire-line logs, several options for a facies interpretation are possible. This is because of the large well spacing (2-3 km on average), low vertical resolution of the seismic data, and the stochastic approach for interpolation. In order to solve this, a shared-earth modeling study is performed to test multiple geological scenarios. It consists of the following three steps.

[1] Summary of the core, wire-line and large scale seismic interpretation studies, which conclude that the Cook Formation is formed in a tidal estuary environment. In order to compare the migrated real seismic image with the simulated migrated seismic image, input data on size and shape of reservoir elements in such a depositional setting are

needed. Recent analogue data sets provide the necessary detail and 3-D data to fill the need. For this study the Gironde and Western-Scheldt Estuaries are selected.

[2] An overburden model is used to compute one zero-offset spatial resolution and the corresponding approximated angle filter. The zero-offset spatial resolution filter is used to perform an enhanced seismic-to-well tie.

[3] In an iterative modeling approach, two different geological scenarios are tested. Relevant wire-line data of the Cook Formation are assigned to the different facies in the geological model and simulated prestack depth-migrated and constrained sparse-spike inverted data are computed by filtering the earth model using the spatial resolution and approximated angle filter, respectively. As an initial approach, the comparison of the simulated and real data is based on a visual inspection. In order, to obtain a closer fit, the size and shape of the facies elements of the geological model are manually varied within the ranges (uncertainties) obtained from a modern-analogue study.

The discussion is further supported by Chapter 6, where a multi-scale analysis is performed to correlate wire-line and 3D constrained sparse-spike inverted data.

5.1   Geological setting of the Cook Formation

The Cook Formation (Late Pliensbachian, Early Jurassic) consists of sandy to heterolithics facies. In the Oseberg Field the formation attains a total thickness of approximately 125 m. According to Færseth and Ravnås [1998], the Cook Formation is formed in a pre-rift setting in an estuarine to shallow marine environment. The base is a sequence boundary incising into marine mudstones of the Amundsen Formation (Sinemurian to Early Pliensbachian). The Cook Formation is conformably overlain by marine mudstones of the Drake Formation. These deposits are part of the Dunlin Group, which lies directly below the reservoir deposits of the Brent Group (Figure 5.3). The Oseberg area underwent extension along eastward dipping
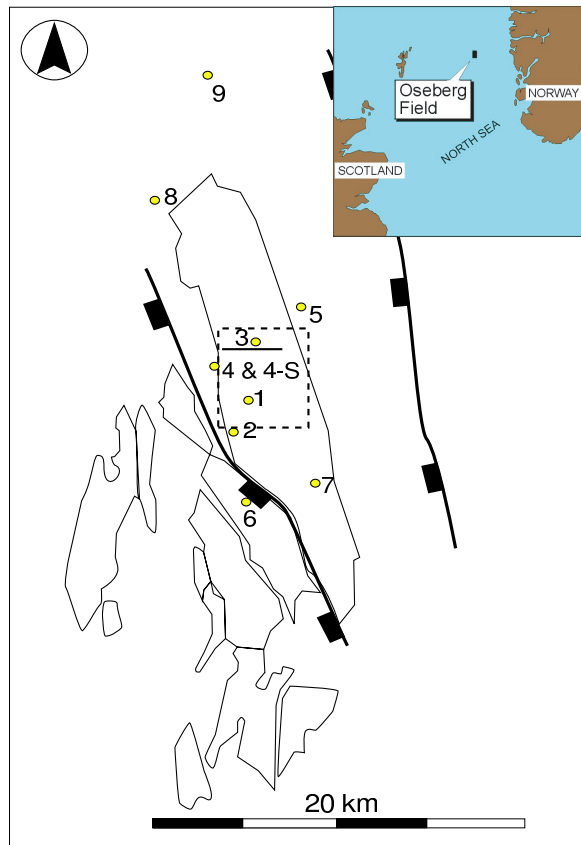
Figure 5.1: Location of the Oseberg Field. The numbers label well locations of which wire-line and core data are studied. The solid line indicates a selection of a west-east migrated seismic image. The small rectangular dashed box indicates the area of the 3D migrated seismic data that is used in the constrained sparse-spike seismic inversion process. This subset is chosen such that the area of the Oseberg fault, where the migrated seismic data suffer imaging problems, is excluded. The geological complexity of this area is highlighted by a number of interpreted faults blocks (contoured lines).
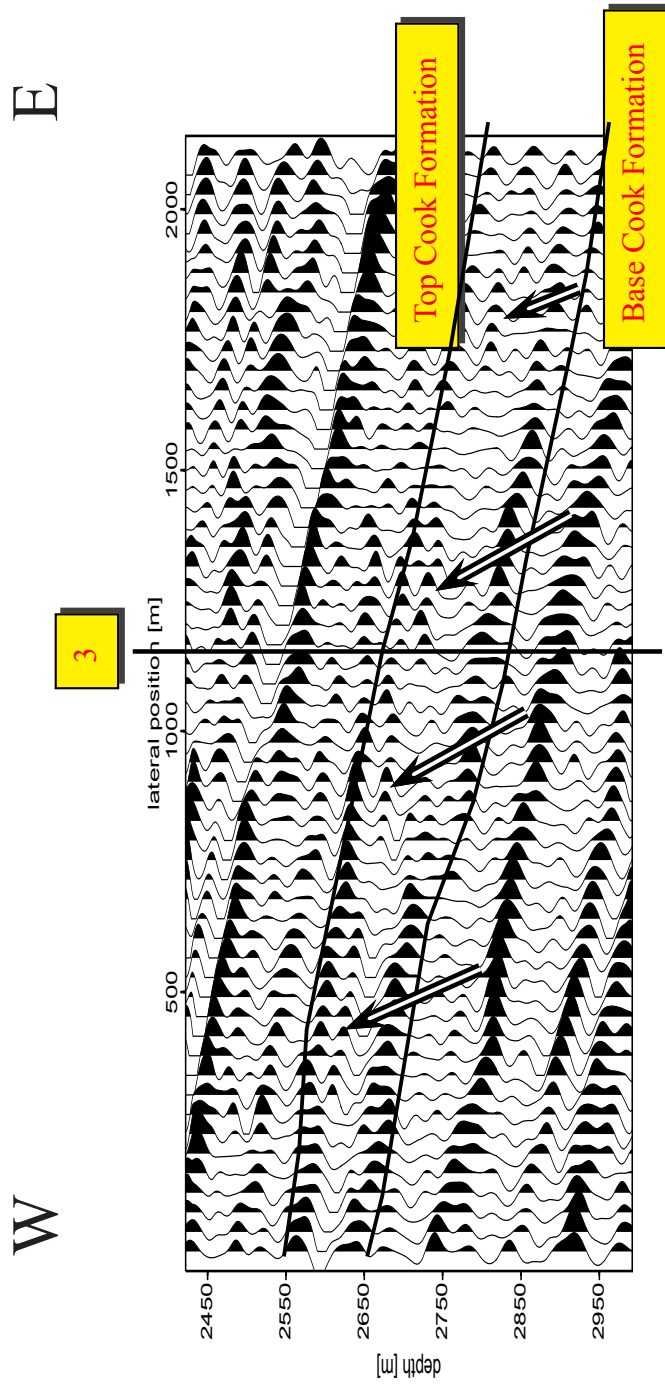
Figure 5.2: A representative image of the Cook Formation, plotted using AGC. With good well control and modern 3D interpretation techniques, the base and top of the Cook Formation (indicated by the solid lines) were interpreted. The arrows indicate inclined internal reflectors that are subject to the iterative shared-earth modeling study presented in this chapter. See Figure 5.1 for the location.

Period		Stage	West ⟶ East
Jurassic	Middle	Callovian	Viking Group
		Bathonian	
		Bajocian	Brent Group
	Lower	Toarcian	Drake Fm.
		Pliensbachian	Cook Fm.
		Sinemurian	Burton Fm. Johansen Fm.
			Amundsen Fm.
		Hettangian	Statfjord Fm.
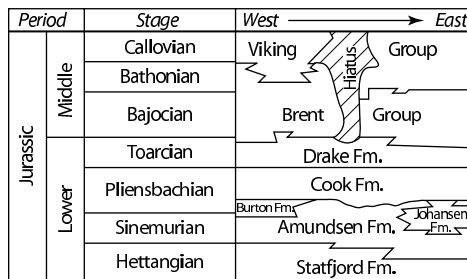
Figure 5.3: *Stratigraphic setting of the Upper Pliensbachian (Lower Jurassic) Cook Formation in the offshore of the northern North Sea. Modified from Marjanac [1995] and Vollset and Doré [1984].*

faults during the Permo-Triassic rifting phase. During the Mid-Jurassic rifting phase the extension concentrated along westward dipping faults. This resulted in a north-east tectonic dip of $\approx 8°$.

The Cook Formation is subdivided into three units on the basis of its lithofacies associations. From base to top these are:

- Cook-1 formed as an estuarine complex of tidal channels and bars with adjacent tidal flats. The deposits are confined to a funnel-shaped estuary that opened and deepened to the northwest. The sand-prone part of the estuarine fill is concentrated in the center of the basin; towards the edges the sand-to-shale ratio decreases.

- Cook-2 is a thin unit of marine clays with a small silt fraction.

- Cook-3 formed after a renewed relative base level fall and associated truncation. The Cook-3 deposits formed in a less sheltered estuarine environment connected to the adjacent open marine environment. Sand-prone estuary mouth deposits laterally grade to muddy tidal flat and marsh deposits.

■ 5.1.1   Lithofacies analysis and environmental interpretation

The lithofacies associations of the Cook Formation were analyzed from cores of four wells: 2, 8, 9 and 4 (Figure 5.1). The Cook-1 unit is present either partially or completely in all cores. The Cook-2 unit is only clearly discernible in well 9 (the most northern well). The uppermost unit, Cook-3, is present in all wells, although the contact with the overlying Drake shales was not cored in any of the wells.

■ 5.1.2   Lithofacies description

The lower part of the Cook-1 unit in the studied wells is characterized by thinly bedded (bed thickness 10 to 50 cm) heterolithic sediments with varying sandstone-to-mudstone ratios, ranging from 0.5 to 0.8 (Figure 5.4 (c)). Characteristic double mud drapes are a prominent feature. The thin sandstone layers are lens-shaped and show cross-lamination. The heterolithic beds generally have a low bioturbation grade, with *Planolites* burrows being the most common ichnofossil type. Plant roots and wood fragments occur in the lower part [Dalman et al., 2003]. Well-sorted very-fine to fine grained thickly bedded sandstone layers overlie this lower part in the Cook-1 unit. The sandstone is cross-bedded or shows meter-thick intervals of inclined bedding, accentuated with mud drapes (Figures 5.4 (a) and (b)). Double mud drapes are a common feature and regular increase and decrease of the mud drape spacing is discerned in the sandstone beds (Figure 5.4 (a)). The bioturbation degree is low. Based on the sedimentary structures in combination with the low bioturbation grade, the deposits are interpreted as having been formed in an estuarine tidal environment. Double mud drapes are a diagnostic criterion for such an environment. The cross-bedded sandstone layers with mud drapes formed in a tidal channel. The inclined sandstone deposits with mud drapes are typical for tidal point bars in the landward part of the estuary. The regular change in mud drape spacing is an expression of cyclic neap-spring variations in tidal current energy [Nio and Yang, 1989]. The coarsening upward succession in the Cook-1 unit from a heterolithic to a sand-dominated facies indicates a gradual increase of the estuarine volume and an associated higher tidal energy. The Cook-2 unit is only present in well 8; further to the south, the Cook-3 unit directly overlies the Cook-1 unit. The Cook-2 unit consists of a meter-thick clay layer with a marine fos-

sil assemblage such as belemnites. In other Norwegian offshore fields, the Cook-2 unit is a clear marker often used for correlation. The Cook-3 unit is characterized by thickly bedded, fine-to-coarse grained, cross-bedded sandstone. Clay rip-up clasts may line the foresets, and occasional clay drapes occur. However, double mud drapes are absent. In places, the bioturbation is strong and obliterated the primary sedimentary structures. *Teichichnus* is a common ichnofossil, and occasional belemnites are found. On the basis of the occurrence of clay drapes and fossil indicators, the Cook-3 unit is interpreted as having been deposited in a shallow marine, tidally influenced environment, probably as tidal sand bars [Dalman et al., 2003].

Thus, based on the correlation of the 1D data, two earth models fit the core and wire-line data. These two scenarios describe a *valley infill* or *east-west migrating channels and tidal sand-bars*.

■ 5.1.3   Correlation panels

In order to obtain information about the lateral extent of the facies of the Cook Formation, the core and wire-line data are correlated. The wire-line interpretation is conducted by traditional comparison of predominantly the gamma-ray, partly the rock-density and P-wave velocity logs. The gamma-ray log is used for the correlation, since it provides the best indication of lithofacies (i.e. especially sand-shale ratios [Luthi, 2001]). The top and base of the Cook Formation can usually be picked easily. However, the position of internal boundaries (e.g., base of the Cook-3 unit) can be quite ambiguous. Therefore, a seismic modeling study forms an essential part to support shared-earth modeling. The log character of the Cook-2 marine mudstone, sandwiched between two units of medium-grained sandstone, is well defined and intervals nearly unmistakable. Obviously, the sandy correlate with the lower gamma-ray values and the shale-rich cores correlate with the higher gamma-ray values [Dalman et al., 2003].

Based on the correlation panels for well 3, the correlation is shown between the rock-density, P-wave velocity and facies interpretation (Figure 5.7). This information is used to assign relevant wire-line data to the different facies in the two different earth models studied later on.

■ 5.1.4   A seismic attribute map

The cosine of the phase is computed around the interpreted base of the Cook Formation (Figure 5.8). The resulting map of this seismic attribute shows a funnel-shaped area that is interpreted in analogy with modern settings (Figures 5.9 (a) and 5.10), as a tidal estuary.
This however, has to be taken with care, because this seismic attribute does not detect a specific geological feature, and it may also be (partly) related to seismic uncertainties. For example, the north-south oriented correlation panel shows that the Cook-1 unit is also present in well 4, which lies outside the interpreted funnel shown in Figure 5.8. In order to better understand the seismic attributes, the attribute should be tested on simulated prestack depth-migrated data.

■ 5.1.5   Studying modern analogues

The core analysis results show that the sediments of the Cook Formation formed in a tidal estuarine environment. The shape of the estuary is visualized with a seismic attribute map, It shows a north-west to south-east elongate funnel shape that opens to the sea in the north-west. The length and width of the funnel shape are 15 km and 5 km, respectively (Figure 5.8). In order to compare the migrated real data with the simulated migrated seismic data, input data on size and shape of reservoir elements in such a depositional setting are needed. Modern-analogue data sets provide the necessary detail and 3D data to fill the need. It is therefore of paramount importance to derive these data from settings with a high degree of analogy, i.e. the basin shape, size and hydrodynamic regime should be similar. For this study, the following two analogues are selected, i.e., the Gironde and Western-Scheldt Estuaries. Both estuaries were formed during the last Pleistocene glacio-eustatic lowstand, when rivers incised deep valleys into the coastal plains. Subsequently, Holocene glacio-eustatic sea level rise flooded the incised valleys and converted them into tidal estuarine basins.

Gironde Estuary

The Gironde Estuary has a funnel shaped opening to the Bay of Biscay in the north-west (Figure 5.9). The estuary has a meso-tidal regime, 2 to 4 m tidal difference, and consists of a set of north-west to south-east elongated tidal bars bordered by deep tidal channels [Fenies and Tastet, 1998]. From
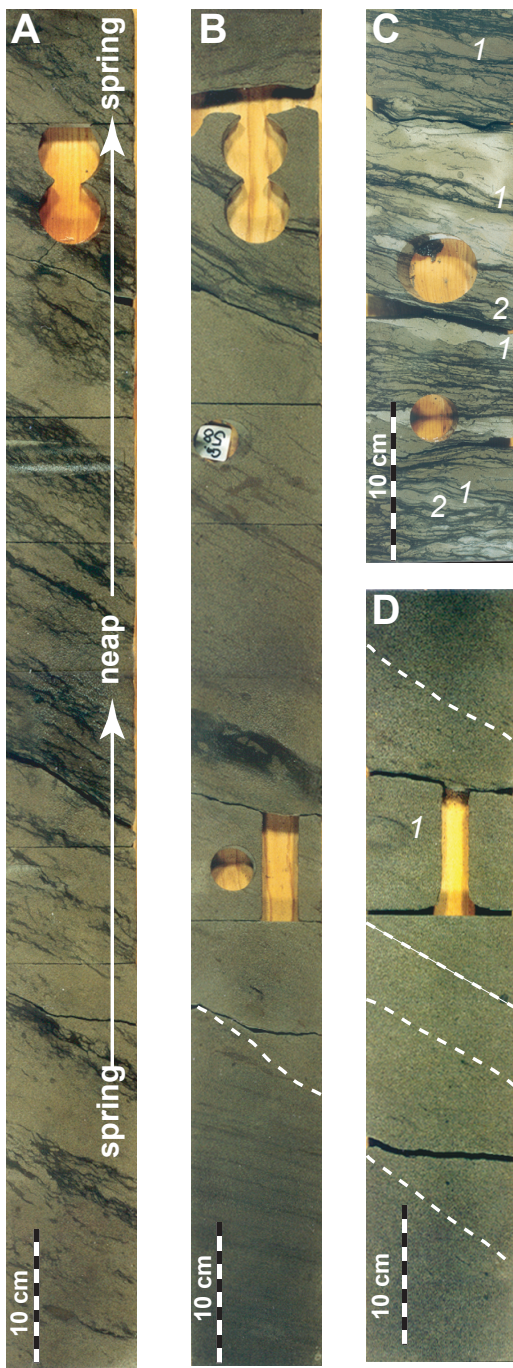
Figure 5.4: Lithofacies characteristics of the Cook-1 and Cook-3. (A) Cross-bedded fine sand with double mud drapes. The low bioturbation grade and the vertical succession of sand-rich to mud-rich and again sand-rich facies, is interpreted as a spring-neap-spring tidal cycle in an estuarine tidal point-bar. Well 4 (Cook-1), from 2489 to 2490 m depth. (B) Cross-bedded very-fine to fine sand with occasionally mud drapes. The change in dip angle above the reactivation surface (illustrated by the dashed line) and the low bioturbation grade is interpreted as cross-bedding in a tidal channel. Well 4 (Cook-1), from 2484 to 2485 m depth. (C) Heterolithic deposits consisting of centimeter-thick thin-flat to lens-shaped silt and very-fine sand layers and mud laminae with double-mud drapes (1) Low bioturbation grade with Planolites burrows (2) interpreted as sub-tidal flat flaser and lenticular deposition in an estuarine environment. Well 9 (Cook-1), from 3763.26 to 3763.64 m depth. (D) Cross-bedded fine grained sandstone of the Cook-3 unit. Occasional clay rip-up clasts on the foresets (1). Mud drapes are absent on the foresets (illustrated by the dashed line), compare with (A). Well 4 (Cook-3), 2471.5 to 2472.0 m depth.
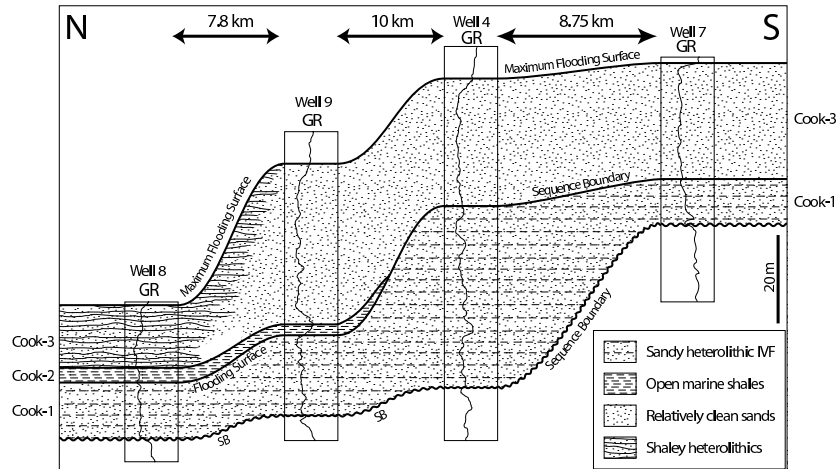
Figure 5.5: North-south facies correlation across the greatest thickness of the Cook Formation in the Oseberg Field. The northward deepening of the Amundsen-Cook boundary is interpreted as the increase in fluvial incision depth in this direction following relative sea level fall. The subsequent sea level rise transgressively filled the incised valley with estuarine Cook-1 and marine shales of the Cook-2. The landward part of the Cook-2 was eroded during the next sea level fall. The Cook-3 unit formed during the next transgression. See Figure 5.1 for well locations.

Unit	Length [km]	Width [km]	Height [m]
I	12	1.9	16
II	8	2.8	14
III	13	1.4	8

Table 5.1: Size and shape data of individual tidal sand-bars in the Gironde Estuary. See Figure 5.9 for tidal-sand bar locations.

published data and bathymetric maps [Kapsimalis et al., 2004], an excellent size and shape data set was derived of the tidal sand-bars and channels (Table 5.1).
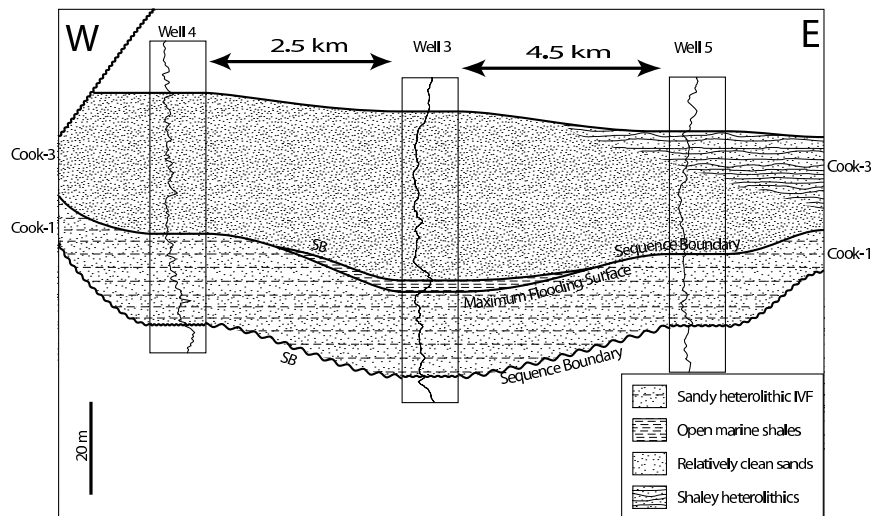
Figure 5.6: *A west-east facies correlation shows the concave valley shape at the base of the Cook Formation See Figure 5.1 for well locations. It is noted that the vertical scale is strongly exaggerated.*

Western-Scheldt Estuary

The Western-Scheldt Estuary is a sinuous east-west oriented estuarine basin that opens to the North-Sea in the west (Figure 5.10). As in the Gironde Estuary, elongate tidal sand-bars are bordered by deep tidal channels. The estuary has a meso-tidal to macro-tidal regime with a maximum of 5.5 m tidal difference. The size and shape data were measured from detailed bathymetric maps [Hydrografie, 2003] (Table 5.2). A schematic cross-section through a set of tidal sandbars inside an estuary is shown in Figure 5.11.

(a)   (b)   (c)
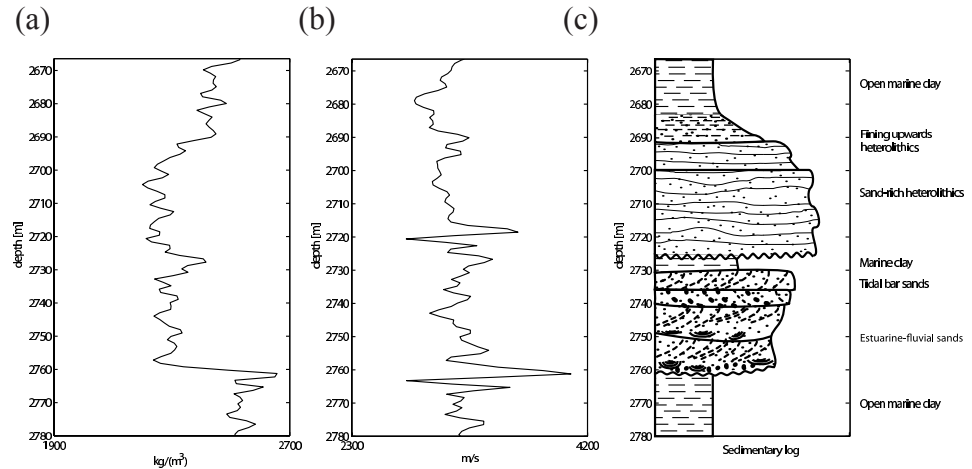
*Figure 5.7: Wire-line logs and corresponding facies interpretation of well 3. (a) Rock-density response. (b) P-wave velocity response. (c) Facies interpretation, based on well-log response.*

Unit	L [km]	W [km]	H_n [m]	H_s [m]	A_n [°]	A_s [°]
1	16	4	23	15	0.4	2.3
		2	20	14		
2	13	3	15	15	1.0	3.8
		3	18	28		
3	11	3	33	19	0.6	1.9
4	16	5	14	28	1.7	5.0

Table 5.2: Size and shape data of the tidal sand-bars in the Western-Scheldt Estuary (Figure 5.10). L, W, H, A denote the length, width, height and local dip angle of a tidal-bar, respectively. Subscripts n and s denote that the height and local dip of one tidal-bar were measured approximately in the northern or southern direction, respectively.
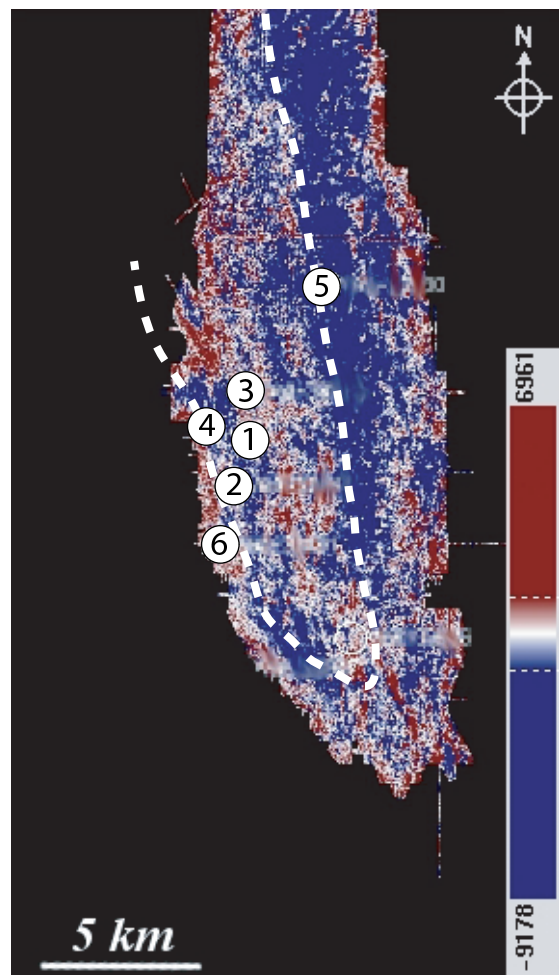
*Figure 5.8: Horizon slice of the migrated data, 15 ms (approximately 23 m) above the base of the Cook Formation The estuarine funnel shape is outlined (dotted line). It is noted that the geological interpretation is based on the observed amplitude variation, but there is not a direct link with the results of the log data. The amplitude values are plotted with use of AGC (indicated by the color bar).*
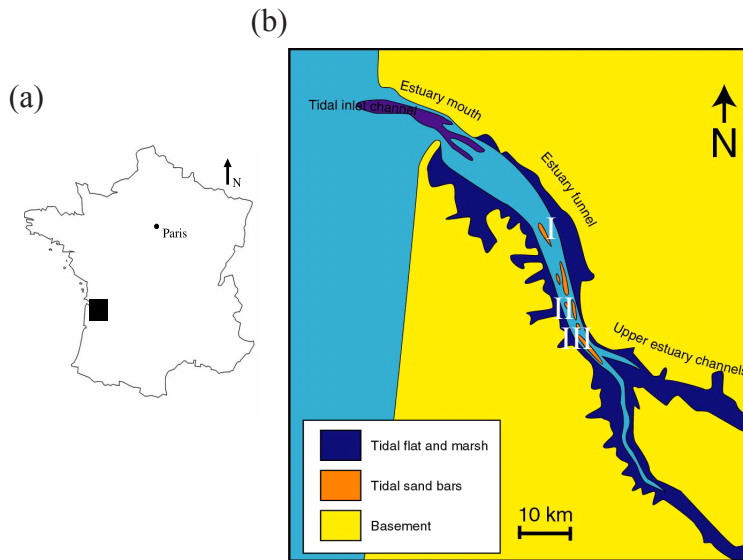
Figure 5.9: (a) In the south-western part of France the Gironde Estuary is present (black box). (b) A schematic illustration of the Gironde Estuary. In red the tidal sand bars are indicated. The tidal-bars that are labeled I to III, where used to perform the size and shape measurements (Table 5.1).

5.2   Time-to-depth converted prestack time-migrated data

The main processing steps carried out to obtain the 3D prestack time-migrated seismic data are as follows;

The raw seismic data are obtained by merging two overlapping seismic surveys. Before the merging step is done, both data are filtered using a low-frequency (0 to 6 Hz) and a high-frequency (70 to 75 Hz) filters. Further, the source signature of the seismic data is estimated and reshaped to a zero-phase wavelet that is also known as a Ricker wavelet. A mute in the τ-p domain is used to attenuate multiple scattering related to the water bottom. Next, the two survey grids are merged and a Kirchhoff prestack time-migration algorithm followed by one residual normal move out correction step is run to

compute the 3D prestack time-migrated data. A time-to-depth conversion is then performed using the P-wave velocity of well 3. The discretization of the migrated seismic data is 12.5 m in the west-east direction, 18.75 m in the north-south direction and 1 m on the depth axis.

In general, the reflectors of the base and top of the Cook Formation are coherent in this data-set. However, at particular lateral positions the continuity of all reflectors is disrupted. This is mainly caused by shallow gas pockets, which have caused difficulties for the migration algorithm used to properly image the input data [Lindanger et al., 2004]. Another issue of the migrated data is that the multiple removal algorithm used is most effective for attenuating water-bottom multiple energy in the far-offset data [Hill et al., 1999]. This means, that in the final stacked data-set, which consists of a stack of near-, mid- and far-offset data, multiple scattering can complicate the seismic interpretation. It is tacitly assumed that all multiple scattering have been properly removed from the real data or imaged to its correct position of origin.

■ 5.2.1 Synthetic overburden model and filters

A proper overburden is crucial to derive the spatial resolution filter that is used to simulate prestack depth-migrated and inverted data as, e.g., illustrated in Section 3.2. Unfortunately, the migration velocity model of the real data is not supplied. Therefore, a 2D acoustic overburden model of the Oseberg area is constructed with the aid of the available wire-line data and regional geological knowledge of the Oseberg area (Figure 5.12 (a)). The lateral distance of the model corresponds to the total recording aperture of the two data-sets.

Near well 3 (x = 6500 m) in the middle of the Cook Formation interval (z = 2700 m), a spatial resolution filter is calculated by constructing an angle and a band-limitation filter in the double Fourier domain. The angle filter is constructed from ray-tracing through a smoothed version of the synthetic migration model, where the maximum angles of wave propagation are $\varphi_1 = 60°$ and $\varphi_2 = -20°$. The band-limitation filter is constructed from a time-to-depth converted Ricker wavelet, which phase is rotated $5°$, and which has a maximum frequency content of 70 Hz. For more information on the phase rotation, see the discussion in the next two sections.

Figure 5.10: The Western-Scheldt Estuary in the southwest of The Netherlands. Elongate inter-tidal sand bars (light colors) fringe deep sub-tidal channels (dark). The major part of the estuary has a meso-tidal range; the range of the semi-diurnal tide varies from about 3.8 m at the mouth to about 5.2 m at Antwerp (78 km upstream). Size and shape parameters (see Table 5.2) are measured from the following tidal sand bars: (1) Hooge Plaat; (2) Middelplaat; (3) Platen van Ossenisse; (4) Plaat van Walsoorden. A-B: cross section of Figure 5.11.
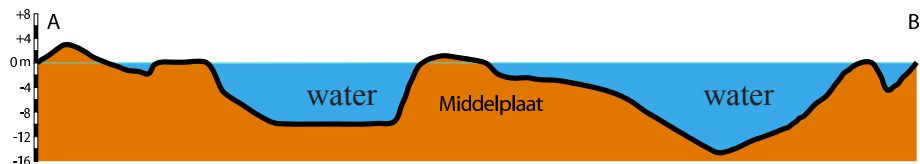

Figure 5.11: A cross section through the Western-Scheldt Estuary. The Middelplaat tidal sand bar has a steep side facing the southern tidal channel, and a gently dipping side on the north. See Figure 5.10 for location. Profile length A-B is 7.2 km.

Multiplication of both filters and a subsequent inverse Fourier transformation gives the spatial resolution filter (Figure 5.12 (b)). The corresponding approximated angle filter is computed by constrained sparse-spike inverting the spatial resolution filter (Figure 5.12 (c)). The discretization information of the filters is $\Delta x = 12$ m and $\Delta z = 1$ m.

5.3 Time-to-depth converted constrained sparse-spike inverted data

A subset of the 3D prestack time-migrated data is loaded into a commercial seismic inversion package to run a constrained sparse-spike inversion algorithm. The area of the subset is indicated by the small rectangular box in Figure 5.1. An important input to the inversion algorithm is an inversion wavelet. This wavelet is estimated using wire-line data and constrained by the seismic processing parameters. Using wire-line data from wells 1, 2 and 3, a zero-phased inversion wavelet is estimated which unfortunately has a very low correlation factor (≈ 0.2). For more information on how a correlation factor is calculated, see the discussion in the next section. One argument for the low correlation factor may be found in the fact that the seismic data are constructed from two seismic surveys, consequently estimating one inversion wavelet for the whole data may not be sufficient. A second argument is that the wire-line data may not be optimally aligned with the seismic reflectors.

A second estimate of an inversion wavelet is only based on the wire-line data of well 3, resulting in a Ricker wavelet whose phase is rotated by $0.5°$, and which has a correlation factor of ≈ 0.5. This inversion wavelet is used in a constrained sparse-spike inversion algorithm. After adding the low-frequency information, the constrained sparse-spike impedance data are time-to-depth converted using the P-wave velocity log of well 3. The low-frequency model is built with the aid of all three wells and uses the interpreted horizons of the base and top of the Cook Formation.
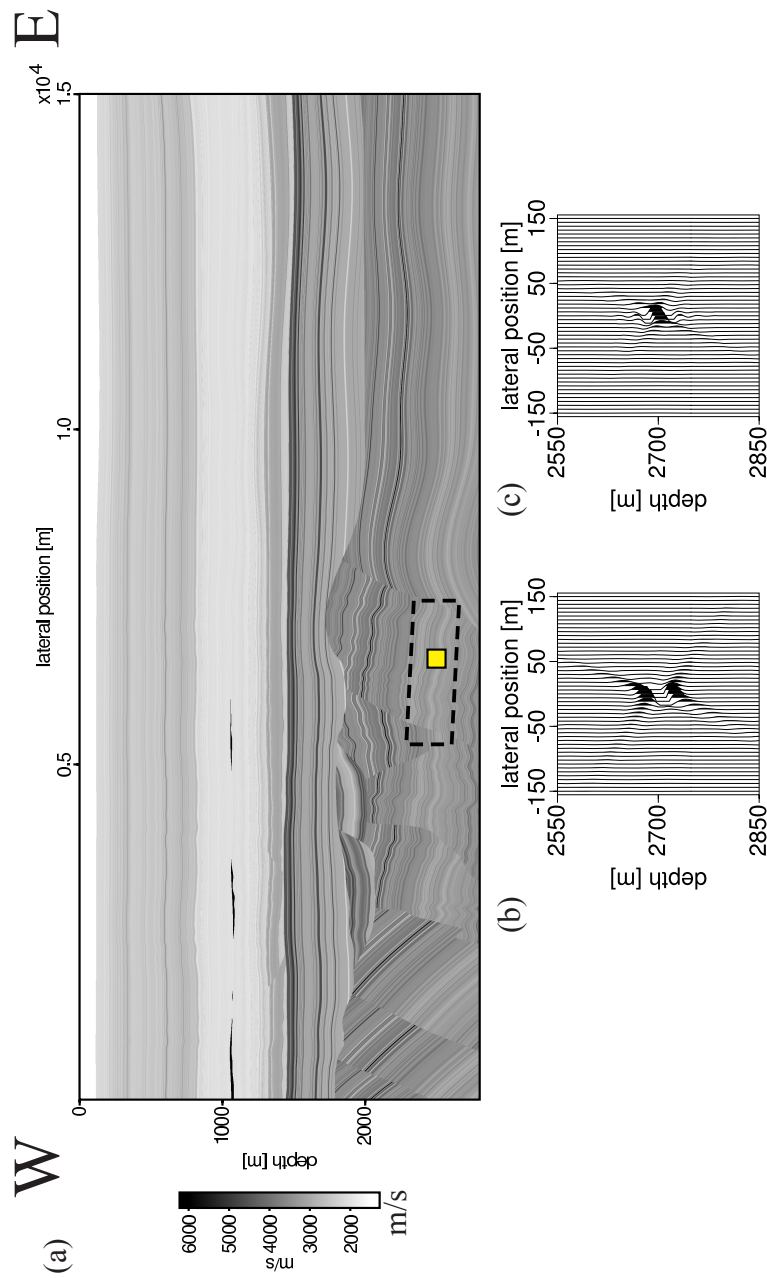
Figure 5.12: (a) A 2D synthetic overburden model of the Cook Formation. The dashed box indicates the target-zone for geological interpretation of the Cook Formation. (b) A spatial resolution filter near well 3 (x = 6500 m) in the middle of the Cook Formation interval (z = 2700 m). (c) Corresponding approximated angle filter of figure (b).

5.4   Enhanced well-to-seismic tie using dip-panels

A well-to-seismic tie is an important starting point for seismic interpretation [White and Simm, 2003]. The industry practice is to compute a 1D seismic trace formed by a 1D convolution in the vertical direction between a wavelet and a reflectivity trace that is derived from wire-line data. By displaying side-by-side successive 1D traces, a (small) 2D seismic image is simulated. By visually comparing this simulated image with the migrated real data, it is judged whether the wire-line data are properly aligned with the migrated real data. Additionally, a correlation factor can be computed.

Unfortunately, the 1D convolution model is based on the assumption that the Earth is horizontally layered, therefore it only expresses for horizontal layers the vertical resolution of a migrated real seismic image and it does not account for the lateral resolution aspects of the migration process. A-priori regional geological information, e.g., dip-meter measurements can be used to judge if this is a correct assumption or not. For example, the Cook Formation is dipping approximately at $8°$. In order to handle such a geological dip a so-called dip-panel is introduced. A dip-panel consists of one dipping layer, where reflectivity values are assigned to. By filtered a dip-panel with a spatial resolution filter, migrated prestack depth-migrated data are simulated that can be compared directly with the migrated real data.

The enhanced seismic-to-well tie is illustrated for the Cook Formation. Figure 5.13 (a) shows seven traces (Common Depth Point (CDP) positions 90 to 98) of the migrated real seismic data around well 3. From the wire-line data, under a normal-incidence assumption, one reflectivity trace is computed (Figure 5.13 (b)). Next, seven different dip-panels are created with a dip range between $12°$ to $-12°$ in steps of $4°$ and the reflectivity trace is assigned to the layered models. In order to simulate prestack depth-migrated data, the dip-panels are filtered by the spatial resolution filter (Figure 5.12 (b)). Figures 5.13 (c) to (i) show the result.

∎ 5.4.1   Discussion on the dip-panels

The industry practice is that the $0°$ dip-panel (that equals the result of the 1D convolution model), is used to perform a well-to-seismic tie (Figures 5.13 (a) and (d)).

The dip-panels enhance this approach by revealing dip information of seismic reflectors. For the Cook Formation, the base and top show a dip that is approximately equal to the dip of the $8°$ dip-panel (solid lines in Figures 5.13 (a) and (d)). The $8°$ dip is the result of tectonic deformation during a rifting phase (Section 5.1). The inclined internal reflector dip is approximately $-4°$ dip-panel (dashed line in Figures 5.13 (a) and (g)). This fits the averaged value of the measured steepest dip of one tidal sand-bar that is $\sim 3°$ (Table 5.2). Therefore, the inclined internal reflector could be interpreted as a tidal sand-bar. This is further investigated by the iterative shared-earth modeling study.

Finally, focus at the depth position of the different reflectors. Only the top of the Cook Formation is properly aligned with the top in the $8°$ dip-panel. Both the base of the Cook Formation and the inclined internal reflector are approximately 25 m too shallow, compared to the position in the wire-line data. This observation, may be the main reason for the low-correlation factor that is found in the inversion wavelet estimation process of the previous section.
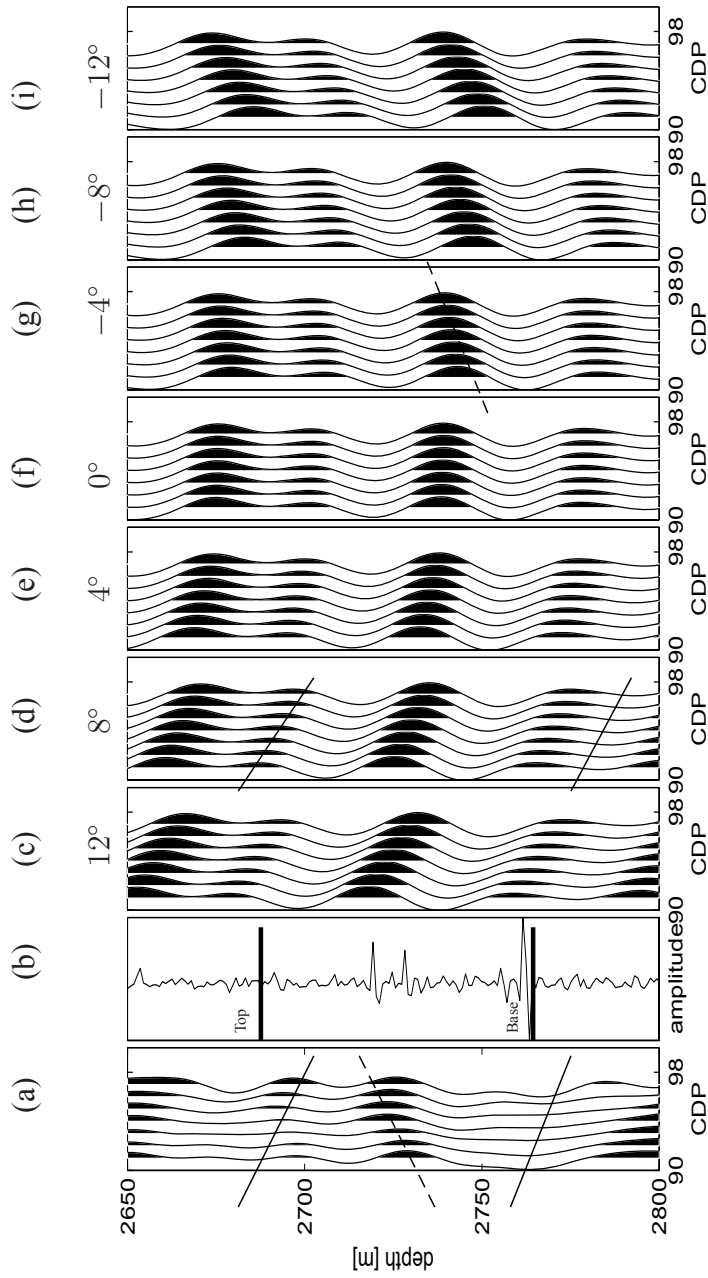
Figure 5.13: *(a) Seven traces of the migrated real seismic data around well 3. (b) Normal-incidence reflectivity log from well 3. (c) to (i) Simulated prestack depth-migrated of seven different dip-panels, obtained after a multidimensional spatial convolution between one of the seven dip-panels and the spatial resolution filter of figure 5.12 (b). Solid lines indicate the base and the top of the Cook Formation, respectively. The dashed line indicate an inclined internal reflector of the Cook Formation.*

5.5   Iterative shared-earth modeling

A common approach is to build a 3D geological scenario from essentially 1D data through the correlation of wire-line and core data. Consequently, different detailed geological scenarios are constructed that all fit the measured data. From the previous discussion on the wire and core data, two geological models fit the core and wire-line data of the Cook Formation. These models describe a *valley infill* and *east-west migrating channels and tidal sand-bars*, respectively. An iterative shared-earth modeling approach is used to find the best fitting model by visually comparing (regarding the phase) simulated migrated and inverted data with the migrated and inverted real data. Relevant wire-line data of well 3 are assigned to the different facies in an earth model (Figure 5.7) and in order to preserve small scale geological features, the facies models are discretized at dz = 1 m and dx = 3 m. Consequently, the spatial resolution and approximated angle filters are sinc-interpolated to this smaller discretization. The simulated migrated and inverted data are computed by filtering a 2D earth model by the spatial resolution and approximated angle filter, respectively. Finally, the size and shape data obtained from the modern-analogue study are used to incorporate geological uncertainties. As an initial approach, the reflectivity is derived under a normal-incidence approximation.

■ 5.5.1   Geological scenario I: valley infill

The first scenario attempts to recreate the inclined internal reflectors of the Cook Formation by modeling an aggradational incised valley fill. The inclined internal reflectors are modeled by the infill and consequent onlapping of the sediments on the erosional base. The geological model only shows the west side of the incision (Figure 5.14). The impedance model is shown in Figure 5.15. Near well 3, the model does only show the $8°$ tectonic dip, but does not take into account the results of the enhanced well-to-seismic-tie, namely that the inclined internal reflectors have a $-4°$ dip. Therefore, the simulated prestack depth-migrated image is not successful in recreating the inclined internal reflectors of the migrated real data (Figures 5.2 and 5.16). Probably, because the same earth model is used, the simulated constrained sparse-spike impedance image also does not match the constrained sparse-

spike real impedance image (Figures 5.17 and 5.18).

Finally, compare the impedance model with the simulated and real impedance image (Figures 5.15, 5.17 and 5.18). The simulated constrained sparse-spike inverted impedance image is much smoother than the impedance model and therefore the comparison between the simulated and the real impedance data is enhanced.

No further update of this geological scenario is undertaken and the second geological scenario is examined.
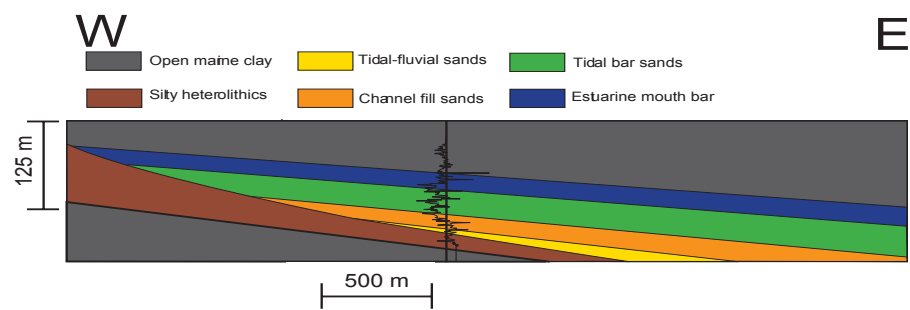
Figure 5.14: Scenario I: schematic illustration of a valley infill and the gamma-ray log response at well 3.
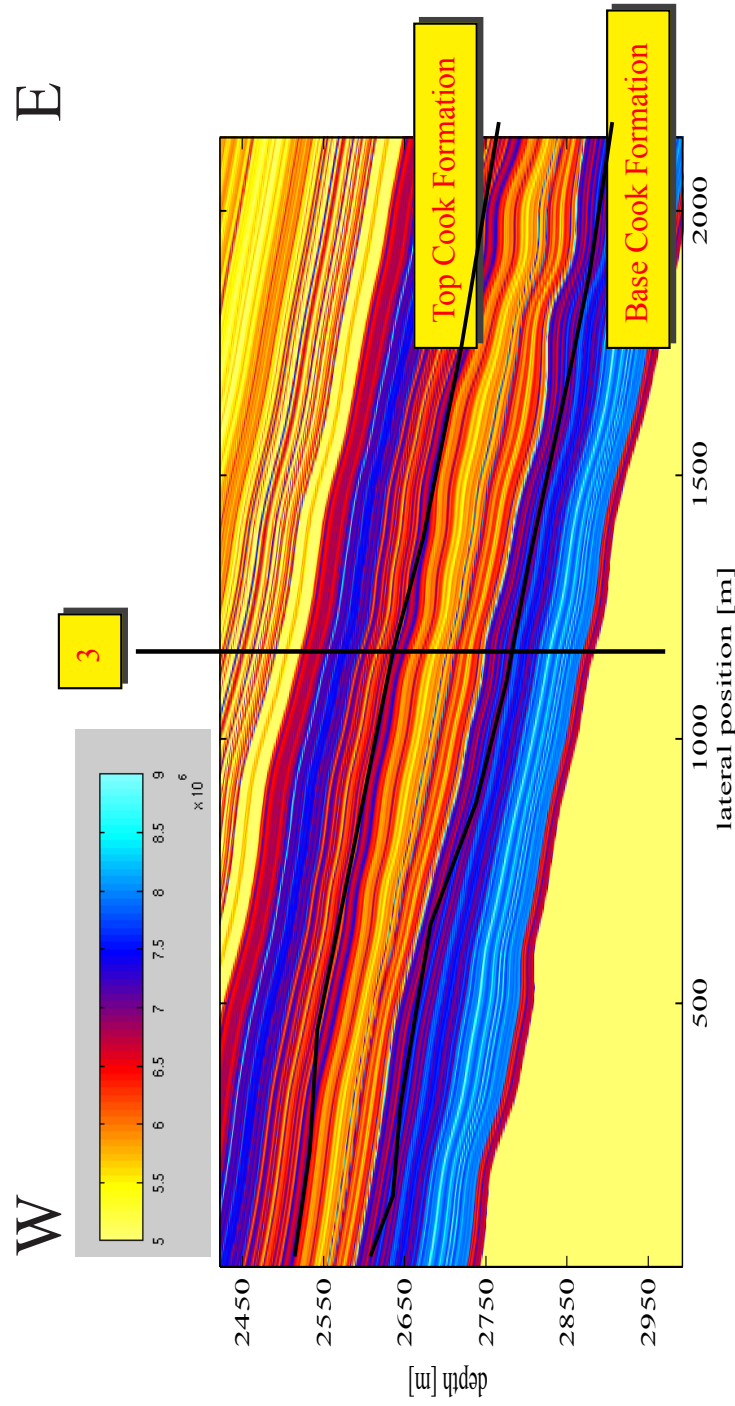
Figure 5.15: Scenario 1: impedance model of a valley infill. The solid lines indicate the base and top of the Cook Formation in the migrated real data, respectively. Impedance values are in [kg /(s m²)].
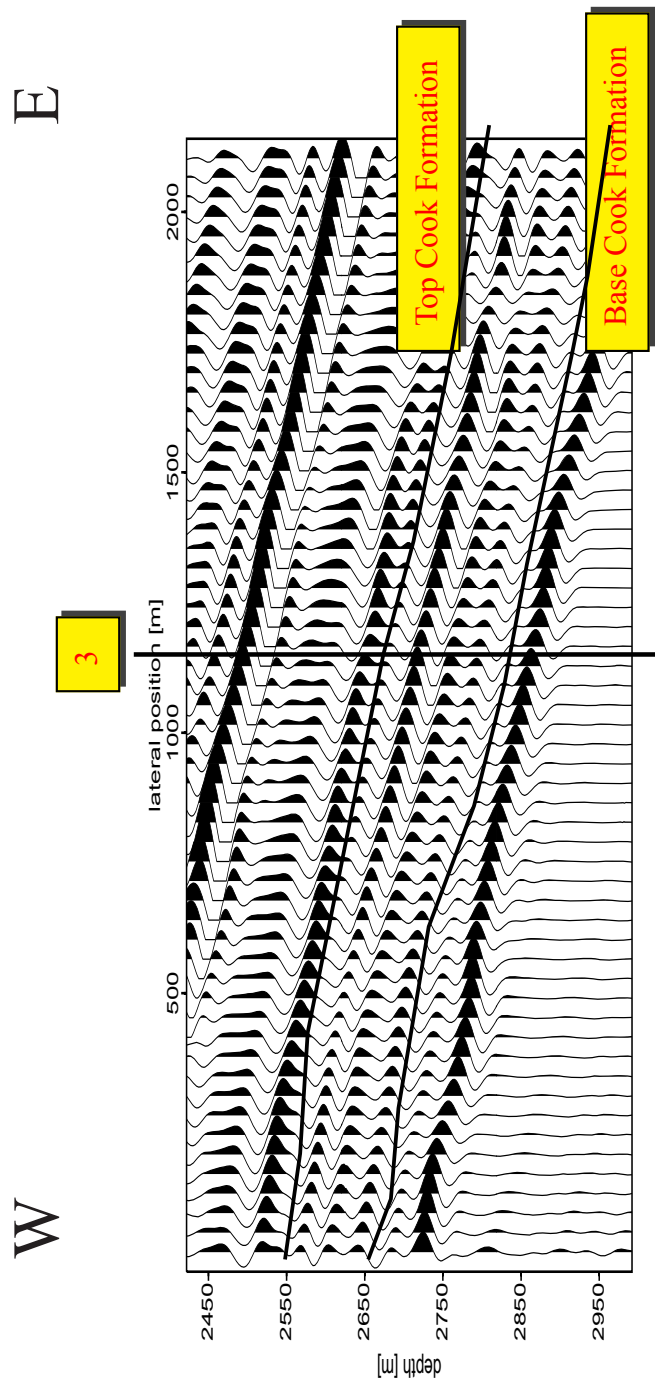
Figure 5.16: Scenario I: simulated prestack depth-migrated image, displayed using AGC. The solid lines indicate the base and top of the Cook Formation in the migrated real data, respectively. The inclined internal reflectors are not simulated.
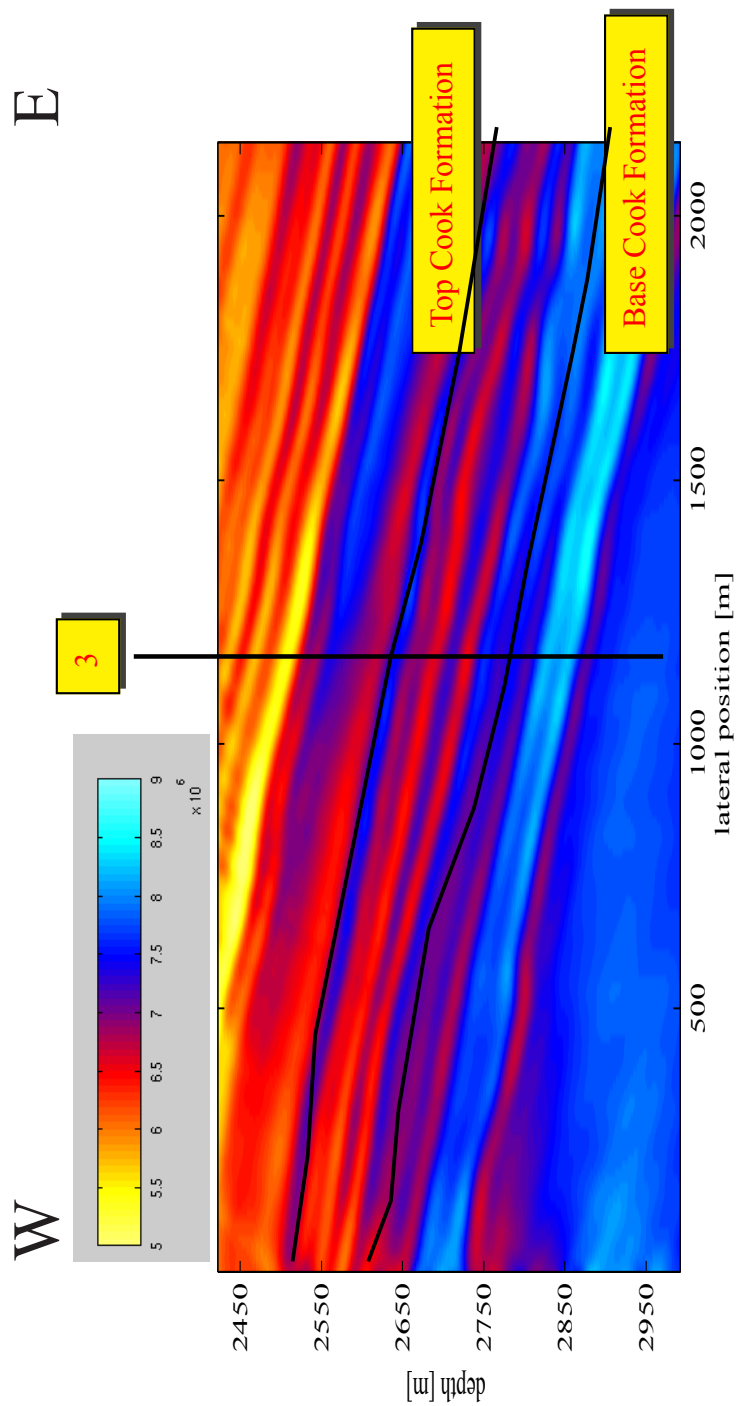
Figure 5.17: Scenario I: simulated constrained sparse-spike impedance image. The solid lines indicate the base and top of the Cook Formation in the migrated real data, respectively. The inclined internal reflectors are not simulated. Impedance values are in $[kg\,/(s\,m^2)]$.
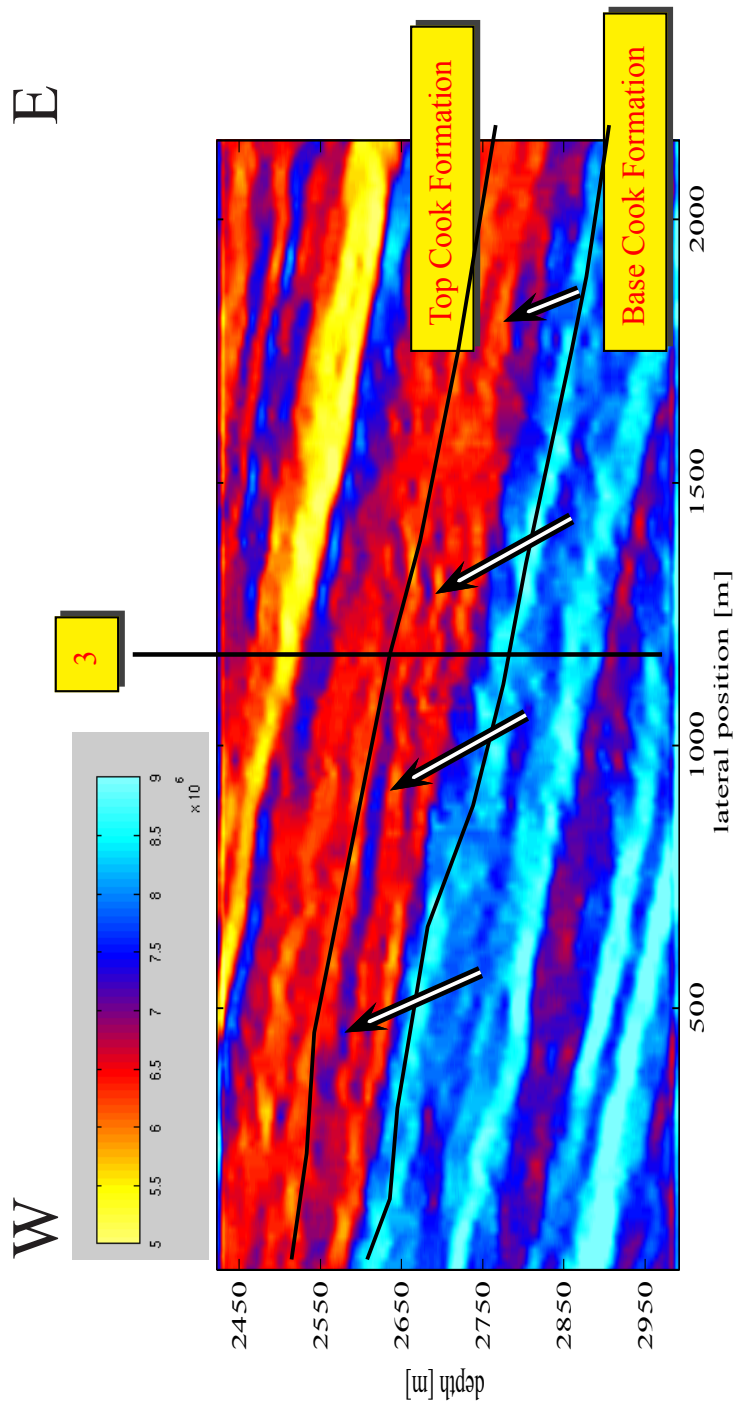
Figure 5.18: Corresponding constrained sparse-spike real impedance image of the migrated real data shown in Figure 5.2. The solid lines indicate the base and top of the Cook Formation, respectively. The arrows indicate the inclined internal reflectors that are subject to the iterative shared-earth modeling study presented in this chapter. Impedance values are in $[kg/(s\,m^2)]$].

■ 5.5.2   Geological scenario II: east-west migrating channels and tidal sand-bars

The second scenario recreates the inclined internal reflectors by geologically modeling east-west migrating channels and tidal sand-bars in an estuarine environment. The tidal sand-bars are constrained by size and shape data of modern day analogues in the Gironde and Western-Scheldt Estuaries (Tables 5.1 and 5.2). A schematic illustration of an earth model with channels and bars is shown in Figure 5.19. The same spatial resolution and approximated angle filters are used to simulate migrated and impedance data.

In the first earth model (denoted by scenario II (A)) the tidal-sand bar height is 15 m. This resembles the analogue data of the Gironde Estuary (Table 5.1). The averaged dip on the channel side is -3° (Table 5.2). In the migrated real image, four inclined internal reflectors are interpreted (Figure 5.2). These reflectors are probably associated with the lateral growth of a tidal sand-bars in the adjacent channel. Therefore, in the earth-model four tidal sand-bars are created. The impedance model is shown in Figure 5.20. The accompanying simulated prestack depth-migrated image shows that this does recreate the inclined internal reflectors (Figure 5.21). Also in the simulated constrained sparse-spike impedance image no expressions of the inclined internal reflectors are found (Figure 5.22).

In the next modeling effort (denoted by scenario II (B)), the tidal-bar height is increased to 30 m. This resembles the analogue data of the Western-Scheldt Estuary (Table 5.2). The dip of the tidal-sand bar is again -3°, but three instead of four growth phases are modeled. The impedance model is shown in Figure 5.23. The simulated prestack depth-migrated image seems to recreate the inclined internal reflectors reasonable well (Figure 5.24). This seismic interpretation is further supported by the simulated constrained sparse-spike impedance image, which show low-impedance zones that are also present in the constrained sparse-spike impedance real image (Figures 5.18 and 5.25).

The observations in the simulated migrated and impedance data lead to the conclusion that the east-west migrating channels and tidal sand-bars in an estuarine environment represent an earth model that fits the migrated and inverted real seismic data best.
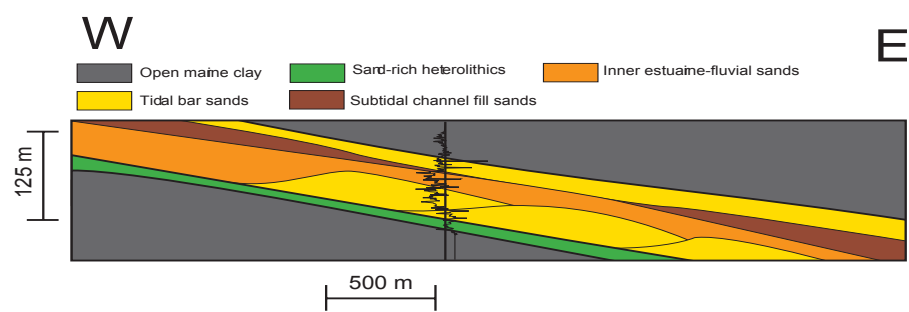
Figure 5.19: Scenario II: schematic illustration of east-west migrating channels and tidal sand-bars and the gamma-ray log of well 3.
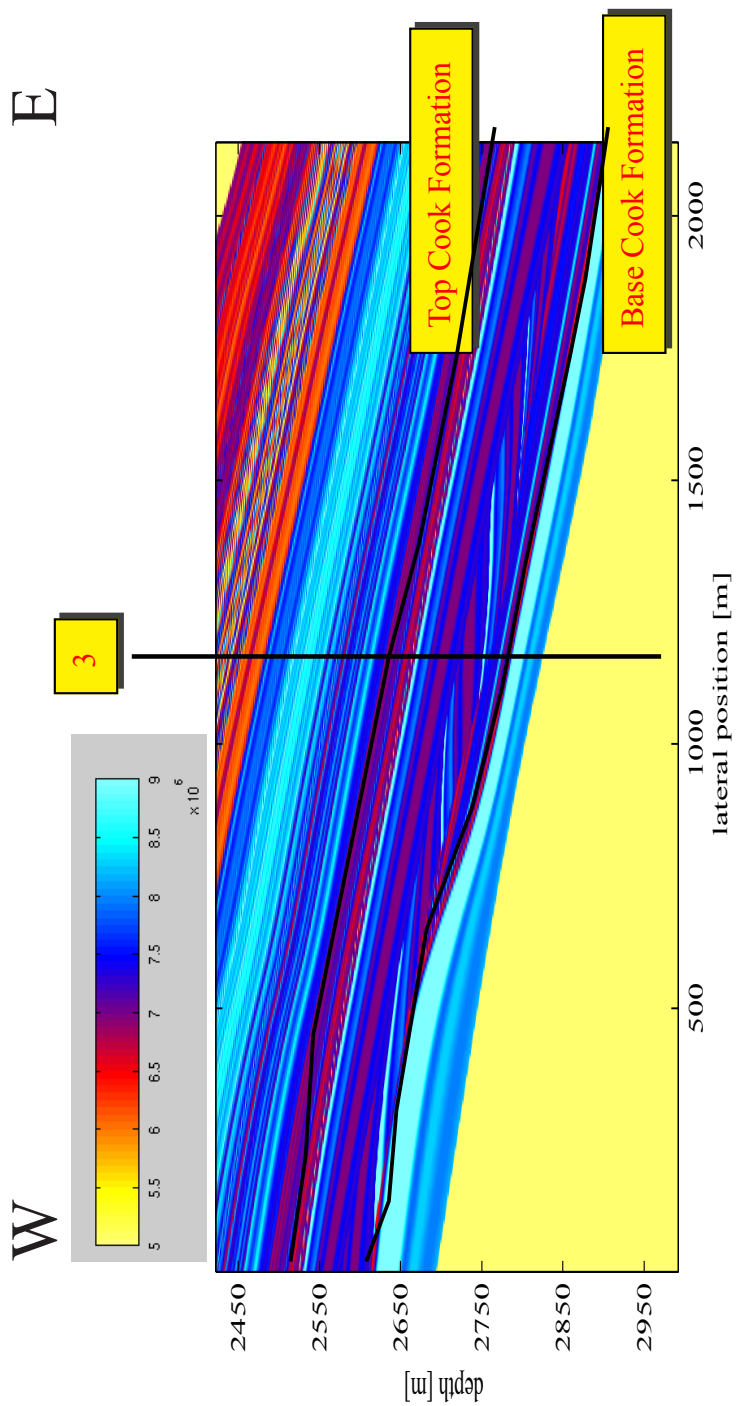
Figure 5.20: Scenario II (A): impedance model. The longitudinal bars are approximately 15 m in height. The solid lines indicate the base and top of the Cook Formation in the migrated real data, respectively. Impedance values are in [kg /(s m²)].
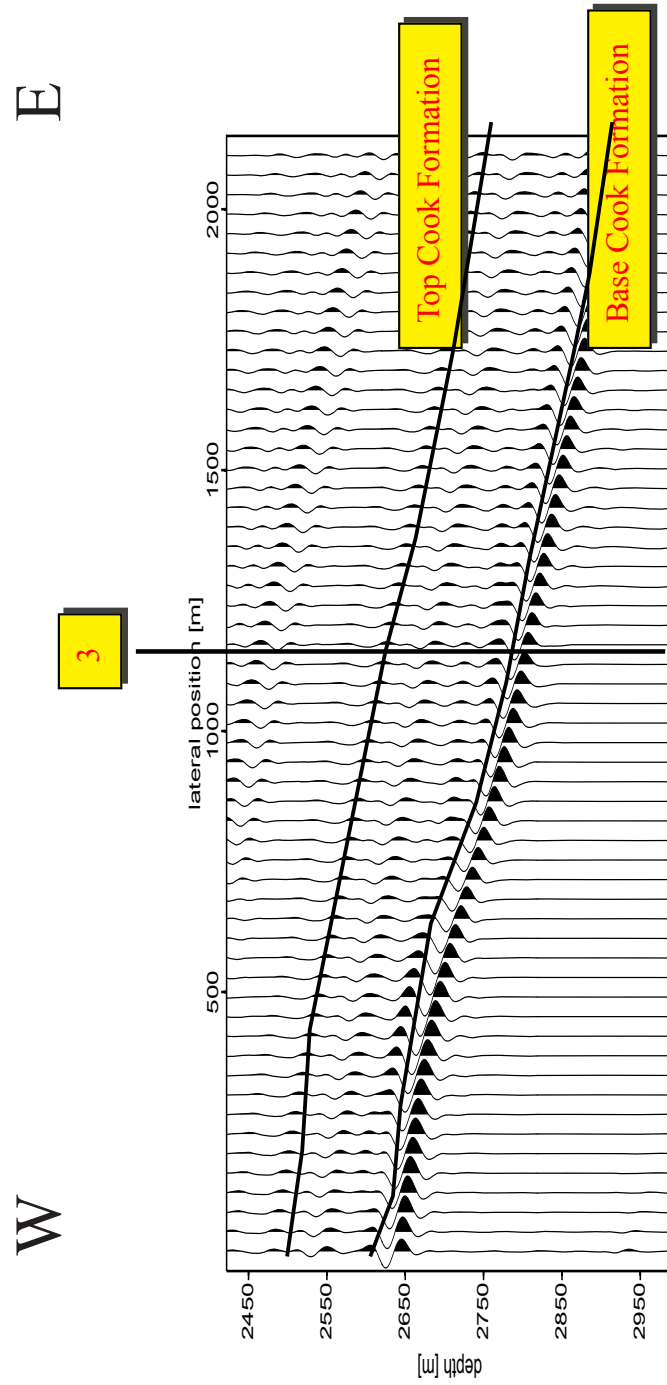
Figure 5.21: Scenario II (A): simulated prestack depth-migrated image plotted using AGC. The solid lines indicate the base and top of the Cook Formation in the migrated real data, respectively.
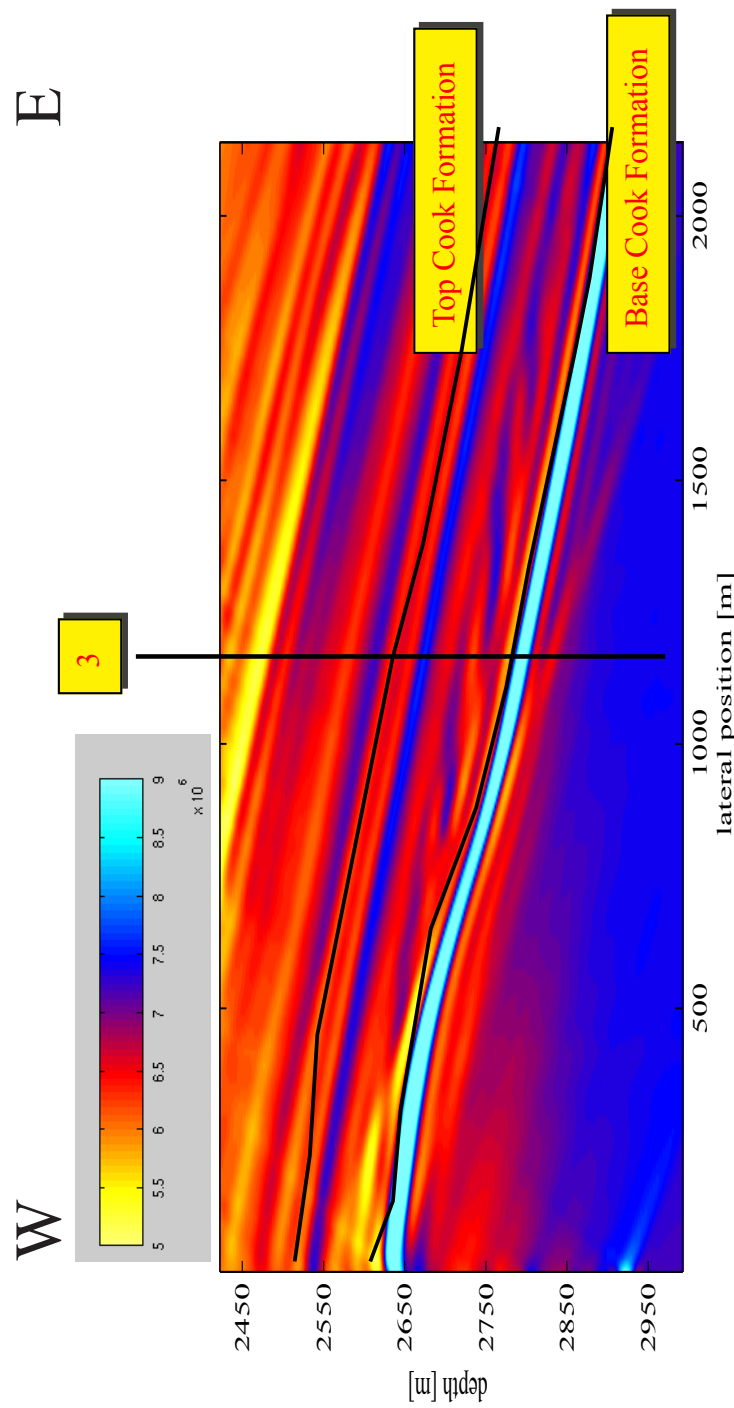
Figure 5.22: Scenario II (A): simulated constrained sparse-spike impedance image. The solid lines indicate the base and top of the Cook Formation in the migrated real data, respectively. Impedance values are in [kg /(s m²)].
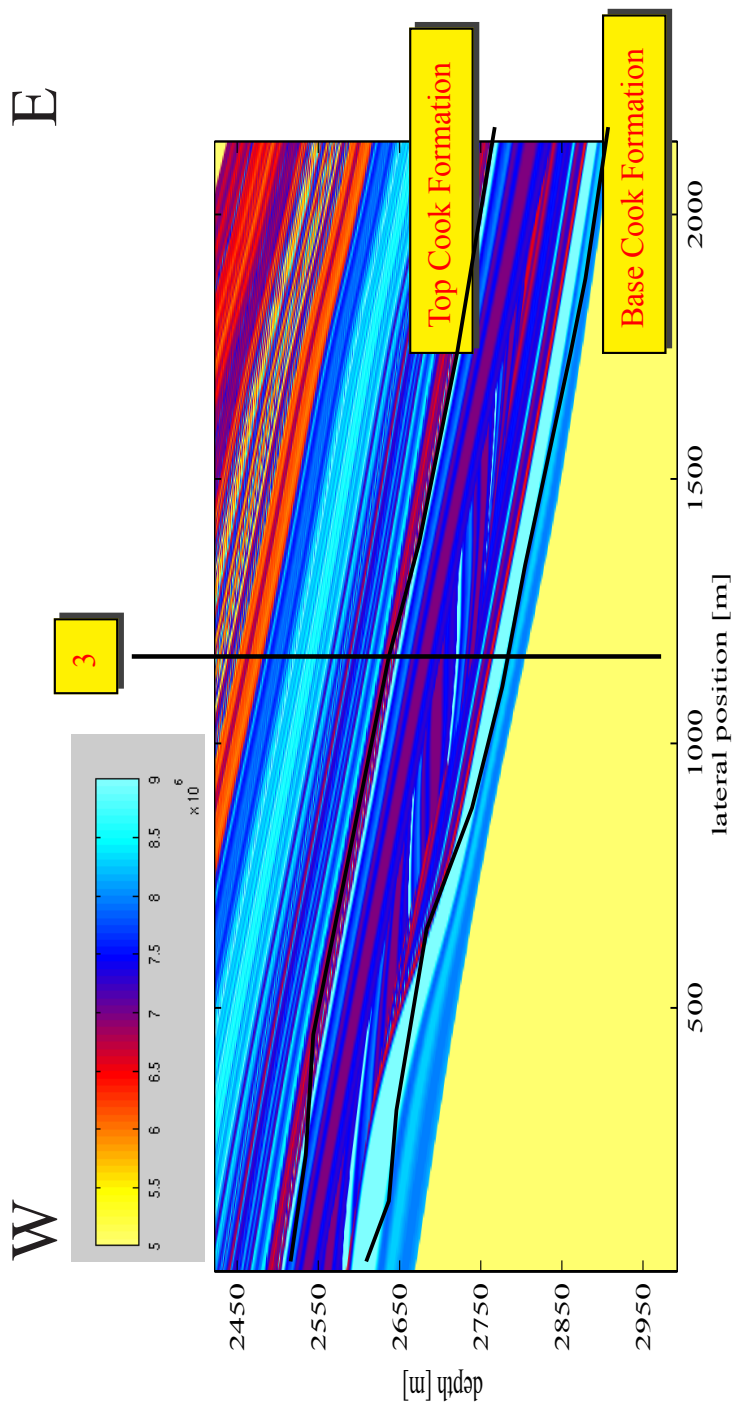
Figure 5.23: Scenario II (B): impedance model. The longitudinal bars are approximately 30 m in height. The solid lines indicate the base and top of the Cook Formation in the migrated real data, respectively. Impedance values are in [kg /(s m²)].
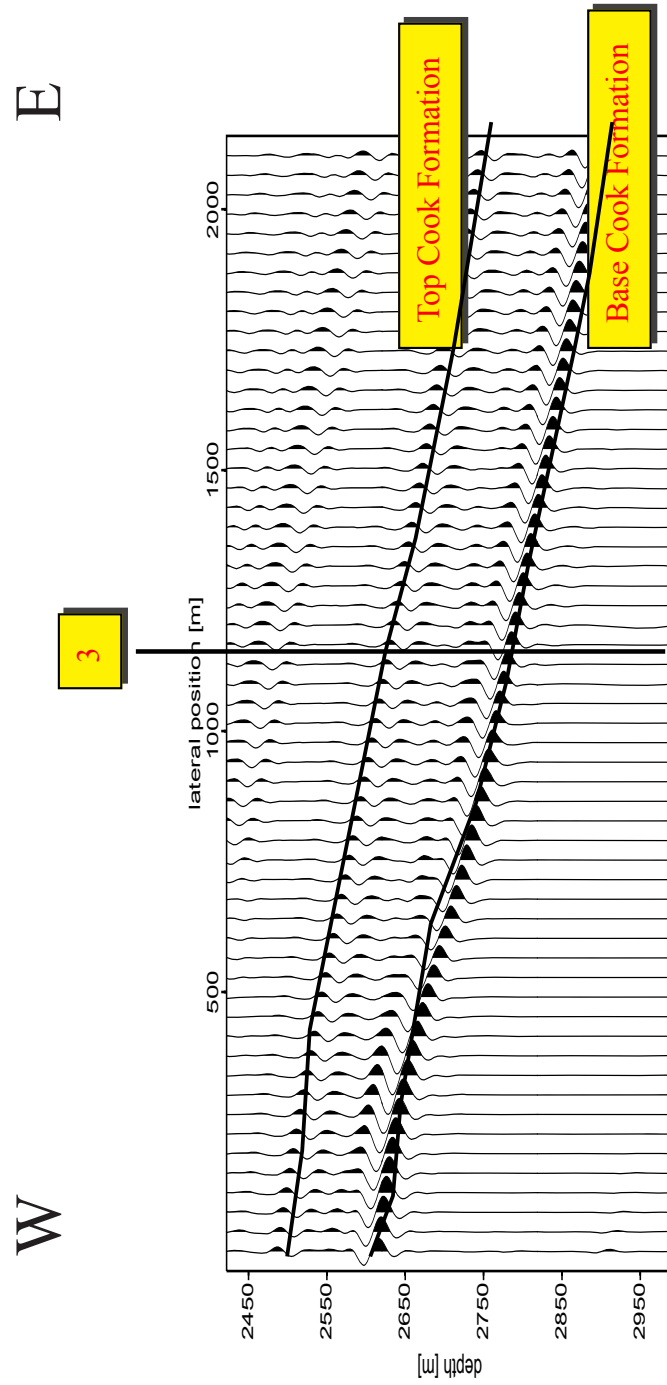
Figure 5.24: Scenario II (B): simulated prestack depth-migrated image plotted using AGC. The solid lines indicate the base and top of the Cook Formation in the migrated real data, respectively.
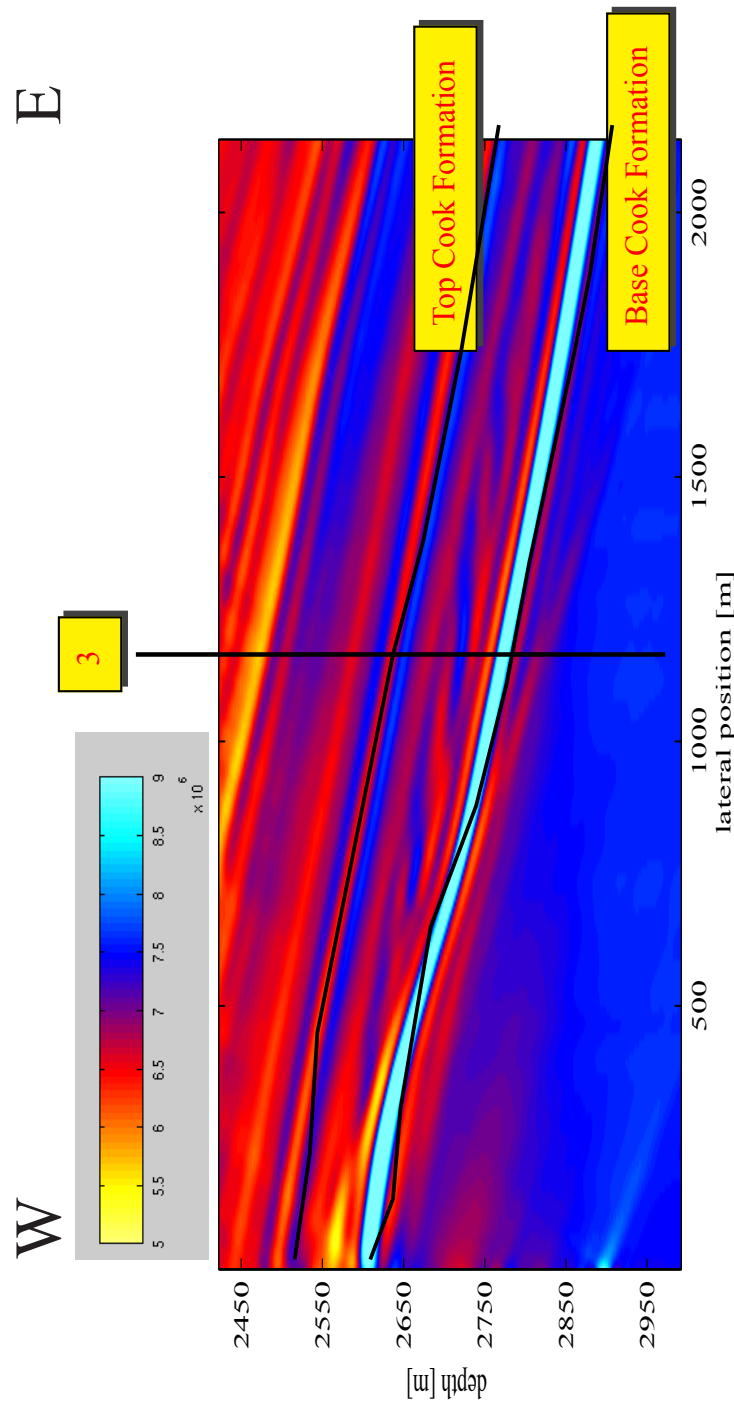
Figure 5.25: Scenario II (B): simulated constrained sparse-spike impedance image. The solid lines indicate the base and top of the Cook Formation in the migrated real data, respectively. Impedance values are in [kg /(s m²)].
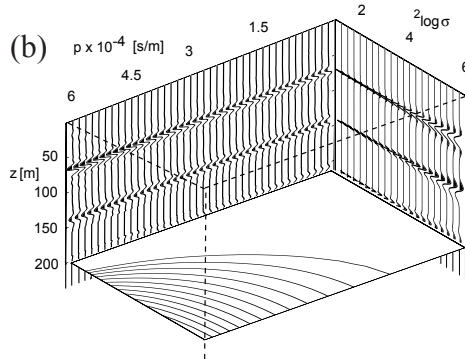
(a) Fingerprint of the author's left forefinger. (b) Response of a plane wave response in the scale (σ) τ, depth domain. The multi-angle multi-scale characterization of a plane wave response is interpreted as the fingerprint of the reflector [Wapenaar et al., 2005].

Originally the Federal Bureau of Investigation (FBI) adopted the discrete wavelet transform to compress images of fingerprints before they were stored in their database. More recently, the wavelet transform is used to extract distinct and local characteristics from fingerprint images to construct an automatic fingerprint identification and recognition system [Lee et al., 2002] (Figure (a)).

The wavelet transform is used in a similar seismic application, the goal of the following chapter is to link an earth model with (simulated) inverted data, making use of fingerprints (Figure (b)).

6

Linking an earth model with inverted seismic data using the wavelet transform

In a shared-earth model different measurement techniques, sensitive to different properties of the Earth's subsurface, are used to analyze a hydrocarbon reservoir body in terms of, e.g., internal heterogeneities and facies distribution. Integration of the different data types is hampered by two factors. Firstly, the measurements are carried out at different scales and secondly, they have different spatial coverages (Figure 1.1). For example, seismic data have a typical depth resolution of 25 m and an earth model has a typical depth resolution of 15 cm, which makes matching of geological boundaries that appear as reflection events in seismic data and changes in the earth model a nontrivial task. It is the aim of this chapter to show that the wavelet transform can be used as a link between an earth model and (simulated) constrained sparse-spike inverted seismic data through a so-called multi-scale analysis. The focus is on the application to link wire-line and constrained sparse-spike inverted seismic data of the Cook Formation of the Oseberg Field (offshore

Norway).

6.1   Introduction to the multi-scale analysis

This section provides a brief description of the multi-scale analysis, a tool based on the wavelet transform for analyzing the scaling properties of local variations in a signal, as introduced by Mallat and Hwang [1992]. Herrmann [1997] was the first to apply this as a seismic attribute. When applied to, e.g., wire-line data, the strength of outliers appear to vary at an approximately constant rate when they are observed as a function of scale (σ).
The continuous wavelet-transform of a signal $c(z)$ is defined as

$$\check{c}(\sigma, z) = \frac{1}{|\sigma|^\mu} \int_{-\infty}^{\infty} c(z')\psi\left(\frac{z'-z}{\sigma}\right) dz', \qquad (6.1)$$

where $\psi(z)$ is the analyzing wavelet, which is chosen real-valued, and σ is the scale parameter, with μ a normalization term. For the moment $\mu = 1$ and $\psi(z)$ is minus the second derivative of the Gaussian (a Ricker wavelet, Figure 3.1). In the next section the proper choice for each parameter for linking a wire-line log with an inverted seismic image is derived.
A function $f(t)$ with three isolated singular points, can be described as: $|t|^{-0.4}$ (top), a step function (middle) and $|t|^{0.2}$ (bottom) (Figure 6.1 (a)). For a discrete set of σ values, the wavelet transform of the function is computed (Figure 6.1 (b)). It has to be noted that the horizontal axis of the scale is logarithmically spaced.
Figure 6.1 (c) shows the position of the so-called modulus-maxima lines, the lines that interconnect the local maxima in neighboring traces. The different values of gray of Figure 6.1 (c) represent the amplitudes of the wavelet transform in Figure 6.1 (b). Figure 6.1 (c) is known as the wavelet transform modulus-maxima line analysis (WTMML). The rate of change (α) of the amplitudes along the modulus-maxima lines may be seen as the fingerprint of the outliers (we refer also to [Wapenaar et al., 2005] and the introduction to this chapter). Next, the amplitudes along the modulus-maxima lines in Figure 6.1 (c) are extracted and plotted in a double-logarithmic scale in Figure 6.1 (d) to (f). These graphs are known as amplitude-versus-scale (AVS) curves. Measuring the slopes along the corresponding AVS-curves gives
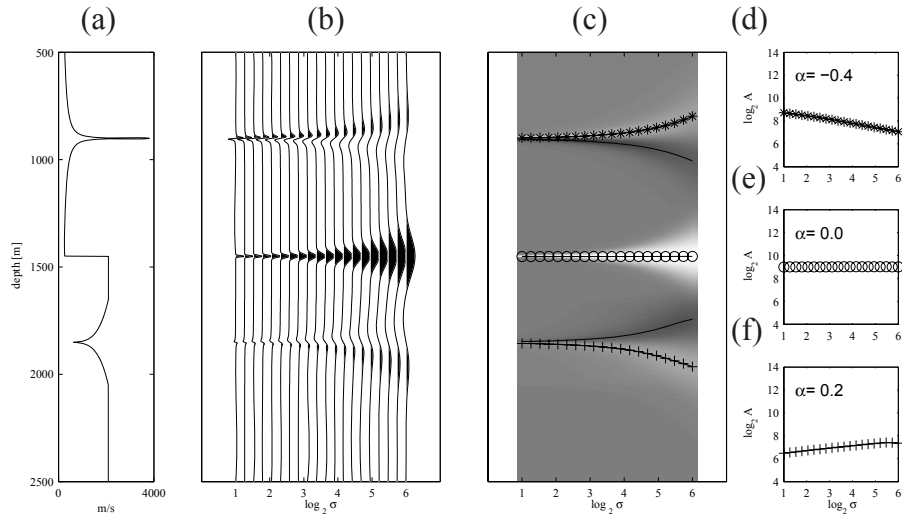
Figure 6.1: (a) The function $f(t)$ with three isolated singular points, respectively described by shifted versions of $|t|^\alpha$ with α = -0.4, 0 and 0.2. (b) Continuous wavelet transform of the signal in figure (a). (c) Wavelet transformed modulus-maxima lines (WTMML), obtained from figure (b). (d) to (f) Amplitude-versus-scale (AVS) curves, measured along the selected modulus-maxima lines in figure (c). The slopes α = -0.4, 0 and 0.2, of the lines correspond to the singularity exponents of the signal in figure (a).

α = -0.4, 0 and 0.2, respectively, which correspond to the exponents in the local description of the singularities in $f(t)$.

The previously outlined procedure is known as multi-scale analysis and can be used to link different data by comparing their fingerprints (α values). Ghose and Goudswaard [2004] showed how shallow S-wave seismic data and cone penetration test data are linked using multi-scale analysis. More recently, the multi-scale analysis is applied by Smythe et al. [2004] to interpret and track stratigraphic boundaries in migrated seismic data. Although a multi-scale analysis on wire-line data is part of their study, a solid mathematical basis to properly compare the fingerprint from inverted seismic data and wire-line data is missing. This link is derived in the next section.

6.2 Linking an earth model and inverted seismic data

The geological model can be described by the impedance function $I(x, y, z)$ and the (simulated) migrated data by $m(x, y, z)$. Their wavelet transforms (analogous to equation (6.1)) are,

$$\check{I}(\sigma, x, y, z) = \frac{1}{|\sigma|^{\mu_1}} \int_{-\infty}^{\infty} I(x, y, z')\psi_1\left(\frac{z' - z}{\sigma}\right) dz', \qquad (6.2)$$

and

$$\check{m}(\sigma, x, y, z) = \frac{1}{|\sigma|^{\mu_2}} \int_{-\infty}^{\infty} m(x, y, z')\psi_2\left(\frac{z' - z}{\sigma}\right) dz', \qquad (6.3)$$

where x, y are parameters and $\psi_1(z)$ and μ_1 may be different from $\psi_2(z)$ and μ_2. In deriving a relation between $\check{m}$ and $\check{I}$, the framework to simulate prestack depth-migrated data is used (Chapter 2). A (simulated) prestack depth-migrated seismic image $m(x, y, z)$ is described by a multidimensional spatial convolution between the reflectivity of the earth model $r(x, y, z)$ and a spatial resolution filter $s(x, y, z)$,

$$m(x, y, z) = s(x, y, z) * r(x, y, z). \qquad (6.4)$$

For the wavelet-transformed migrated data we may write,

$$\check{m}(\sigma, x, y, z) = s(x, y, z) * \check{r}(\sigma, x, y, z), \qquad (6.5)$$

where

$$\check{r}(\sigma, x, y, z) = \frac{1}{|\sigma|^{\mu_2}} \int_{-\infty}^{\infty} r(x, y, z')\psi_2\left(\frac{z' - z}{\sigma}\right) dz'. \qquad (6.6)$$

Next the reflectivity function $r(x, y, z)$ is approximated by,

$$r(x, y, z) \approx \frac{1}{2\bar{I}} \frac{\partial I(x, y, z)}{\partial z}, \qquad (6.7)$$

where $\bar{I}$ is an averaged (possibly smoothly varying) version of the impedance function $I(x, y, z)$. Substitution into equation (6.5) and applying integration by, parts yields

$$\check{r}(\sigma, x, y, z) \approx -\frac{1}{2\bar{I}} \frac{\sigma^{-1}}{|\sigma|^{\mu_2}} \int_{-\infty}^{\infty} I(x, y, z')\psi_2'\left(\frac{z' - z}{\sigma}\right) dz', \qquad (6.8)$$

where $\psi_2'(z) = \frac{\partial \psi_2(z)}{\partial z}$. When we choose

$$\psi_2'(z) = -\psi_1(z) \text{ and } \mu_2 = \mu_1 - 1, \tag{6.9}$$

and compare the results for positive σ with equation (6.2), we find,

$$\check{r}(\sigma, x, y, z) \approx \frac{\check{I}(\sigma, x, y, z)}{2\bar{I}}, \tag{6.10}$$

or, using equation (6.5),

$$\check{m}(\sigma, x, y, z) \approx s(x, y, z) * \frac{\check{I}(\sigma, x, y, z)}{2\bar{I}}. \tag{6.11}$$

Hence, if we make the choices for the wavelets and exponents according to equation (6.9), it follows from equation (6.10) that the wavelet transform of the (simulated) prestack depth-migrated data are approximately proportional to the wavelet transform of the earth model (in terms of the impedance) convolved with the spatial resolution filter. When the spatial resolution filter is derived for a seismic wavelet that has a constant spectrum in the seismic frequency band, it thus follows that the AVS behavior along the WTMML of the (simulated) inverted seismic data should be approximately equal to that of the earth model.

6.3   Application to the Cook Formation

With the aid of the multi-scale analysis (Section 6.1) together with the properly derived input parameters of Section 6.2, the goal is to link the slope of AVS curves (α's), which are computed of wire-line and constrained sparse-spike inverted seismic data of the Cook Formation, to each other.
This is first done by performing a multi-scale analysis of the wire-line logs. The multi-scale analysis is guided by a detailed sedimentary analysis. The multi-scale analysis is used to derive a α-characterization of the base, the inclined internal reflectors and the top of the Cook Formation. These results are also used to enhance and support a north-south and a west-east correlation panel of the different wells.
Secondly, before the constrained sparse-spike inverted real data are used in the multi-scale analysis, a sensitivity study is performed with the goal to

understand the influence of phase errors introduced by a constrained sparse-spike algorithm on the seismic data on the slope of an AVS curve.

Finally, based on the multi-scale wire-line analysis and the sensitivity analysis, two α ranges are tracked in the 3D constrained sparse-spike inverted seismic data by performing the multi-scale analysis on a trace-by-trace basis. The two attribute maps are interpreted geologically using the results of the sensitivity analysis, detailed sedimentary analysis and an independent 3D seismic interpretation study which focuses on internal boundaries of the Cook Formation.

■ 6.3.1 Multi-scale analysis of wire-line data

Input to the multi-scale analysis is the impedance log of each well (i.e, the P-wave velocity log multiplied with the rock-density log). The impedance log is high-frequency filtered and re-sampled from 15 cm to 1 m, to match the depth sampling of the constrained sparse-spike inverted seismic data of the Cook Formation. The multi-scale analysis starts with *well 3*. The impedance log of the Cook Formation interval is shown in Figure 6.2 (a). In the wavelet transform $\psi_1(z)$ is chosen as a Ricker wavelet and $\mu_1 = 1$, according to equation (6.2). The wavelet-transformed impedance log is shown in Figure 6.2 (b) for a range of $\log_2\sigma = 1$ to $\log_2\sigma = 6$. Table 6.1 is used as a lookup table to select possible modulus-maxima lines which belong to the Cook Formation.

For the base of the Cook Formation at 2759 m a modulus-maxima line is found which is indicated by "+" signs in Figure 6.2 (c). In the corresponding AVS graph, the slope reads $\alpha = 0$ (Figure 6.2 (f)). The slope is measured in this scale range, because at a sampling rate of 1 m this scale range roughly corresponds to the seismic-scale range [Wapenaar et al., 2005]. At a depth of 2678 m a modulus-maxima line for the top of the Cook Formation is found, which is indicated by "*" signs in Figure 6.2 (c). The corresponding AVS curve shows that the modulus-maxima line exists up to $\log_2\sigma = 3$, because only in the $\log_2\sigma = 4$ to $\log_2\sigma = 6$ scale range, wire-line and seismic data can be properly compared; α is indicated with Not a Number (NaN).

An internal boundary of the Cook Formation interval is identified at a depth of 2703 m. The corresponding modulus-maxima line, which is indicated by "o" signs, has a slope of 0 (Figure 6.2 (e)).

The previous outlined procedure is repeated for *well 5*, from east to west, where the base of the Cook Formation is characterized by a modulus-maxima line which in the AVS graph has a slope of -0.6 (Figure 6.3 (e)). At a depth of 3177 m a modulus-maxima line belonging either to the top or an internal boundary is found, which is characterized by α=-0.9 (Figure 6.3 (d)). A multi-scale analysis of *well 4* shows similar AVS graphs as the result of well 3: the base, an internal boundary and the top of the Cook Formation are characterized by $\alpha = $ NaN, -0.3 and 0, respectively (Figure 6.4 (d) to (f)).

From north to south, the AVS graphs of *well 1* characterize the base by α=0.1, an internal boundary by α=-0.2 and the top by α=NaN (Figure 6.5 (d) to (f)).

Finally in *well 2*, the base, an internal boundary and the top of the Cook Formation are characterized by $\alpha = $ NaN, -0.3, and -0.5, respectively (Figures 6.6 (d) to (f)). All results are also listed next to the result of the sedimentary analysis such that the depths and α characterization can be compared in the following discussion (Table 6.1).

Geological discussion on the results of the multi-scale analysis

Base of the Cook Formation

The depths found in the multi-scale analysis correspond very well with the results of the sedimentary analysis (Table 6.1). The base is characterized by $\alpha = 0$ in wells 3, 1 and 4. The α characterization is only based on the slope between $\log_2\sigma$=4 and $\log_2\sigma$=6, whereas comparing different wire-line AVS-graphs can be done over the whole scale range.

Similar shaped AVS-curves are found in wells 3 and 1 (Figures 6.2 (f) and 6.5 (f)). The shape of the AVS-curves in wells 5 and 4 similar in the scale range up to $\log_2\sigma$=3, then a different slope is found (Figures 6.3 (e) and 6.4 (f)). It is concluded that all four AVS graphs characterize the base of the Cook Formation, the variation in the shape of the curve found in the AVS graphs of well 4 and 5 are most likely explained by the fact that both wells are located near the edge of the estuarine environment (Figure 5.8). The shape found in the AVS graph of well 2, greatly differs from the other wells, possibly indicating that the base of the Cook Formation is eroded (Figure 6.6 (f)).

Top of the Cook Formation

A clear α characterization for the top of Cook Formation is only found in well 2, around the depth indicated by the sedimentary analysis. Because the shape and the α characterization of the AVS graph of well 5 at a depth of 3177 m is quite similar, it is considered the top of the Cook Formation. In all other wells, only up to $\log_2\sigma = 4$ a modulus-maxima line exists. These AVS graphs cannot be linked in a logical way, which is perhaps explained by the geological setting of the Cook Formation, which originates from a relative sea level rise. The smooth transition from the Cook to the Drake Formations is difficult to detect with a multi-scale analysis, which characterizes the sharpness of a transition. The base of the Cook Formation originates from a relative sea level fall, which created a sharp sequence boundary that is clearly detected by the multi-scale analysis.

The sequence boundary at the base of Cook-3

The sequence boundary at the base of Cook-3 is not characterized by a α value that exists up to the seismic range. Also in the other logs, the base of Cook-3 could not be characterized. This conclusion is based on the depth information derived in the sedimentary study.

Instead other modulus-maxima lines that exist up to the seismic scale range are selected, it shows that a strong correlation in the α value is found. This could indicate an internal boundary of the Cook Formation. However, this does not seems not to be in agreement with the results of the sedimentary analysis. A possible geological explanation is that the selected modulus-maxima lines are related to occurrences of isolated nodules of carbonate cement. These are found in the Cook-3 cores (Fig. 6.7 (a)). These produce a sharp increase of the density log (Fig. 6.7 (b)) that can explain the modulus-maxima lines. Unfortunately, this cannot be checked, because the wells are only partly cored.

Well	Sedimentary study	Multi-scale analysis		Multi-scale analysis at 8°		
		Base of the Cook Formation				
1	2588	2591	0.1			
2	2486	2481	NaN			
3	2761	2759	0	2755 2755 2752	0 0 0.5	
4	2496	2491	0			
5	3181	3184	-0.6			
		Top of the Cook Formation				
1	2514	2507	NaN			
2	2426	2431	-0.5			
3	2684	2678	NaN	2660 2660 2670	NaN NaN NaN	
4	2405	2415	NaN			
5	3161	3177	-0.9			
		Internal sequence boundary				
1	2575	2522	-0.2			
2		2447	-0.3			
3	2726	2703	0	2700 2700 2712	-0.2 -0.2 NaN	
4	2483	2448	-0.3			

Table 6.1: Overview per well at which depth in meters subsea, the base, internal boundary and top of the Cook Formation are interpreted. The table further shows the result of the multi-scale analysis and the sensitive analysis performed for well 3. NaN indicates that the α characterization could not be performed in the seismic-scale range.
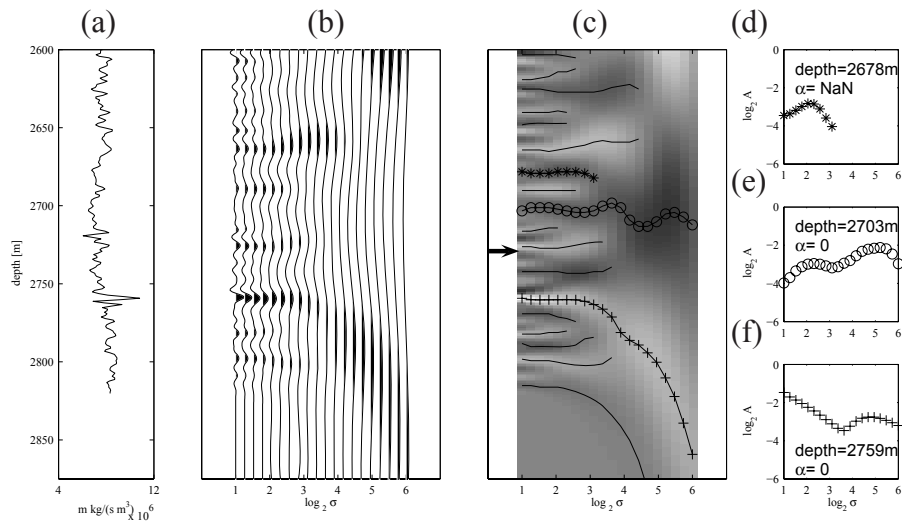
Figure 6.2: Multi-scale analysis. (a) Impedance log of well 3. (b) Continuous wavelet transform of the impedance log. (c) Wavelet transform modulus-maxima lines (WTMMLS), obtained from (b). (d) to (f) Amplitude-versus-scale (AVS) curves, measured along the selected modulus-maxima lines in (c). The arrow indicates the modulus-maxima line at the depth of the base of the Cook-3 as interpreted in the sedimentary study.
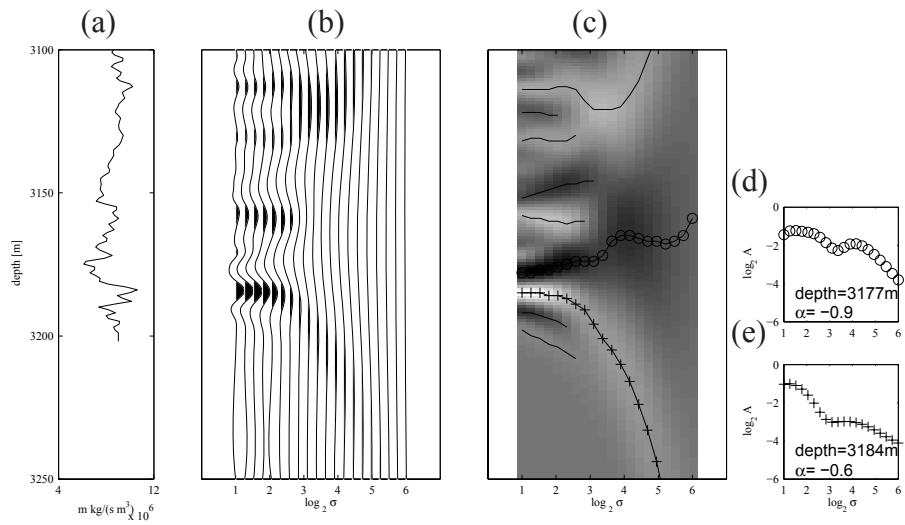
Figure 6.3: Multi-scale analysis. (a) Impedance log of well 5. (b) Continuous wavelet transform of the impedance log. (c) Wavelet transform modulus-maxima lines (WTMMLS), obtained from (b). (d) to (e) Amplitude-versus-scale (AVS) curves, measured along the selected modulus-maxima lines in (c).
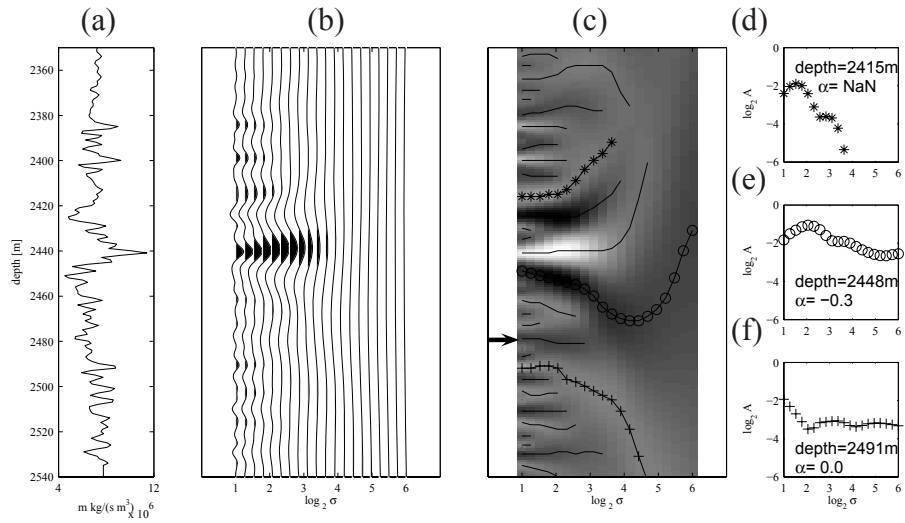
Figure 6.4: Multi-scale analysis. (a) Impedance log of well 4. (b) Continuous wavelet transform of the impedance log. (c) Wavelet transform modulus-maxima lines (WTMMLS), obtained from (b). (d) to (f) Amplitude-versus-scale (AVS) curves, measured along the selected modulus-maxima lines in (c). The arrow indicates the modulus-maxima line at the depth of the base of the Cook-3 as interpreted in the sedimentary study.

Figure 6.5: Multi-scale analysis. (a) Impedance log of well 1. (b) Continuous wavelet transform of the impedance log. (c) Wavelet transform modulus-maxima lines (WTMMLS), obtained from (b). (d) to (f) Amplitude-versus-scale (AVS) curves, measured along the selected modulus-maxima lines in (c). The arrow indicates the modulus-maxima line at the depth of the base of the Cook-3 as interpreted in the sedimentary study.
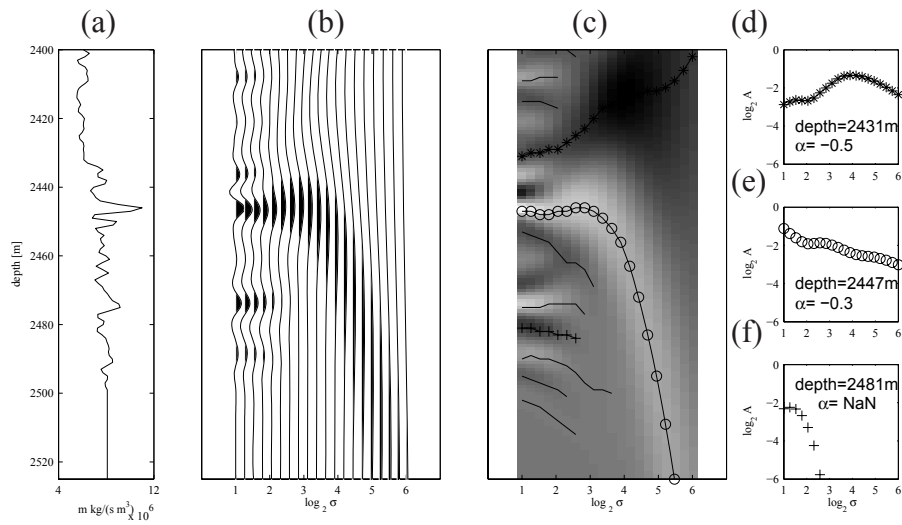
Figure 6.6: Multi-scale analysis. (a) Impedance log of well 2. (b) Continuous wavelet transform of the impedance log. (c) Wavelet transform modulus-maxima lines (WTMMLS), obtained from (b). (d) to (f) Amplitude-versus-scale (AVS) curves, measured along the selected modulus-maxima lines in (c).

Figure 6.7: (a) A cored section of well 4-S, showing the Cook-3 consisting of a cemented sandstone interval (indicated by 3). (b) Corresponding density log (depth scale in cm), at the location of the arrows a sharp increase of the density is found that correlate to the cemented interval.

■ **6.3.2   Sensitivity study of the multi-scale analysis**

Before the real constrained sparse-spike inverted seismic data are used in a multi-scale analysis, a sensitivity study is conducted. The main question is how the multi-scale analysis, and in particular the α characterization of a modulus-maxima line, is influenced by uncertainties in the input data. This is important because tracking of a sequence boundary in the real constrained sparse-spike inverted seismic data are based on selecting a value of α. The quality of the output data after running a constrained sparse-spike inversion algorithm depends on the estimate of the inversion wavelet and the steepness of geological dips, as discussed in Chapter 4 and Section 5.3. In the following sensitivity study the discussion is restricted to these two parameters. Other problems, e.g., errors introduced by the time-to-depth conversion of the real constrained sparse-spike inverted seismic data based on only the velocity log of well 3, are not considered.

Are constrained sparse-spike inverted seismic data a proper input for a multi-scale analysis ?

In order to answer this question, the Cook interval of well 3 is used to construct three dip-panels (Section 5.4), dipping at $8°$, $22°$ and $45°$. The $8°$ dip-panel approximates the geological dip of the Cook Formation (Section 5.1). Constrained sparse-spike inverted seismic data are simulated using the approximated angle filter, as shown in Figure 6.8. This filter is constrained by the same processing parameters as discussed in Section 5.2.1. The suppression of particular dips is directly related to the maximum angles of wave propagation. However, in this case we are interested how the amplitude are effected if the wavelet stretch is not correctly handled instead if a particular reflector is imaged or not. Therefore the total opening-angle is chosen to be $120°$ ($\varphi_1 = 60°$ and $\varphi_2 = -60°$). After adding low-frequency information to the local 1D approximated angle filtered dip-panels, one reflectivity trace of each dip-panel is used as input to a multi-scale analysis. Input to the wavelet transform are $\psi_2(z)$, i.e. the first derivative of the Gaussian, and $\mu_2 = 0$, in order to compare the computed α values directly to the previous multi-scale analysis results of the impedance log (equation (6.9)).

The AVS graphs of the multi-scale analysis of the $8°$ reflectivity trace and

the multi-scale analysis of the impedance log (Figures 6.9 (d) to (f) with Figures 6.2 (d) to (f)) show the following two differences. Firstly, the depths at which the three sequence boundaries are found differ slightly. Secondly, although the shape in the AVS graphs is comparable, the values of α differ slightly. Since α is computed by fitting a straight line from $\log_2 \sigma = 4$ to $\log_2 \sigma = 6$, a slight difference in one of the two points in the AVS graph has a large impact on the value of α (highlighted by the dashed circle in Figure 6.9 (e)).

The multi-scale analysis of the $22°$ dip-panel (Figure 6.10) shows that the base of the Cook Formation is not detected. Increasing the geological dip to $45°$ (Figure 6.11), the constrained sparse-spike inverted seismic data produces errors too large to correctly perform a multi-scale analysis. Instead of using a constrained sparse-spike algorithm, an alternative such as a migration-deconvolution algorithm should be used to properly invert the seismic data as input for a multi-scale analysis.

What is the influence of a wrongly estimated inversion wavelet on the multi-scale analysis ?

In order to answer this question, a $8°$ dip-panel based on well 3 is filtered by two different approximated angle filters which simulate the effect of a wrongly estimated inversion wavelet. These approximated angle filters are created through trace-by-trace inversion of two different spatial resolution filters with an input wavelet of $5°$ and $20°$ respectively with a zero-phase inversion wavelet (Figures 6.12 (a) and (b)).

After adding the low-frequency information to each of the filtered dip-panels, one reflectivity is selected and used in a multi-scale analysis. Figure 6.13 shows the result for the $5°$ phase error. By comparison of this result with Figure 6.9 it is concluded that the values of α and the depths are comparable.

The results of the $20°$ phase error show that, e.g., the base of the Cook Formation is found at the correct depth, but that the value of α is much larger value (Figure 6.14). The internal sequence boundary is in this case not detectable.

In conclusion, constrained sparse-spike inverted seismic data for geological dips up to $\sim 15°$, even with an inversion wavelet that is not properly match-
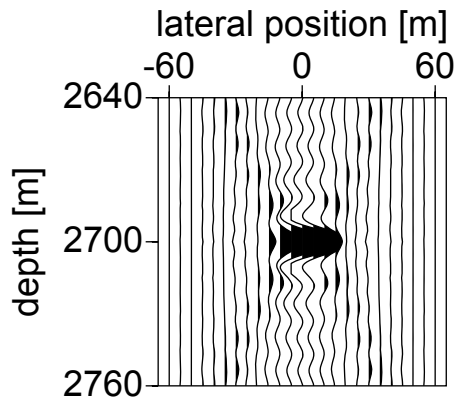
Figure 6.8: A local 1D approximated angle filter.

ing the data, are still suitable as input to multi-scale analysis. In order to track a particular geological boundary a small range of α values should be selected. Because the multi-scale analysis is performed on a trace-by-trace basis on the 3D data, not at every lateral position a particular boundary is detected in the multi-scale analysis.

The previous sensitivity analysis can also be used as an application to guide the seismic inversion process itself. The wire-line information provides valuable a-priori knowledge on the value of α. If this information is not coherent in the inverted seismic data, the inversion parameters should be adapted with a sensitivity analysis guiding the process.
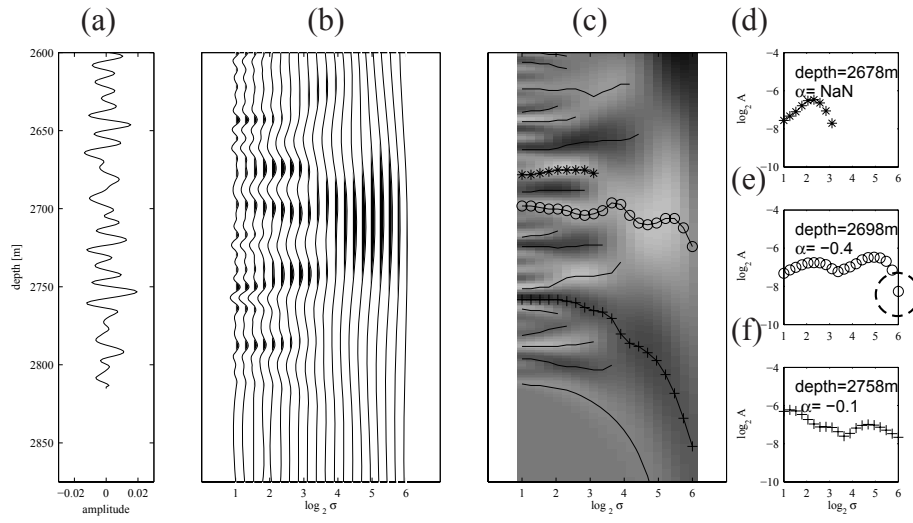
Figure 6.9: Multi-scale analysis performed on $8°$ dip-panel filtered by the approximated angle filter shown in Figure 6.8. (a) One reflectivity trace of the dip-panel. (b) Continuous wavelet transform of the impedance function in (a). (c) Wavelet transform modulus-maxima lines (WTMMLS), obtained from (b). (d) to (f) Amplitude-versus-scale (AVS) curves, measured along the selected modulus-maxima lines in (c). The dashed circle highlight that the α value is sensitive to small errors because of the linear fit that is performed to compute it.
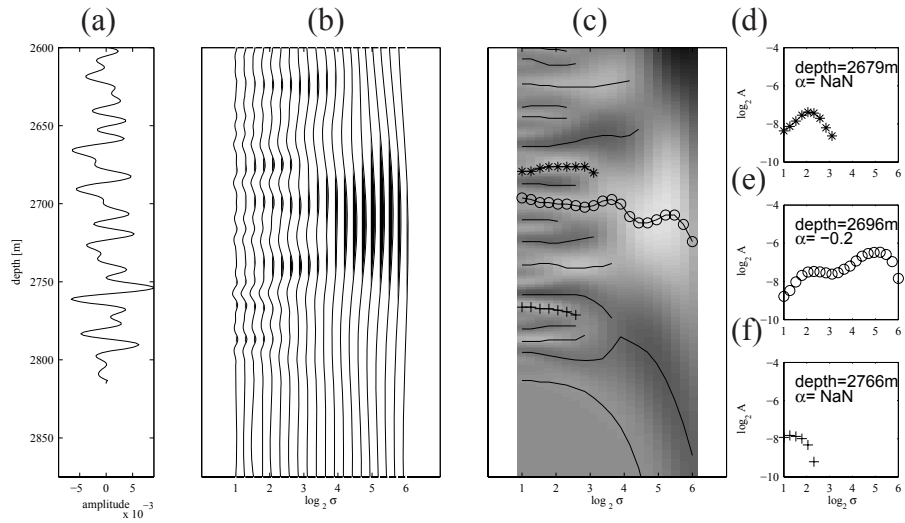
Figure 6.10: Multi-scale analysis performed on $22°$ dip-panel filtered by the approximated angle filter shown in Figure 6.8. (a) One reflectivity trace of the dip-panel. (b) Continuous wavelet transform of the impedance function in (a). (c) Wavelet transform modulus-maxima lines (WTMMLS), obtained from (b). (d) to (f) Amplitude-versus-scale (AVS) curves, measured along the selected modulus-maxima lines in (c).
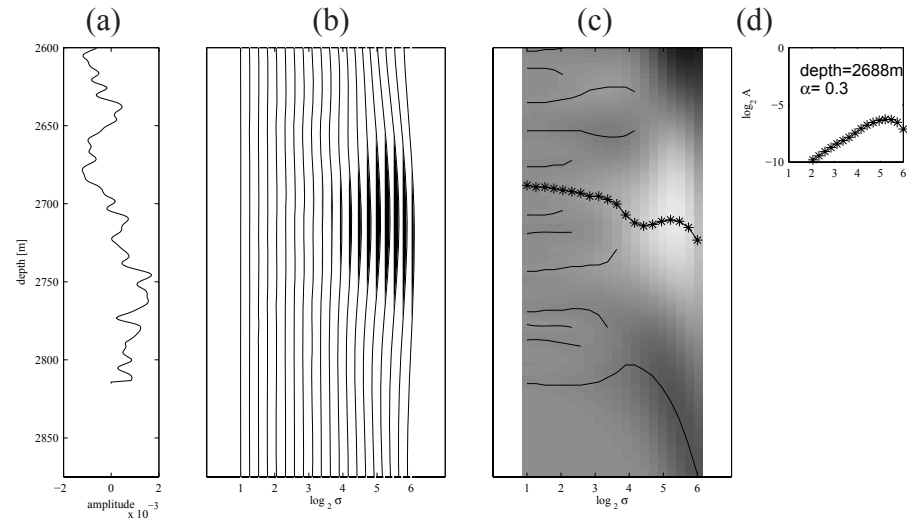
Figure 6.11: Multi-scale analysis performed on $45°$ dip-panel filtered by the approximated angle filter shown in Figure 6.8. (a) One reflectivity trace of the dip-panel. (b) Continuous wavelet transform of the impedance function in (a). (c) Wavelet transform modulus-maxima lines (WTMMLS), obtained from (b). (d) Amplitude-versus-scale (AVS) curve, measured along the selected modulus-maxima lines in (c).
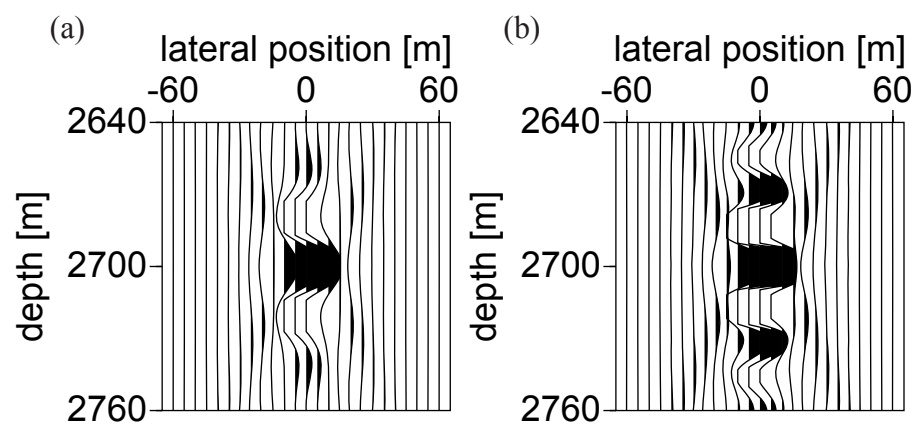
Figure 6.12: (a) An approximated angle filter obtained after inverting a spatial resolution filter with a $5°$ rotated wavelet by a zero-phased inversion wavelet. (b) An approximated angle filter obtain after inverting the spatial resolution filter with a $20°$ rotated wavelet by a zero-phase inversion wavelet.
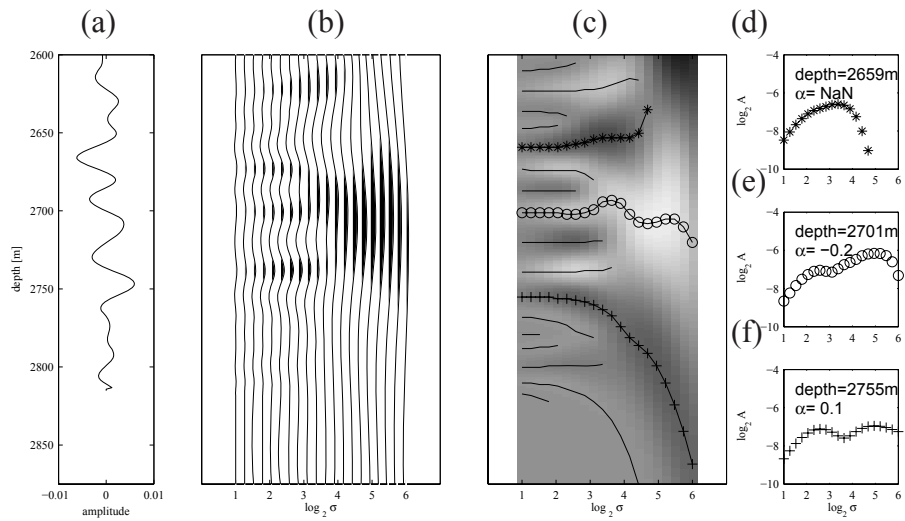
Figure 6.13: Multi-scale analysis performed on 8° dip-panel filtered by the 1D angle shown in Figure 6.12 (a). (a) One reflectivity trace of the dip-panel. (b) Continuous wavelet transform of the impedance function in (a). (c) Wavelet transform modulus-maxima lines (WTMMLS), obtained from (b). (d) to (f) Amplitude-versus-scale (AVS) curves, measured along the selected modulus-maxima lines in (c).
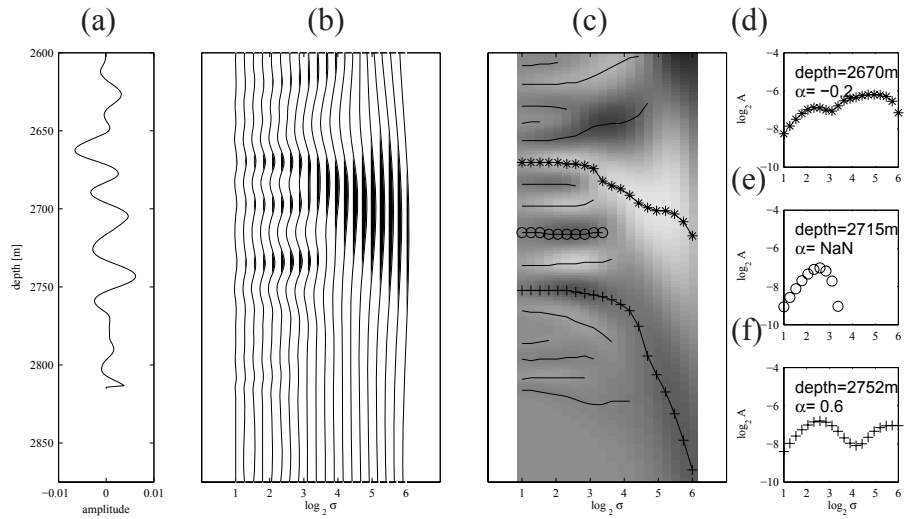
Figure 6.14: Multi-scale analysis performed on 8° dip-panel filtered by the 1D angle shown in Figure 6.12 (b). (a) One reflectivity trace of the dip-panel. (b) Continuous wavelet transform of the impedance function in (a). (c) Wavelet transform modulus-maxima lines (WTMMLS), obtained from (b). (d) to (f) Amplitude-versus-scale (AVS) curves, measured along the selected modulus-maxima lines in (c).

■ 6.3.3   Multi-scale analysis of constrained sparse-spike inverted seismic data

The multi-scale analysis on the real constrained sparse-spike inverted seismic data starts with a discussion of the multi-scale analysis results of two traces of a west-east image which is crossing well 3 (Figure 5.1).

A reflectivity trace 50 m west of the actual well location is input to the wavelet transform (Figure 6.15 (a)). The wavelet transform uses $\psi_2(z)$, i.e. the first derivative of the Gaussian, and $\mu_2 = 0$. Using the depths in Table 6.1, modulus-maxima lines for the base, an internal boundary and top of the Cook Formation are selected. Figures 6.15 (d) to (f) show the accompanying AVS graphs, respectively.

Only in the range from $\log_2 \sigma = 4$ to $\log_2 \sigma = 6$ the multi-scale analysis of the constrained sparse-spike inverted and wire-line data can be compared. Therefore, the top of the Cook Formation cannot be detected, which was also concluded for the multi-scale analysis of the impedance log at well 3. The modulus-maxima line at a depth of 2764 m and characterized by $\alpha = 0$ is linked to the base of the Cook Formation. However, closer inspection of the AVS graphs of Figures 6.2 (f) and 6.15 (f) shows that in the range from $\log_2 \sigma = 4$ to $\log_2 \sigma = 6$ the shape of the AVS curves differ. The internal boundary that is characterized by $\alpha = 0$ at a depth of 2730 m, is located at the proper depth according to the sedimentary study.

A second reflectivity trace is located at 103 m to the west of well 3. Due to the geological dip of approximately $8°$, the depths listed in Table 6.1 are expected to be shallower here. The AVS graph (Figure 6.16 (f)), which could belong to the base of the Cook Formation, is located too deep and the value of α is not within a small range of α values obtained from the sensitivity analysis (Table 6.1). Furthermore it is also difficult to correlate the other two AVS graphs. This underlines the conclusion of the sensitivity analysis that gaps may show up in the multi-scale analysis, even if the geological boundary is expected to be continuous.

Attribute map of the base of the Cook Formation

On a trace-by-trace basis the 3D constrained sparse-spike inverted seismic data are used in a multi-scale analysis. In order to track the base of the Cook

Formation, an α range from $\alpha > $ -0.5 to $\alpha < 0.1$ is selected. The α range is based on the multi-scale analysis of the wire-line data and sensitivity analysis (Table 6.1). The value of α at well 5 is not taken into account, because the inverted seismic data do not extend to this lateral position.

In Figure 6.17, each depth where the multi-scale analysis has found a value of α which is within the selected α range, is marked with a "+" sign on the migrated seismic data. Furthermore, the solid lines in Figure 6.17 indicate the base and the top of the Cook Formation. Especially in the west, the result of the multi-scale analysis lines up well with the base of the Cook Formation. The dashed circle indicates the base of the Cook Formation, and the solid circle indicates an internal reflector. As discussed earlier, due to the fact that the value of α of both sequence boundaries are similar (or very close to each other), it is impossible to distinguish the two from each other. This problem is solved by selecting a depth range for the value of α. For the base of the Cook Formation, only 50 m above and below the seismic interpretation base (shown by the solid line) the value of α used to construct an attribute map of the 3D data are shown (Figure 6.18). Around well 2, the base is hardly detected, as is highlighted by the circle. If time-to-depth errors are excluded as a cause, this may support the previously discussed idea that around well 3 the base of the Cook Formation is eroded.

Finally, compare the result of the multi-scale analysis to Figure 6.19 that shows an enlarged version of Figure 5.8. There is not a clear correlation between the two attribute maps. As discussed in Section 5.1.4, geologically interpreting this seismic attribute is not straightforward. However, the attribute map that is based on the multi-scale analysis can be correlated directly to the wire-line data.

Attribute map of the inclined internal reflectors of the Cook Formation

The inclined internal reflectors of the Cook Formation are tracked using the following α value range: $0 \leq \alpha < 1$. In the east and near the well 3 the + markers line up well with the inclined internal reflectors which are studied in the previous chapter (highlighted by the arrows in Figure 6.20). Near well 3 only a part of an angular discontinuity is tracked that is indicated by the box in Figure 6.20, and further to the west no inclined internal reflectors are found.

In order to track the inclined internal reflectors in the 3D multi-scale data, a depth window 50 m above the base and below top of the Cook is used, otherwise also the base of the Cook Formation is tracked (illustrated by the two circles in Figure 6.20). The resulting attribute map is shown in Figure 6.21. In order to interpret this attribute map, it is compared to an independent attribute map created from a 3D seismic interpretation study which focused on the inclined internal reflectors (Figure 6.22). It is noted that because an auto tracker and interpolation step are used in order to perform the seismic interpretation, the shapes are more smoothed than the multi-scale attribute map. The shape obtained from the multi-scale analysis matches very well with the shape found by the seismic interpretation study. Only in the south the multi-scale analysis does not show the interpreted inclined internal reflectors. Different causes can be considered, e.g., the influence of the time-to-depth conversion, which is only based on well 3 or a different geological facies. If the first cause is considered, also the interpretations of the base of the Cook Formation need to be updated. Based on the shape, sizes and distribution, the inclined internal reflectors are interpreted as tidal sand-bars [Thomassen et al., 2006].

Based on the comparison between the two attribute maps, the initial seismic interpretation of the inclined internal reflectors (highlighted by the arrows) is reconsidered. West of well 3, neither in the multi-scale analysis nor in the 3D interpretation study they could be found. The only conclusion may be that seismic events are not created by geological layers, but is a result of, e.g., multiple scattering or seismic imaging errors. Obviously, this also has to be studied with a sensitivity analysis. The framework to simulate prestack depth-migrated and constrained sparse-spike inverted seismic data does not include simulation of multiples (see also discussion in Section 2.5).

The multi-scale analysis, and in particular the attribute map is a powerful attribute, because unlike most other attributes, it can be interpreted geologically using the a-priori and independent analysis of the wire-line data. If in this way also multiple energy could be discriminated between true reflections, the value of the multi-scale analysis and corresponding attribute map can further be increased.
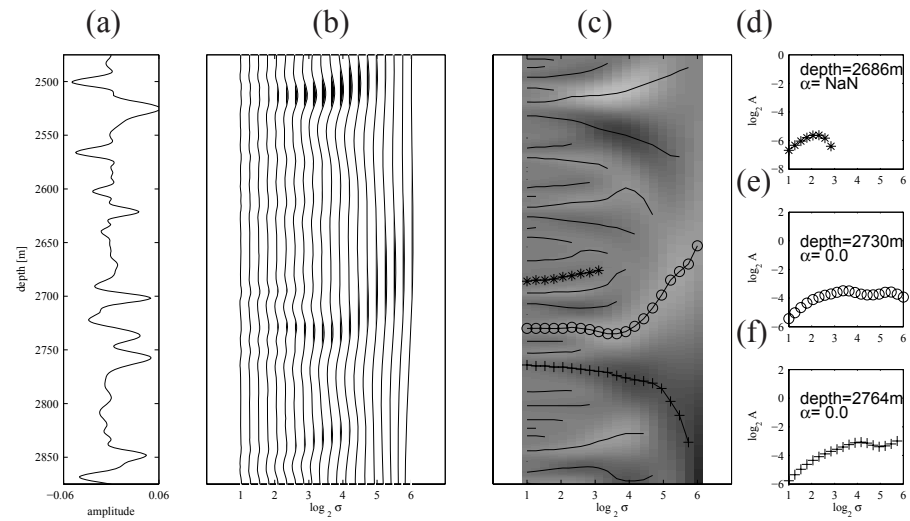
Figure 6.15: Multi-scale analysis on the constrained sparse-spike inverted data. (a) reflectivity trace located 50 m to the west of well 3. (b) Continuous wavelet transform of the impedance function in (a). (c) Wavelet transform modulus-maxima lines (WTMMLS), obtained from (b). (d) to (f) Amplitude-versus-scale (AVS) curves, measured along the selected modulus-maxima lines in (c).
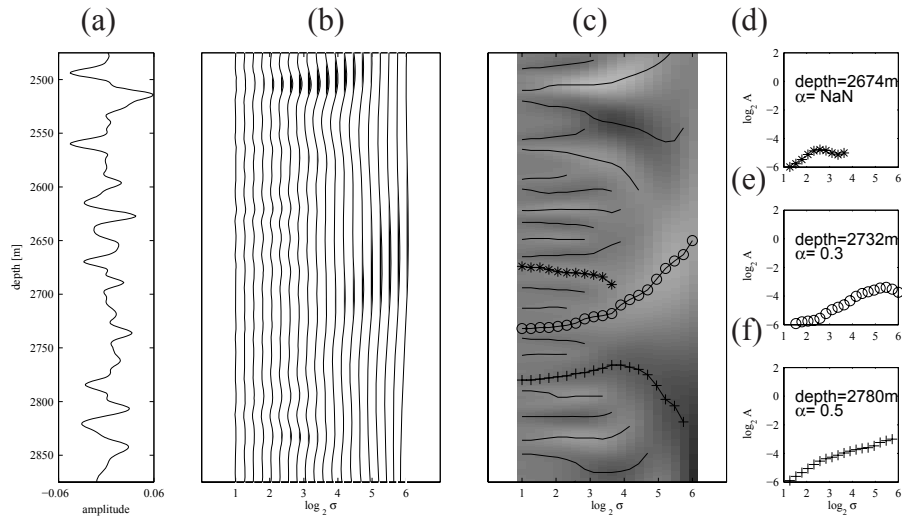
Figure 6.16: Multi-scale analysis on the constrained sparse-spike inverted data. (a) reflectivity trace located 100 m to the west of well 3. (b) Continuous wavelet transform of the impedance function in (a). (c) Wavelet transform modulus-maxima lines (WTMMLS), obtained from (b). (d) to (f) Amplitude-versus-scale (AVS) curves, measured along the selected modulus-maxima lines in (c).
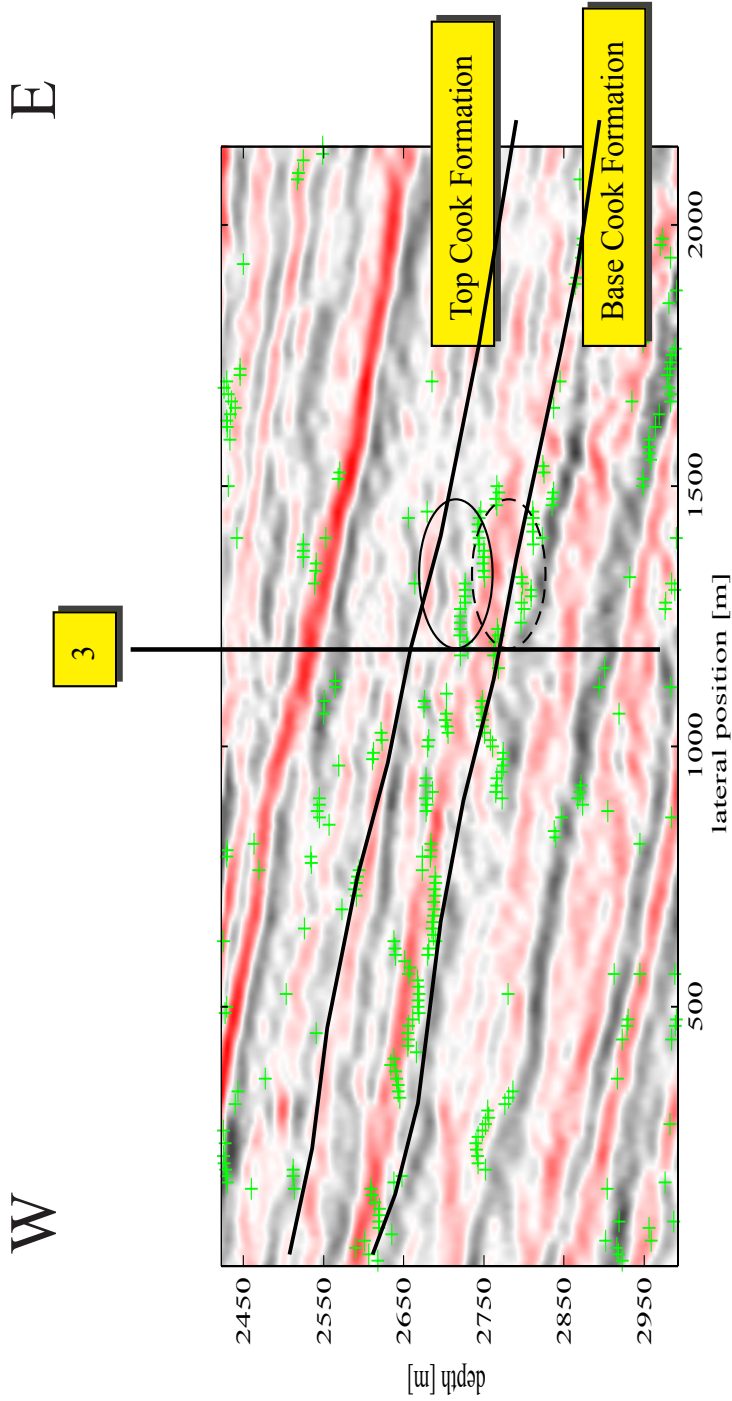
Figure 6.17: West-east migrated seismic image, crossing well 3. The result of a trace-by-trace multi-scale analysis for a range of α values from > -0.5 to < 0.1 (indicated by "+" signs) to track the base of the Cook Formation. The solid lines represent the base and top of the Cook Formation as interpreted from the 3D seismic data. The dashed circle indicates the base and the solid circle indicates an internal sequence boundary of the Cook Fm., respectively. Both are found with the same by α range.
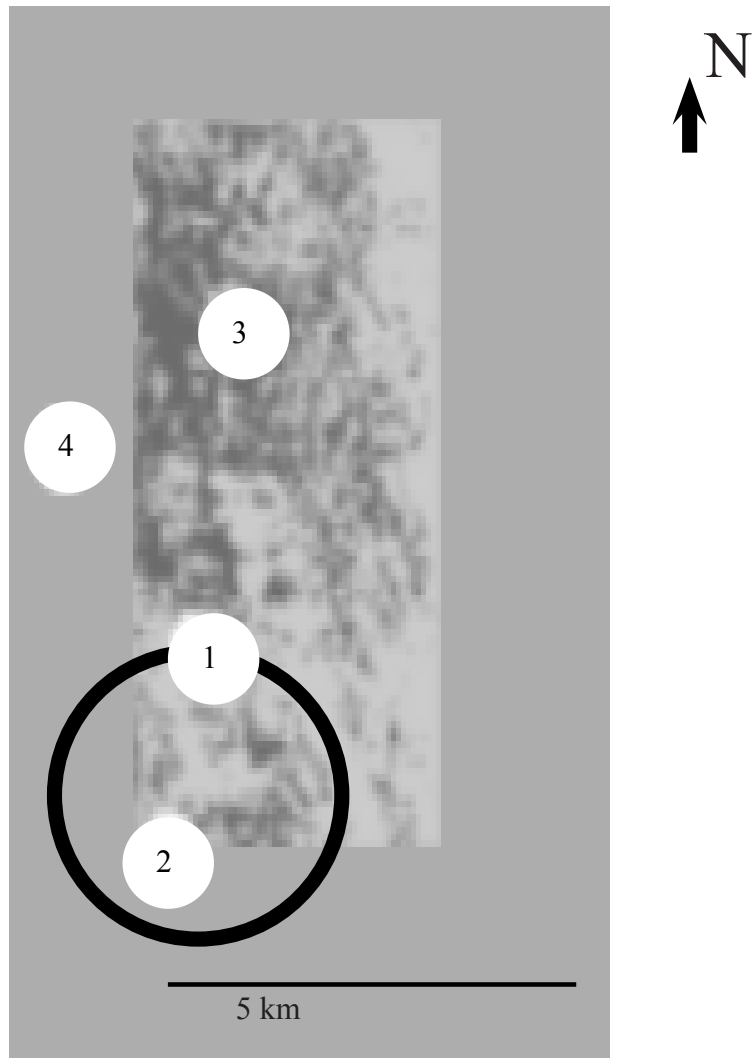
Figure 6.18: Attribute map showing the shape of the base of the Cook Formation based on the multi-scale analysis, shown together with the well locations. The circled area indicates possible erosion of the base of the Cook Formation.
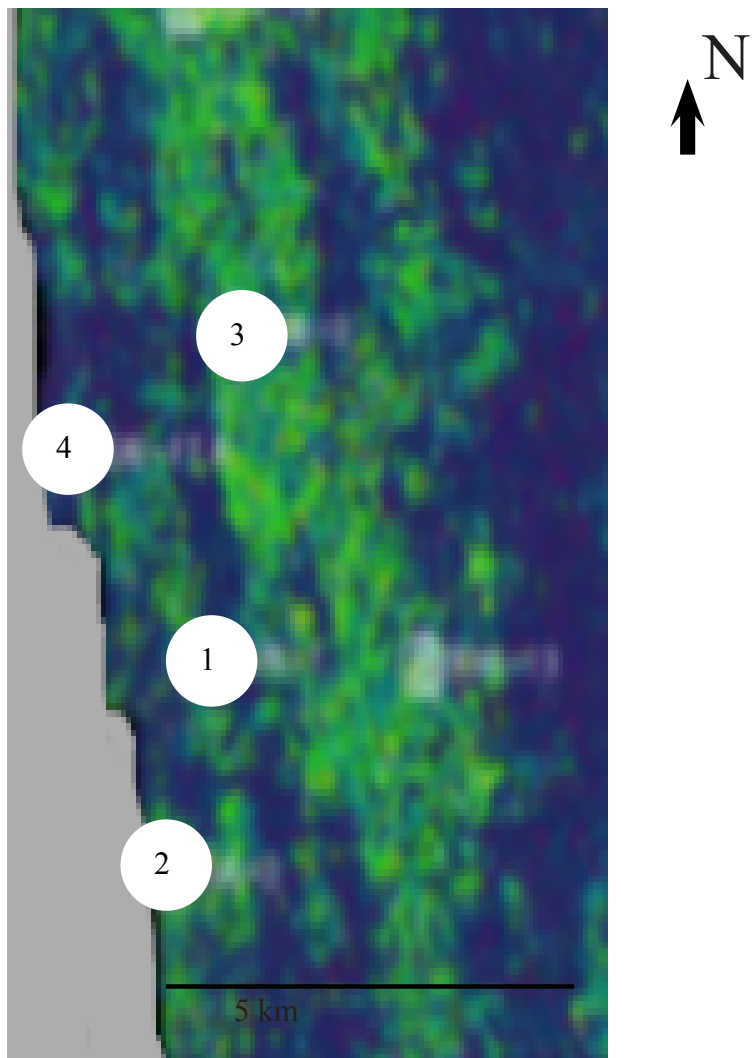
Figure 6.19: Seismic attribute map, showing taking the cosine of the phase around a small interval of the base of the Cook Formation. The image is an enlarged version of Figure 5.8.
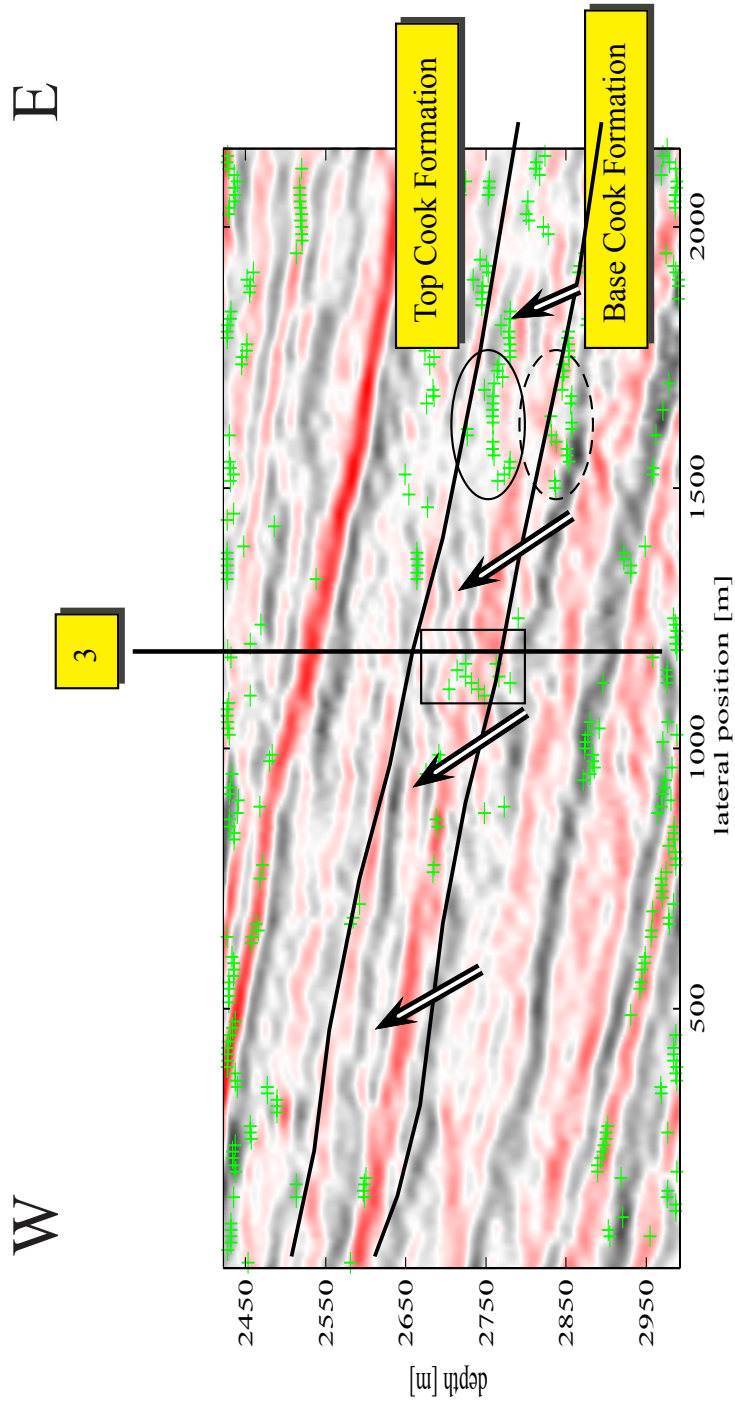
Figure 6.20: West-east migrated seismic image, crossing well 3. The results of a trace-by-trace multi-scale analysis for a range of α values (indicated by "+" signs) from $\alpha >= 0.1$ to $\alpha < 1$ to track an internal interface of the Cook Formation. The solid lines represent the base and top of the Cook Formation as interpreted from the 3D seismic data. The arrows indicate the inclined internal reflectors studied in the previous chapter.
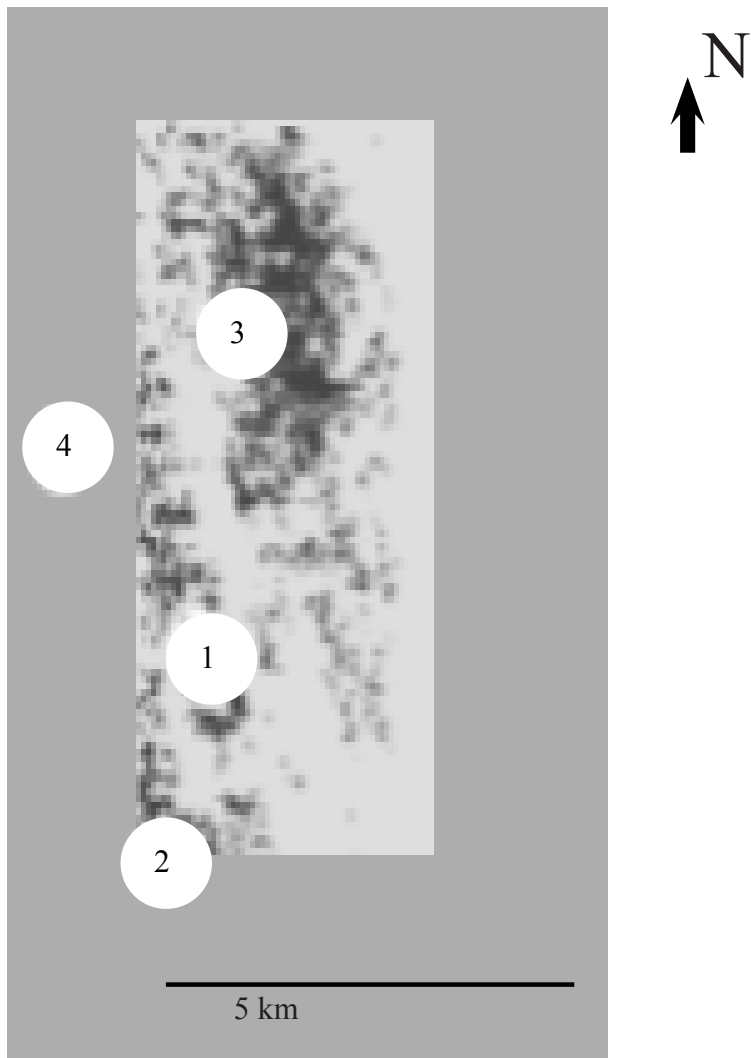
Figure 6.21: Attribute map showing the shape of the inclined internal reflectors based on the multi-scale analysis, shown together with the well locations.
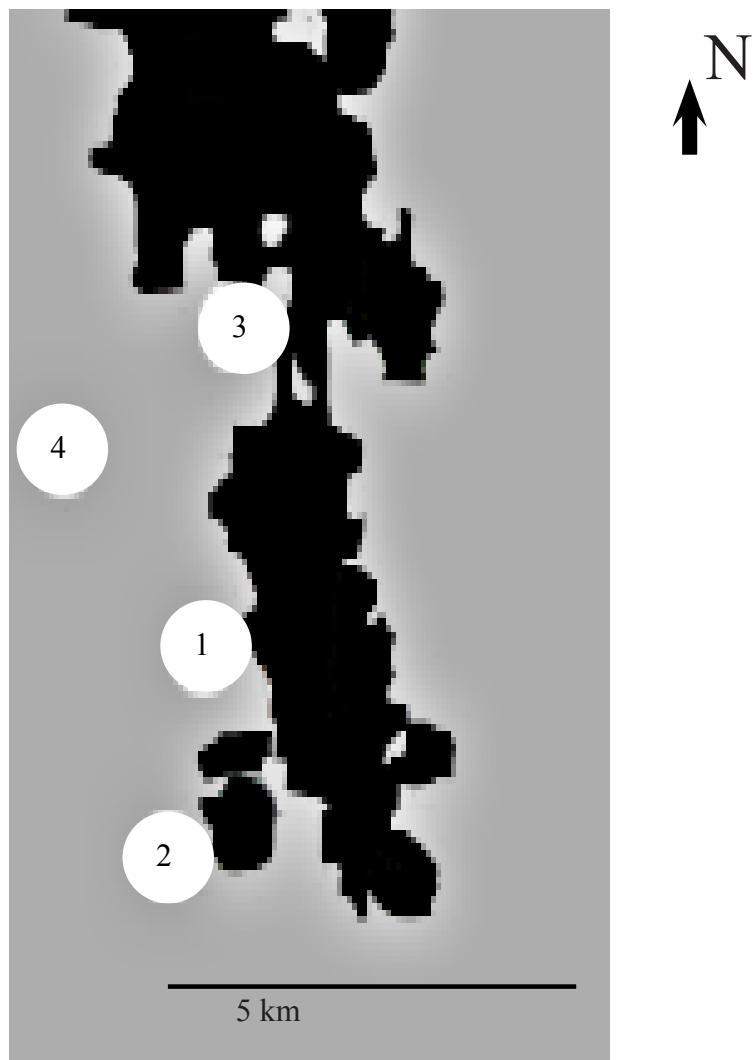
Figure 6.22: Attribute map of the inclined internal reflectors interpreted from a detailed 3D seismic study, shown together with the well locations.

7

Conclusions and recommendations

In this thesis a framework has been developed to efficiently simulate prestack depth-migrated and (constrained sparse-spike) inverted seismic data that can be directly compared with the migrated and inverted real seismic data.

This framework is used in a shared-earth modeling, were simulated migrated and (constrained sparse-spike) inverted data are used to reduce the non-uniqueness of the geological scenario construction.

The objectives of this research were: 1) to extend the combined operator concept such that there is a clear link between the simulated migrated and migrated real data on the one hand and the simulated inverted and inverted real data on the other hand, 2) to demonstrate the ability of the combined operator concept, such that geological ideas of a seismic interpreter can be tested in an iterative approach, and 3) to include seismic and geological uncertainties in the framework. In this chapter, conclusions that can be drawn from this research performed on 2D synthetic and a 2D cross-section of real 3D image are summarized, and recommendations for future research are given. This is done separately for simulated migrated and inverted data, an iterative

shared-earth modeling approach and the new seismic attribute.

7.1   Simulated migrated and inverted seismic data

A prestack depth-migrated seismic image was simulated by performing a multidimensional spatial convolution between an earth model and a spatial resolution filter. In the 1D convolution model only in the vertical direction a convolution is performed between a source wavelet and an earth model. The key element was the spatial resolution filter, which has the following characteristics:

- It was obtained from the combined operator (C) that combines the forward and the migration operator. This resembles the operators used to process the real seismic data, therefore there is a clear relation between the migrated real data and an earth model.

- All acquisition, seismic processing and model heterogeneity related effects can be properly captured in it. This also includes seismic uncertainties.

- It is a local filter.

- It can be decomposed into an angle (A) and a band-limitation filter (B). That was summarized in the double-Fourier domain as: A×B=C.

Reference data are simulated using finite-difference modeling consequently followed by a migration operator and an inversion step. The validation tests show that the simulated prestack depth-migrated data can be compared directly to the reference data. The simulated prestack depth-migrated data expressed the effects of vertical and horizontal smearing, and a different wavelet stretch for a different dip of a layer. This information was captured in the band-limitation filter. In the migrated data certain geological structures were suppressed that were present in the earth model. Which structures were suppressed was directly related to the overburden and the acquisition setup. This information was captured in the angle filter. The spatial resolution filter also expresses the effect of seismic uncertainties, e.g., a laterally varying source wavelet, errors due to a "wrong" migration velocity model (resulting in a suboptimal focused seismic image) and statics.

Seismic inversion aims to remove the band-limitation filter from migrated real data. It was shown that by constrained sparse-spike inverting the migrated real data, the band-limitation filter is only partly removed. The approximated angle filter was introduced, to simulate inverted data for this specific class of inversion algorithms. The validation tests showed that the simulated constrained sparse-spike inverted data can be compared directly to the reference data. The simulated constrained sparse-spike inverted data showed large phase and amplitude errors, especially for layers dipping more than $\sim 25°$. Additionally, the influence of adding a low-frequency model was simulated.

Finally, an important conclusion was that the spatial resolution, angle and band-limitation filters constitute a very efficient way to enhance the communication between different disciplines in geosciences. Therefore, the filters should be an integral part of a shared-earth modeling.

Recommendations

- Factors like, e.g., sampling in space play also a role in the shape of a spatial resolution filter [Schuster and Hu, 2000]. The exact influence could be tested.

- Due to the popularity of ray-based migration algorithms for migrating the real data, the computed ray-information may be stored and used to 1) guide to what degree the spatial resolution filter can be assumed laterally constant, i.e. if one or both the angles of maximum wave propagation have laterally significantly changed, a new filter is computed, 2) construct the angle filter, 3) guide the seismic interpretation process by showing the averaged horizontal resolution or maximum angles of wave propagation attribute map.

- It was shown that the band-limitation filter can be used as an accurate inversion operator. Constraining the band-limitation filter by the maximum angle of wave propagation resulted in a spatial resolution filter. That has been introduced as an inversion operator [Yu et al., 2006]. The band-limitation filter was used as an inversion filter, by realizing that ideally the migrated real data do not have any information outside the maximum angles of wave propagation. Therefore, the inversion operator did not have to be constrained by angle information. How-

ever, still the influence of noise, e.g., multiple scattering, should be tested.

Limitations

- In a comparison between simulated and real data, it was tacitly assumed that all multiple scattering has been properly removed from the real data or imaged to its correct position of origin.

- For a complex overburden, e.g., under a salt body, the local 1D assumption of the local 1D spatial resolution filter was insufficient to accurately simulate migrated and inverted data.

7.2   Iterative shared-earth modeling

A shared-earth model was used to geologically interpret inclined internal reflectors that are present in the migrated real data of the Cook Formation, Oseberg Field (offshore Norway). From an initial core, wire-line and large seismic interpretation study, two different geological scenarios both fitted the measured data. The shared-earth models describe a valley infill and east-west migrating tidal sand-bar and channel complexes in an estuarine.

The earth models describing the Cook Formation were decoupled from the velocity model that was used to compute the spatial resolution filter. Because of this, the earth model describing the reservoir can be geologically more detailed and adjusted without having to recalculate the spatial resolution and approximated angle filter. This enabled iterative testing of the two geological scenarios that consisted of the following steps:

[1] Size and shape data of modern-analogue data from the Gironde and Western-Scheldt Estuaries were used to properly constrain the geological elements in an earth model.

[2] A dip-panel was introduced to perform an enhanced well-to-seismic tie. The regional $8°$ dip of the Cook Formation is the result of a rifting phase. An inclined internal reflector dip of approximately $-4°$ dip-panel was found that fits the averaged value of the measured steepest dip of one tidal sand-bar.

[3] Simulated migrated and inverted data of the valley infill model were visually compared with the real data sets. The simulated data did not match the real data. The earth model did account for the regional $8°$ dip, but did not express the $-4°$ dip. Therefore, this earth model did not recreate the inclined internal reflectors.

[4] The same spatial resolution and approximate angle filter were used to simulate data of the east-west migrating tidal sand-bars and channel earth model. The first model used the height of the tidal sand-bar complexes that are present in the Gironde Estuary. On average the height is 15 m. The dip of the tidal sand-bar complexes is approximately -3°, which was found in the Western-Scheldt Estuary data and from the enhanced seismic-to-well tie. By comparison of the simulated migrated and inverted data and the real data, similar expressions were found.

[5] The tidal sand-bar height was increased to 30 m. This expresses the tidal sand-bars height that are present in the Western-Scheldt Estuary. The simulated data showed in the prestack depth-migrated data features that correlated with the observed inclined internal reflectors in the migrated real data. Additionally, in the simulated constrained sparse-spike inversion data, low-impedance zones are observed that were also present in the constrained sparse-spike inverted real data. The observations in the simulated migrated and impedance data led to the conclusion that east-west migrating channels and tidal sand-bars in an estuarine environment produce the best fitting geological model.

Recommendations

- The spatial resolution filter were computed from a synthetic overburden under a zero-offset condition. Ideally, the macro velocity that is used to migration to migrate the real data should be used to compute the spatial resolution filter.

- Numerical experiments, analogue modeling and production data (history matching Gosselin et al. [2004]), etc, can also be use to improve the non-uniqueness of the geological scenario construction, as well as, etc.

- A shared-earth model is also very suitable as managing, prediction and planning tool. It will therefore fit in a closed-loop reservoir system that has been proposed to optimize hydrocarbon production [Jansen et al., 2005].

- As the cosine of the phase attribute map of the base of the Cook Formation showed, the interpreted estuarine shape did not honor all well positions. Therefore, geologically interpreting seismic attribute data should also be supported by making use of simulated migrated data.

- Iterative shared-earth modeling can further be enhanced with a solid way of comparing the simulated migrated and inverted seismic data with the migrated and inverted real data and consequently automatically update the earth model in order to obtain the best fitting model.

7.3   Multi-scale seismic attribute

Matching inclined internal reflectors for example of the Cook Formation and changes in an earth model, is a nontrivial task. The multi-scale analysis was used to facilitate this.

- The spatial resolution filter was used as the proper link between an earth model and the migrated real data to derive the proper input parameters of the wavelet transform such that sequence boundaries found in wire-line and inverted data can be correlated using a unique α characterization value.

- Analyzing and geologically interpreting the wire-line data using the α characterization showed that each sequence boundary had a unique value that was used to enhance the correlation process in order to understand the lateral distribution of the geological facies of the Cook Formation.

- The approximated angle filter was used to simulate constrained sparse-spike inverted data in a sensitivity analysis. In this way, the influences of inversion errors on the multi-scale analysis were investigated. It turns out that for geological dips up to a maximum of $\sim 15°$, and for

small errors in the estimated inversion wavelet such that they do not significantly change the α characterization value.

- The core data was used to find the position of the tidal-sand bar in the wire-line data of the Cook Formation. At this position a α characterization value was calculated. This value was track in the inverted real data. The shape of the resulting attribute map strengthened the conclusion that the inclined internal reflectors are produced by tidal sand-bar complexes that are present in an estuarine environment.

Recommendations

- In this study only changes in sedimentation processes were used to geologically interpret the multi-scale results. Fluids and compaction processes also strongly influence the elastic properties, therefore these need to be incorporated as well [Goudswaard, 2001].

- The sensitivity analysis can be part of an application to guide the seismic inversion process itself. The wire-line information provides valuable a-priori knowledge on the value of α. If this information is not coherent in the inverted data, the inversion parameters should be adapted with a sensitivity analysis guiding the process.

- The multi-scale analysis can be used as an application to compare the inverted real seismic data with an earth model.

A

Zero-offset spatial resolution filter

A spatial resolution filter is computed in two different ways, on the one hand by constructing an angle and band-limitation filter in the double-Fourier domain and on the other hand by forward modeling and subsequently a migration step. This latter option is briefly discussed for a 2D horizontally layered earth model.

A.1 Zero-offset forward modeling and migration using the phase-shift operator

A velocity trace is obtained from a borehole or from the migration velocity model that was used to prestack-depth migrate the real seismic data. This velocity trace is then used to build a horizontally layered earth model. In each layer, the velocity is constant and a wave field can be propagated in this layer by making use of the Gazdag phase-shift operator [Gazdag, 1978]. Applying this operator recursively, the wave field is then propagated through

all layers of the earth model. We will briefly discuss how the phase-shift operator is derived and how it is numerically evaluated in the double-Fourier domain.

Consider the 2D source-free acoustic wave equation for a homogeneous medium,

$$\nabla^2 p - \frac{1}{c^2}\frac{\partial^2 p}{\partial t^2} = 0, \tag{A.1}$$

where $p = p(x, z, t)$ is the acoustic pressure, c is the P-wave velocity and ∇^2 is the Laplace operator. The forward Fourier transform from the space-time domain to the wavenumber-frequency domain is defined as

$$\tilde{P}(k_x, z, \omega) = \int_\infty^\infty \int_\infty^\infty p(x, z, t)e^{-j(\omega t - k_x x)}dtdx, \tag{A.2}$$

and the inverse Fourier transform as,

$$p(x, z, t) = \frac{1}{\pi}\Re \int_0^\infty d\omega \int_\infty^\infty \tilde{P}(k_x, z, \omega)e^{j(\omega t - k_x x)}dk_x. \tag{A.3}$$

Forward Fourier transformation of equation (A.1) with respect to the horizontal spatial coordinate (x) and time (t) yields,

$$\partial_z^2\tilde{P} + (k^2 - k_x^2)\tilde{P} = 0, \tag{A.4}$$

where $\tilde{P} = \tilde{P}(k_x, z, \omega)$ and $k = \frac{\omega}{c}$. The solution of equation (A.4) is well known,

$$\tilde{P}(k_x, z, \omega) = \tilde{P}(k_x, z_m, \omega)e^{\pm jk_z|z_m - z|}, \tag{A.5}$$

with

$$k_z = \begin{cases} \sqrt{k^2 - k_x^2} & k_x^2 \leqslant k^2 \\ -j\sqrt{k_x^2 - k^2} & k_x^2 > k^2 \end{cases} \tag{A.6}$$

and $j = \sqrt{(-1)}$. The current depth is denoted by z and z_m denotes the mth sample of the gridded input velocity trace. On physical grounds in equation (A.5), the minus sign is chosen for forward wave propagation. The plus

sign is for inverse propagation. The forward operator shows that wave field propagation in a homogeneous layer of the velocity trace is described by a phase-shift operator in the double-Fourier domain, or k_x, ω domain [Gazdag, 1978],
For upward propagation waves this comes to,

$$\tilde{P}^-(z_{m-1}) = \tilde{W}^-(z_{m-1}, z_m)\tilde{P}^-(z_m), \qquad (A.7)$$

where $\quad \tilde{W}^-(z_{m-1}, z_m) = e^{-jk_z|z_{m-1}-z_m|}$.
To resemble the zero-offset experiment, the exploding reflector model is used (Figure 2.4 (b)). Hence, half the P-wave velocity is taken, so we replace $k = \frac{\omega}{c}$ by $k = \frac{\omega}{c/2}$.
The recursion starts at the depth level for which one wants to derive the spatial resolution or angle filter, with $\tilde{P}(k_x, z, \omega) = S(\omega)$, where $S(\omega)$ is the spectrum of the source wavelet, and ends at the acquisition depth level z_0. The inverse wave field extrapolator ($\tilde{F}^- = 1/\tilde{W}^-$) forms the basis for zero-offset depth migration. To obtain a stable inverse wave field extrapolator, the complex conjugate of the forward operator is taken according to $\langle \tilde{F}^- \rangle = (\tilde{W}^-)^*$. Physically, this means that only the propagating wave region is used (Figure A.1). Hence,

$$\tilde{P}^-(z_m) = \langle \tilde{F}^-(z_m, z_{m-1}) \rangle \tilde{P}^-(z_{m-1}), \qquad (A.8)$$

where $\langle \tilde{F}^-(z_m, z_{m-1}) \rangle = e^{+jk_z^*|z_m-z_{m-1}|}$.
The final depth-migrated image is obtained when the wave field is evaluated at $t = 0$ for all depth levels. In the double-Fourier domain this is done by a summation over all frequency components for each k_x. Finally, the zero-offset depth-migrated image is obtained by an inverse Fourier transform from the wave-number to the space domain,

$$\text{Depth-migrated image}(x, z) = (\text{FFT})^{-1}\left[\sum_{\omega_i} \tilde{P}(k_x, z, \omega_i)\right], \qquad (A.9)$$

where x, z denotes the spatial coordinates of a point in the earth model.
For more extensive details we refer to Berkhout [1987] and Wapenaar and Berkhout [1989]. The depth-migrated image shows a spatial resolution filter if the double-Fourier transformed result of a unit strength point scatterer multiplied with the source spectrum is used as input to equation (A.7).
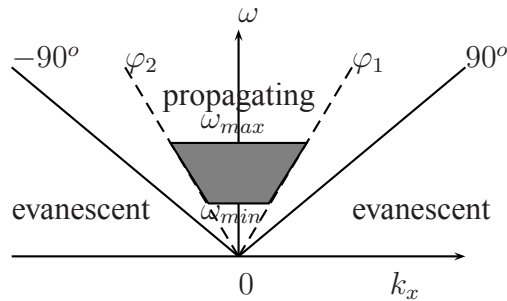
Figure A.1: Overview of the double-Fourier domain. The solid lines (denoted by -90° and 90°) mark the boundary between the propagating and evanescent part of a wave field. The dashed lines indicate the maximum angles of wave propagation (φ_1 and φ_2). These angles are less than 90° due to a limited recording aperture and effect of the overburden (Chapters 4 and 3). The signal of the artificial source has a frequency content that is marked by ω_{min} to ω_{max}. To reduce computational costs only the gray filled region need to be computed.

The depth-migrated image shows a angle filter if the double-Fourier transformed result of a unit strength point scatterer is used as input to equation (A.7).

■ A.1.1 Numerical implementation

In the double-Fourier or (k_x, ω) domain equations (A.5) and (A.8) are numerically evaluated (Figure A.1). The horizontal axis displays the wavenumber (k_x) and the vertical axis the angular frequency ($\omega = 2\pi f$). For a computationally efficient implementation of these equations, consider the following fifth features.

Firstly, recognize that the Fourier transform is computed from a real and causal signal. This means that only the positive frequencies have to be calculated; the complex-to-real inverse Fourier transform obviates the need for negative frequency values (equation (A.3)).

Secondly, if the square root of the phase-shift operator becomes imaginary the wave field is evanescent (exponentially decaying) (equations (A.5) and (A.6)). Therefore, the phase-shift operator is only applied if the wave field

is propagating. The maximum angles of wave propagation (φ_1 and φ_2) mark these boundaries. These are less than $\pm 90^o$ due to a limited recording aperture and effect of the overburden (see for an extensive discussion Chapters 3 and 4).

Thirdly, the signal of the artificial source has a particular frequency content from ω_{min} to ω_{max}. This means that in the frequency range up to the Nyquist frequency, not all frequencies need to be calculated. Thus, to reduce computational costs only the gray filled region in Figure A.1 need to be evaluated.

Fourthly, recognize that applying the phase-shift operator is a linear process. Thus, the same phase-shift operator is used when the next layer of the layered earth model has the same velocity as the previous layer.

Finally, computing different spatial resolution filters is an embarrassingly parallel problem.

Pseudo codes

Input to the forward algorithm is a gridded velocity trace, the depth of the unit strength point scatter, information on the acquisition and processing parameters and a source wavelet. The signal of the source wavelet has a particular frequency content. Additionally, information on the maximum angles of wave propagation (φ_1 and φ_2) is used to compute a so-called local 1D spatial resolution filter (Chapter 3). Below is the pseudo code of the forward part.

```
function gazdag_modeling(velocity trace,
    acquisition and processing parameters,
    source wavelet,
    maximum angles of wave propagation)

velocity trace = c/2

for z =  z_{m} to z_{1}
  for w = w_{min} to w_{max}
    for k_{x} = k_{1} to k_{max}
        check depth unit strength point scatterer
        if c(z) ˜= c(z-1)
            calculate new forward operator up to
```

```
           the maximum angles of wave propagation
        endif
        apply forward operator

    end
  end
end

add source wavelet
```

The pseudo-code of the migration part is

```
function gazdag_migration(forward modeled data,
velocity trace, acquisition and
processing parameters)

velocity trace = c/2

for z = z_{1} to z_{m}
  for w = w_{min} to w_{max}
    for k_{x} = k_{1} to k_{max}
        if c(z) != c(z-1)
           calculate new inverse operator
        endif
        apply inverse operator

  image condition: sum over all frequencies
  end
  FFT^{-1} k_{x}
end
```

Bibliography

Aki, K. and Richards, P. G. (2002). *Quantitative Seismology*. University Science Books.

Avseth, P., Flesche, H. and Van Wijngaarden, A. (2003). AVO classification of lithology and pore fluids constrained by rock physics depth trends. *The Leading Edge*, 22 (10), pp. 1004–1011.

Badescu, O. M. (2002). *Thick-bedded deep marine sandstones, the use of analogs for reservoir appraisal*. Ph.D. thesis, TUD.

Berkhout, A. J. (1987). *Applied Seismic Wave Theory*. Elsevier Science, Amsterdam.

Berkhout, A. J., Ongkiehong, O., Volker, A. W. F. and Blacquiere, G. (2001). Comprehensive assessment of seismic acquisition geometries by focal beams Part I: Theoretical considerations. *Geophysics*, 66 (3), pp. 911–917.

Beylkin, G. and Burridge, R. (1984). Linearized inverse scattering problems in acoustics and elasticity. *Wave Motion*, 12 (1), pp. 15–52.

Blauw, B. and Toxopeus, P. H. (2001). *HET GESLACHT TOXOPAEUS 1576-2000*. Stedum : Stichting Gerrit Alje Toxopeus 1852.

Bleistein, N., Cohen, J. K. and Stockwell (Jr.), J. W. (2000). *Mathematics of Multimensional Seismic Imaging, Migration, and Inversion*. Springer-Verlag.

Bos, C. and Van Kruijsdijk, C. P. J. W. (1997). Reservoir Engineering and Geosciences. *Final resport, EC Joule II, Reservoir Engineering Project, JOU2-0182*, Kruijsdijk, C. P. J. W. v. and Elewout, E. F. M., eds., pp. 1–6. NITG-TNO report, Delft, The Netherlands.

Chen, J. and Schuster, G. T. (1999). Resolution limits of migrated images. *Geophysics*, 64 (4), pp. 1046–1053.

Claerbout, J. F. (1976). *Fundamentals of Geophysical Data Processing*. McGraw-Hill Book Co. Inc.

Dalman, R., Donselaar, M. E. and Toxopeus, G. (2003). The Reservoir Geology of the Cook Formation, Oseberg Field, Offshore Norway. Yearly progress report Norsk Hydro, Delft University of Technology.

Deregowski, S. M. and Rocca, F. (1981). Geometrical optics and wave theory of constant offset sections in layered media. *Geophysical Prospecting*, 29 (03), pp. 374–406.

Devaney, A. J. (1984). Geophysical diffraction tomography. *Trans. Geosci. Remote Sensing*, 22 (1), pp. 3–13.

Færseth, R. B. and Ravnås, R. (1998). Evolution of the Oseberg Fault-Block in context of the northern North Sea structural framework. *Marine and Petroleum Geology*, 15, pp. 467–490.

Fenies, H. and Tastet, J. P. (1998). Facies and architecture of an estuarine tidal bar (the Trompeloup bar, Gironde Estuary, SW France). *Marine Geology*, 150, pp. 149–169.

Ferguson, R. J. and Margrave, G. F. (1996). A simple algorithm for band-limited impedance inversion. *CREWES Research Report*, V8 (21), pp. 1–10.

Gazdag, J. (1978). Wave equation migration with the phase-shift method. *Geophysics*, 43, pp. 1342–1351.

Gelius, L. J., Lecomte, I. and Tabti, H. (2002). Analysis of the resolution function in seismic prestack depth imaging. *Geophysical Prospecting*, 50, pp. 505–515.

Ghose, R. and Goudswaard, J. (2004). Integrating S-wave seismic-reflection data and cone-penetration-test data using a multiangle multiscale approach. *Geophysics*, 69 (2), pp. 440–459.

Gjøystdal, H., Iversen, E., Laurain, R., Lecomte, I., Vinje, V. and Astebol, K. (2002). Review of Ray Theory Applications in Modelling and Imaging of Seismic Data. *Studia Geophysica et Geodaetica*, 46 (2), pp. 113–164.

Gosselin, O., Aanonsen, S. I., Cominelli, A., Gonard, R., Kolasinski, M., Kovacic, L. and Neylon, K. (2004). History matching using time-lapse seismic (HUTS). *Journal of Petroleum Technology*, 04, pp. 66–67.

Goudswaard, J. (2001). *Multiangle Multiscale Characterization of Seismic Reflection Data*. Ph.D. thesis, TUD.

Gratwick, D. and Finn, C. (2005). What's important in making far-stack well-to-seismic ties in West Africa? *The Leading Edge*, 24 (7), pp. 739–745.

Hagedoorn, J. (1954). A process of seismic reflection interpretation. *Geophysical Prospecting*, 2, pp. 85–127.

Hart, B. and Chen, M. A. (2004). Interpreter's corner - Understanding seismic attributes through forward modeling. *The Leading Edge*, 23 (09), pp. 834–841.

Herrmann, F. J. (1997). *A scaling medium representation*. Ph.D. thesis, TUD.

Hill, S., Dragoset, B. and Weglein, A. (1999). An introduction to this special section: The new world of multiple attenuation. *The Leading Edge*, 18 (1), pp. 38–38.

Hydrografie (2003). Westerschelde 2003. Uitgeven door het Ministerie van de Vlaamse Gemeenschap - Departement Leefmilieu en Infrastructuur.

Jansen, J. D., Brouwer, D. R., Naevdal, G. and Van Kruijsdijk, C. P. J. W.
(2005). Closed-loop reservoir management. *First Break*, 23 (1), pp. 43–
48.

Kallweit, R. S. and Wood, L. C. (1982). The limits of resolution of zero-
phase wavelets. *Geophysics*, 47 (07), pp. 1035–1046.

Kapsimalis, V., Massé, L. and Tastet, J. P. (2004). Tidal impact on modern
sedimentary facies in the Gironde Estuary, southwestern France. *Journal
of Coastal Research*, 41, pp. 1–11.

Lancaster, S. and Whitcombe, D. (2000). *Fast-track 'coloured' inversion*,
pp. 1572–1575. Soc. of Expl. Geophys.

Laurain, R., Vinje, V. and Strand, C. (2004). Simulated migration amplitude
for improving amplitude estimates in seismic illumination studies. *The
Leading Edge*, 23 (3), pp. 240–245.

Lecomte, D. I. and Pochon Guerin, M. L. (2005). *Simulated 2D/3D PSDM
images with a fast, robust, and flexible FFT-based filtering approach*, pp.
1810–1813. Soc. of Expl. Geophys.

Lecomte, I., Gjøystdal, H. and Drottning, A. (2003). *Simulated prestack lo-
cal imaging: A robust and efficient interpretation tool to control illumina-
tion, resolution, and time-lapse properties of reservoirs*, pp. 1525–1528.
Soc. of Expl. Geophys.

Lee, S. Y., Hwang, J. W., Seo, M. G. and Myung, Y. S. (2002). Recent
Fingerprint Image Enhancement Using Wavelet Transforms. *The 8th con-
ference on Applications of Computer Algebra*.

Lindanger, R., Øygaren, M., Gabrielsen, R. H., Mjelde, R., Randen, T. and
Tjøstheim, B. A. (2004). Analogue (plaster) modeling and synthetic seis-
mic representation of haningwall fault blocks above ramp-flat ramp exten-
sional faults. *First Break*, 22 (1), pp. 33–41.

Loewenthal, D., Roberson, L. R. and Sherwood, J. W. (1985). The wave
equation applied to migration. *Geophysical Prospecting*, 24, pp. 380–399.

Luthi, S. M. (2001). *Geological Well Logs, their use in reservoir modelling*. Springer-Verlag, Berlin-Heidelberg, Germany.

Mallat, S. G. and Hwang, W. L. (1992). Singularity detection and processing with wavelets. *IEEE Transactions on Information Theory*, 38 (2), pp. 617–643.

Marjanac, T. (1995). Architecture and sequence stratigraphy of the Dunlin Group formations and proposal for new type and reference-wells: Sequence stratigraphy on the north-west European margin. *NPF special publication*, 5, pp. 143–165.

Matson, K. and Dragoset, B. (2005). An introduction to this special section—multiple attenuation. *The Leading Edge*, 24 (3), pp. 252–252.

Mittet, R., Sollie, R. and Hokstad, K. (1995). Prestack depth migration with compensation for absorption and dispersion. *Geophysics*, 60 (05), pp. 1485–1494.

Mulder, W. A. and Plessix, R. E. (2004). A comparison between one-way and two-way wave-equation migration. *Geophysics*, 69 (6), pp. 1491–1504.

Nemeth, T., Wu, C. and Schuster, G. T. (1999). Least-squares migration of incomplete reflection data. *Geophysics*, 64 (1), pp. 208–221.

Nio and Yang (1989). Recognition of tidally-influenced facies and environments. Short course note series 1, InterGeos B. V., Leiderdorp, The Netherlands.

Oldenburg, D. W., Scheuer, T. and Levy, S. (1983). Recovery of the acoustic impedance from reflection seismograms. *Geophysics*, 48 (10), pp. 1318–1337.

Paffenholz, J., Stefani, J., McLain, B. and Bishop, K. (2002). *SIGSBEE 2A Synthetic Subsalt Dataset - Image Quality as Function of Migration Algorithm and Velocity Model Error*, p. B019. Eur. Assn. Geosci. Eng.

Petersen, S. A. (1992). *A description of the geophysical technology and its impact on the construction of ideal information bases*, pp. 74–75. EAGE.

Popovici, A. M. (1994). *Reducing artifacts in prestack phase-shift migration of common-offset gathers*, pp. 684–687. Soc. of Expl. Geophys.

Pratson, L. and Gouveia, W. (2002). Seismic simulations of experimental strata. *Bulletin of the American Association of Petroleum Geologists*, 86 (1), pp. 129–144.

van Riel, P. and Berkhout, A. J. (1985). Resolution in seismic trace inversion by parameter estimation. *Geophysics*, 50 (09), pp. 1440–1455.

Schuster, G. T. and Hu, J. (2000). Green's function for migration: Continuous recording geometry. *Geophysics*, 65 (01), pp. 167–175.

Sheriff, R. E. (2001). *Encyclopedic Dictionary of Exploration Geophysics*. Soc. of Expl. Geophys.

SMAART (2002). Publicly released smaart data sets, available to the geophysical industry. `http://www.delphi.tudelft.nl/SMAART/`.

Smythe, J., Gersztenkorn, A., Radovich, B., Li, C. and Liner, C. (2004). Gulf of mexico shelf framework interpretation using a bed-form attribute from spectral imaging. *The Leading Edge*, 23 (9), pp. 921–926.

Stolt, R. H. (1978). Migration by Fourier transform. *Geophysics*, 43 (1), pp. 23–48.

Thomassen, R. A. J., Dalman, R. A. F., Donselaar, M. E., Dreijer, T., Luthi, S. M. and Toxopeus, G. (2006). The use of modern analogues in shared earth model-ling (Case study of the Cook Formation, Oseberg Field, offshore Norway). *Expanded Abstracts of the 68th EAGE Conference & Exhibition*, p. B006.

Thorbecke, J., Wapenaar, K. and Swinnen, G. (2004). Design of one way wavefield extrapolation operators, using smooth functions in WLSQ optimization. *Geophysics*, 69 (4), pp. 1037–1045.

Veeken, P. C. H. and Da Silva, M. (2004). Seismic inversion methods and some of their constraints. *First Break*, 22 (06), pp. 47–70.

Vermeer, G. J. O. (2001). *3-D Seismic Survey Design*. Soc. of Expl. Geophys.

Verschuur, D. J., Berkhout, A. J. and Wapenaar, C. P. A. (1992). Adaptive surface-related multiple elimination. *Geophysics*, 57 (09), pp. 1166–1177.

Volker, A. W. F., Blacquiere, G., Berkhout, A. J. and Ongkiehong, O. (2001). Comprehensive assessment of seismic acquisition geometries by focal beams – Part II: Practical aspects and examples. *Geophysics*, 66 (3), pp. 918–931.

Vollset, J. and Doré, A. G. (1984). A revised Triassic and Jurassic lithostratigraphic nomenclature for the Norwegian North Sea. *NPD Bulletin*, p. 53.

Wapenaar, C. P. A. and Berkhout, A. J. (1989). *Elastic wave field extrapolation: redatuming of single-and multi-component seismic data*. Elsevier Science Publishing Co., Amsterdam.

Wapenaar, C. P. A. and Grimbergen, J. L. T. (1996). Reciprocity theorems for one-way wave fields. *Geoph. J. Int.*, 127, pp. 169–177.

Wapenaar, K., Ghose, R., Toxopeus, G. and Fokkema, J. (2005). The wavelet transform as a tool for geophysical data integration. *Integrated Computer-Aided Engineering*, 12 (1), pp. 20.

Wapenaar, K., Van Wijngaarden, A. J., Van Geloven, W. and Van der Leij, T. (1999). Apparent AVA effects of fine layering. *Geophysics*, 64 (6), pp. 1939–1948.

Wever, A. and Spetzler, J. (2004). *Criteria for source and receiver positioning in time-lapse seismic acquisition*, pp. 2319–2322. Soc. of Expl. Geophys.

White, R. and Simm, R. (2003). Tutorial: Good practice in well tie. *First Break*, 21 (10), pp. 75–83.

Yilmaz, O. (2001). *Seismic Data Analysis*, volume 02, pp. 1001–2027. Soc. of Expl. Geophys.

Yu, J., Hu, J., Schuster, G. T. and Estill, R. (2006). Prestack migration deconvolution. *Geophysics*, 71 (2), pp. S53–S62.

Zhu, J., Lines, L. and Gray, S. (1998). Smiles and frowns in migration/velocity analysis. *Geophysics*, 63 (04), pp. 1200–1209.

Abstract

Simulating migrated and inverted seismic data for enhanced reservoir characterization

Gerrit Toxopeus

Natural resources, in particular hydrocarbon reservoirs are commonly located by a shared-earth modeling concept. The construction of the shared-earth model is hampered by the fact that measurements have a difference in spatial coverage and resolution. Consequently, different earth models all fit the measured data. Migrated seismic data can help to reduce the non-uniqueness of a geological scenario. However, the resolution of migrated seismic data is insufficient to directly support this approach. This discrepancy is reduced using the framework of simulated migrated and inverted seismic data.

The industry practice is to simulate seismic data by filtering an earth model with a wavelet, which is known as the 1D convolution model. Unfortunately, this model only expresses the vertical resolution of migrated data but does not account for the lateral resolution aspects of the migration process. Therefore, the simulated migrated seismic data cannot directly be compared to the migrated real data.

The research presented in this thesis concerns a new and computationally efficient method for simulating prestack depth-migrated and (constrained sparse-spike) inverted seismic data that can be compared directly to the migrated and inverted real data. This is essential for an optimal use of shared-earth modeling.

This objective is achieved by introducing the spatial resolution filter and simulating prestack depth-migrated data by filtering an earth model with this filter. The spatial resolution filter is obtained from the combined operator (C) that combines the forward and migration operator.

The spatial resolution filter is decomposed into an angle (A) and band-limitation (B) filter, summarized in the double-Fourier domain as: A×B=C. This result, is used to show that by the current industry practice of constrained sparse-spike inverting the migrated real data the band-limitation filter is only partly removed. The approximated angle filter is introduced, to simulate inverted data for this specific class of inversion algorithms. Three synthetic examples demonstrate the ability to accurately simulate prestack depth-migrated and inverted data that can be compared directly to the reference data.

An enhanced shared-earth modeling approach is used to geologically interpret inclined internal reflectors that are present in the migrated real data of the Cook Formation, Oseberg Field (offshore Norway).

From initial core and wire-line data and a large seismic interpretation study, two different geological scenarios both fit the measured data. The earth-models describe a valley infill and east-west migrating channels and tidal sand-bars, respectively.

The earth models describing the Cook Formation is decoupled from the velocity model that is used to compute the spatial resolution and approximate angle filter. Because of this, the earth model describing the reservoir can be geologically more detailed and adjusted without having to recalculate the filters. This enables iterative testing of the two geological scenarios. By a visual comparison of the simulated migrated and inverted data with the real data sets, it appears that tidal sand-bar complexes that are present in an estuarine environment produce the best fitting geological model. The size and shape data of tidal sand-bars in two modern-analogues is used to increase the fit in the iterative approach.

Matching the inclined internal reflectors of the Cook Formation with changes in an earth model, is a nontrivial task. The multi-scale analysis is used to facilitate this.

The spatial resolution filter is used to derive the proper input parameters of the wavelet transform such that one sequence boundary found in the impedance log is correlated to one reflector in the inverted seismic data us-

ing a unique α characterization value. The approximated angle filter is used to simulate constrained sparse-spike inverted data that is used in a sensitivity analysis. In this way, the influences of inversion errors on the multi-scale analysis are investigated. It turns out that geological dips up to a maximum of $15°$, and for small errors in the estimated inversion wavelet such that they do not significantly change the α characterization value.

The wire-line data of the Cook Formation is used to calculate one α characterization value of a tidal-sand bar. This value is tracked in the wavelet transformed constrained sparse-spike inverted real data. The shape of the resulting attribute map strengthens the conclusion that the inclined internal reflectors are produced by tidal sand-bar complexes that are present in an estuarine environment.

Samenvatting

Simuleren van gemigreerde en geïnverteerde seismische data voor verbeterde reservoir karakterisatie

Gerrit Toxopeus

Om natuurlijke hulpbronnen, in het bijzonder olie- en gasvoorkomens te vinden wordt gewoonlijk gebruikt gemaakt van een geïntegreerde aanpak. Een optimaal gebruik van deze aanpak wordt helaas belemmerd doordat de meetgegevens een verschillend meetgebied beslaan en de resolutie verschillend is. Dientengevolge voldoen meerdere geologische modellen aan de gemeten data. Gemigreerde seismische data worden gebruikt om één geologisch model te selecteren. Echter, de verticale resolutie van gemigreerde data is te laag en daarom wordt er gebruik gemaakt van gesimuleerde gemigreerde data om het best passende geologische model te vinden.

Seismische data wordt meestal gesimuleerd door een geologisch model met een bronsignaal te filteren, dit model staat bekend onder de naam "1D convolution model". Helaas wordt zo alleen de verticale resolutie van de gemigreerde seismische data gesimuleerd en de laterale resolutie aspecten van het migratie proces verwaarloosd. Daardoor kunnen de gesimuleerde data niet direct worden vergeleken met de echte data, wat een essentiële stap vormt in een geïntegreerde aanpak.

Het gepresenteerde onderzoek heeft betrekking op het efficiënt simuleren van gemigreerde en geïnverteerde seismische data die direct vergeleken kunnen worden met de echte gemigreerde en geïnverteerde seismische. Om dit

doel te bereiken wordt een spatiële resolutiefilter gebruikt en gemigreerde seismische data worden gesimuleerd door het filteren van een geologisch model met dit spatiële resolutiefilter. Het spatiële resolutiefilter representeert de gecombineerde operator (C) welke de voorwaartse- en migratieoperator combineert.

Het spatiële resolutiefilter valt uiteen in een hoek- (A) en een frequentiefilter (B), in het dubbele-Fourier domein wordt dit weergegeven als: A×B=C.

Dit resultaat wordt gebruikt om aan te tonen dat met de huidige inversie proces dat wordt toegepast op de gemigreerde seismische data, het frequentiefilter maar ten dele wordt verwijderd. Om deze zogenaamde sparse-spike geinverteerde seismische data te simuleren wordt een benaderd hoekfilter geïntroduceerd. Drie synthetische voorbeelden illustreren dat de gesimuleerde gemigreerde en geïnverteerde seismische data direct te vergelijken zijn met referentie data.

In de gemigreerde seismische data van de Cook Formatie worden hellende reflectoren geïnterpreteerd. Uit een eerdere studie werd geconcludeerd dat twee geologische modellen beide voldoen aan de gemeten kern- en boorgegevens. Het eerste geologische model beschrijft het opvullen van een vallei en het tweede geologische model beschrijft zandbanken die gevormd zijn in een estuarium. De geologische modellen die Cook Formatie beschrijven zijn los gekoppeld van het geologische model om het spatiële resolutie- en benaderd hoekfilter te berekenen. Daarom kan het reservoir model van de Cook Formatie worden veranderd, zonder dat de filters opnieuw uitgerekend hoeven te worden. Dit maakt een iteratieve geïntegreerde aanpak mogelijk. Door een visuele vergelijking van de gesimuleerde gemigreerde en geïnverteerde seismische data met de echte data sets, wordt geconcludeerd dat zandbanken in een estuarium het best passende geologische model is. Door het bestuderen van deze zandbanken in enkele bestaande estuaria wordt realistische informatie over groottes en hoogtes van deze zandbanken verkregen. Deze informatie wordt gebruikt om een beter passend model te vinden.

Het is niet triviaal om de scheve reflectoren in de Cook Formatie te correleren met één overgangen in boorputgegevens. Een schaalafhankelijke karakterisering methode is gebruikt om dit te mogelijk te maken. Het spatiële resolutiefilter wordt gebruikt om de juiste parameters af te leiden voor de schaalafhankelijke karakterisering methode, zodat met één unieke waarde (α) één overgang uit de boorputgegevens te correleren is met één reflector

in de geïnverteerd seismische data. Het benaderd hoekfilter wordt gebruikt om geïnverteerd seismische data te simuleren. Op deze data wordt een sensitiviteitstest uitgevoerd. Dit laat zien dat inversie fouten een invloed hebben op de schaalafhankelijke karakterisering methode. Echter, voor hellende geologische lagen van minder dan 15° en kleine fouten in het inversie operator zijn deze fouten verwaarloosbaar.

Uit de boorputgegevens van de Cook Formatie wordt één α waarde bepaald die behoort bij de zandbanken in de Cook Formatie. Volgens, wordt de schaalafhankelijke karakterisering toegepast op de geïnverteerde seismische data. De vorm van de posities van de resulterende α kaart, versterkt de conclusie dat de hellende reflectoren in de Cook Formatie kunnen worden geïnterpreteerd als zandbanken in een estuarium.

Curriculum vitae

Gerrit Toxopeus was born in Assen, The Netherlands, on November 16, 1976
[Blauw and Toxopeus, 2001]. From 1989 to 1996 he attended secondary
school (VWO) at the "Doctor Nassau College" in Assen. In September of
the year 1996, he started his university studies in Applied Geophysics at the
Delft University of Technology, Faculty of Applied Earth Sciences. For his
M.Sc. thesis, he carried out research in the field of elastic wave propagation
on common-of-the-shelf built parallel computers (Beowulf). On 14 December 2001 he received his M.Sc. degree cum laude.

On December 1, 2001 Gerrit started his Ph.D. research on developing a novel
and compute efficient method to simulate prestack depth-migrated and inverted data. The research was supervised by Professor Dr. ir. C.P.A. Wapenaar, Professor Dr. S.M. Luthi and Professor Dr.ir. J.T. Fokkema and project
leader Dr. M.E. Donselaar of the Delft University of Technology. It is part
of Norsk Hydro's project "GeoLogical Elements for Seismic (GLEFS)". A
travel grant of The Netherlands Organization for Scientific Research (NWO)
made a three months research visit to the University of Utah in Salt Lake
City (United States of America) possible. In addition, Gerrit presented his
research at several international conferences and Hydro's research center in
Bergen (Norway). This research led to the present Ph.D. thesis.

Dankwoord

If I have seen further it is by standing on ye shoulders of Giants
(*Isaac Newton*)

Veel mensen hebben bijgedragen aan het tot stand komen van dit werk. Ik wil deze mensen dan ook graag bedanken.

Als eerste mijn promotoren Kees Wapenaar, Stefan Luthi en Jacob Fokkema, door mij te ondersteunen op zowel het onderzoeks- als het persoonlijke vlak. In dit rijtje horen ook mijn dagelijkse begeleiders Rick Donselaar en Jan Thorbecke thuis. Jullie hebben mij uit vele valkuilen geholpen en het vertrouwen gegeven dat wat als een tweejarig project begon zou kunnen uitgroeien tot dit werk. Ook reizen naar congressen en veldwerken met elk van jullie zal ik niet snel vergeten.

Takk til Steen Petersen og Tom Dreyer for godt samarbeid og for mange hyggelige besøk til Norsk Hydros forskningssenter.

Next, I would like to thank Jerry Schuster for a very pleasant stay at the University of Utah, including all the fruitful (non-)scientific discussions. I will never forget the leaf party you have organized for me! Jianhua Yu for teaching the aspects of the migration-deconvolution program and all the students of Jerry, especially Travis Crosby for showing me around in town.

Omdat mijn onderzoek op het grensvlak van de geologie en geofysica heeft plaatsgevonden ben ik mijn dank verschuldigd aan veel meer mensen, ik noem kort Clemens Visser en Rory Dalman voor hulp met de geologische